Many-Body Physics with Atomically Thin Semiconductors and Ultracold Atoms

Dissertation

Marcel Wagner

2024

Dissertation

submitted to the
Combined Faculty of Mathematics, Engineering and Natural Sciences
of Heidelberg University, Germany
for the degree of
Doctor of Natural Sciences

Put forward by
Marcel André Wagner,
born in Stuttgart

Oral examination: July 23, 2024

Many-Body Physics with Atomically Thin Semiconductors and Ultracold Atoms

---

Referees: Prof. Dr. Richard Schmidt
Prof. Dr. Hans Peter Büchler

– Summary in German –

Vielteilchenphysik mit Van-der-Waals-Halbleitern und ultrakalten Atomen

Diese Arbeit untersucht wie das Auftreten von gebundenen Zuständen genutzt werden kann, um Eigenschaften von Quantensystemen zu vermessen und zu manipulieren. Diese Frage wird im Kontext zweier verschiedener Felder – zweidimensionale Materialien und ultrakalte atomare Rydberg-Physik – beleuchtet.

Insbesondere wird untersucht wie Bindungszustände aus Elektronen und Löchern in geschichteten zweidimensionalen Halbleitern verwendet werden können um die Streueigenschaften von Ladungsträgern und Exzitonen zu verändern. Hier wird durch eine numerische Analyse von Drei-Teilchen Zuständen gefunden, dass die Mechanismen von Feshbach Resonanzen, welche aus dem Kontext ultrakalter Quantengase bekannt sind, auf das Gebiet zweidimensionaler Halbleiter ausgedehnt werden können, dort jedoch auch grundlegende Unterschiede aufweisen, wie z.B. die Notwendigkeit der Aufgabe der üblichen Definition der Resonanzbreite.

Weiter wird die Verwendung ultra-langreichweitiger Rydbergmoleküle – gebundene Zustände aus Atomen und Rydbergatomen – als Sonden für Korrelationen in ultrakalten Quantengasen untersucht. Hierbei wird die wohldefinierte Bindungslänge dieser Moleküle, deren optische Anregbarkeit und die Separation der Zeit- und Energieskalen der Molekül-Formierung und der typischen Dynamik innerhalb von Systemen ultrakalter Quantengase ausgenutzt. Insbesondere wird ein direkter Zusammenhang zwischen der Paarkorrelationsfunktion und dem spektralen Gewicht des Dimer-Rydbergmoleküls im Absorptionsspektrum gefunden.

– Summary in English –

Many-Body Physics with Atomically Thin Semiconductors and Ultracold Atoms

This thesis investigates how the emergence of bound states can be used to modify and sense properties of quantum systems. This question is addressed in the context of two different fields – two-dimensional materials and ultracold atomic Rydberg physics.

In particular it is studied how charged bound states of electrons and holes in a system of stacked two-dimensional semiconductors can be used to manipulate and control scattering properties of excitons and charge carriers. Here it is found by a first-principle calculation that the mechanism of Feshbach resonances as known from ultracold atoms extends to atomically thin semiconductors with some important differences as, e.g., the necessity to discard the usual definition of the resonance width.

Further the use of Rydberg molecules – bound states of atoms and Rydberg atoms – as probes of ultracold atoms is investigated. In particular, a connection between the pair correlation function and the spectral response of the Rydberg-dimer molecule is found. The separation of time and energy scales of the typical system dynamics in ultracold atoms and the molecule formation in addition to their well defined molecular binding length allows to use these molecules as a probe of inter-particle distances in ultracold gases.

Table of contents

1. Introduction

Microscopic interactions and the individual properties of the constituents of matter determine their collective macroscopic behavior. Imagine an ensemble of water molecules. Depending on temperature and pressure (or their kinetic, vibrational energies and interparticle spacings) they can either be found in a solid, liquid or gaseous collective state. Analogously, in quantum matter – a regime where quantum mechanical effects become essential to describe the physical state – such as superfluids [1, 2] or supersolids [3, 4], microscopic properties of particles and their interplay lead to the formation of macroscopic collective quantum states that may comprise a large number of particles. This transition from few-body microscopic interactions to the emergence of many-body states and phases is essential for the understanding of matter and appears in many different areas of current research such as quantum spin liquids [5, 6], kinetic magnetism [7, 8], dipolar supersolids [9] or quantum simulators of strongly correlated quantum matter [10].

The underlying theoretical description of interacting many-body systems is itself often extremely challenging, as in general Schrödinger equations for more than two interacting particles do not have analytical solutions and the numerical complexity of classical implementations grows exponentially with the number of particles being involved. The number of exactly solvable problems is rather small forcing us to understand nature in terms of approximations such as perturbative descriptions [11], mean-field theories [12], Monte-Carlo methods [13] and renormalization group approaches [14, 15], or to rely on a clever ansatz for the physical state we wish to describe such as matrix product states and projected entangled pair states [16, 17] or variational states [18]. Often finding effective descriptions such as in the case of the theory of superconductivity [19] (describing the binding of Cooper pairs by an effective exchange of phonons) or – going back to the example of an ensemble of water molecules – the classical theories of thermodynamics [20] or fluids [21] (both describing matter in terms of continuous mean quantities rather than treating particles individually) deepens our understanding of physics. The classical examples illustrate the power of effective models on an intuitive level; even long before the existence of atoms and molecules had become part of our perception of the world, effective theories existed that were able to describe their collective macroscopic behavior.

One prime example of a quantum many-body system that, however, has an exact solution is the heavy impurity problem in the limit of infinite mass [22–24]. Here a single immobile impurity interacts with a bath of indistinguishable particles. This system seems to be rather simple on first glance but gives rise to a variety of nontrivial effects. The interaction of the impurity with the neighboring particles leads to a dressing of the

impurity by bath excitations, resulting in the formation of collective quantum states involving many particles – called polarons[1]. Such situations can be found in various fields of physics ranging from condensed matter [25, 26] and ultracold atoms [27, 28] to high energy physics (where particles get dressed by vacuum fluctuations leading to the lamb shift [29] which, e.g., modifies the energies of electronic states within the the hydrogen atom). This allows to study the reoccurring concept of quantum impurities using one platform (e.g., ultracold atoms) and thereby also gaining insight in other fields of physics. In this context ultracold atoms take a special role. This is rooted in the ability to control interaction strengths between atoms using Feshbach resonances allowing to investigate the emergence of complex quantum states when interaction strengths are tuned from zero to finite values (e.g., between the impurity and its environment) and thereby controllably entering a regime of strong interactions.

The success of ultracold atoms as platform for quantum simulation also builds on the universality of low-energy scattering, i.e., the fact that the properties of scattering particles with low momenta are based purely on their asymptotic behavior. All features of the relevant scattering states are fully characterized by a single parameter – the scattering length [30]. In this sense low-energy scattering of particles is universal as the microscopic details of scattering potentials do not affect their asymptotic behavior. This can result in two completely different potentials to be indistinguishable when only observing low-energy scattering properties. Hence, allowing unbound particles to be treated as if they would interact via contact interactions with a coupling strength that reproduces the correct phase shifts (i.e., scattering lengths). Therefore different platforms realizing the same interacting many-body systems behave similarly within their respective low-energy regime[2].

On the other hand the description of bound states typically depends on the knowledge of the full interaction potential. This sets the scope for this thesis where we investigate how few-body bound states that are formed during the scattering process of their constituents allow to modify, control or probe properties of the many-body system in which they are formed (i.e., tune scattering properties or measure correlations). To this end, we will study universal connections between the, at first sight, vastly different fields of two-dimensional materials and ultracold atoms. We will focus on specific examples that show how knowledge from one field can be transfered to the other. In the following we give a short outline of this thesis.

[1] This name dates back to Landau [25] who introduced the concept of electrons polarizing their environment by displacing atoms when moving through a lattice.

[2] This is the basic idea behind quantum simulation [31, 32].

Outline

Part I: tunable exciton-electron scattering in atomically thin semiconductors

The first part of this thesis investigates two-dimensional exciton-electron scattering in atomically thin semiconductors. We focus on the question how exciton-electron Feshbach resonances translate to two-dimensional systems and how they can be understood from a microscopic few-particle point of view.

In Chapter 2 we start by giving a short overview of Feshbach resonances in ultracold atoms and transition metal dichalcogenides (TMDs). These atomically thin semiconductors are a class of van der Waals materials that posses semiconducting band gaps. The two-dimensional nature of these materials supports the formation of deeply bound excitonic states. The interactions between these excitons and free charge carriers are typically fixed by material parameters which limits the range of application. Conversely, the coupling of scattering states and bound states in ultracold atoms, leading to the phenomenon of Feshbach resonances, allows for a manipulation of the scattering properties.

In Chapter 3 we investigate how two-dimensional exciton-electron Feshbach resonances and consequently tunability of interaction strengths result from the interactions of two electrons and a hole in a TMD heterostructure. In the context of van der Waals materials this concept is new [33] and was lacking an understanding based on first principles which is presented in Section 3.2. We also introduce a toy model for the description of a two-dimensional heavy impurity in a Fermi sea and investigate the consequences of the tunability of interaction strengths via Feshbach resonances on the optical signatures of the respective two-dimensional Fermi-polaron problem. We conclude this chapter in Section 3.3 by an investigation of a two-dimensional Hubbard-type model of excitons interacting with a lattice of electrons formed by a charge-ordered state in two-dimensional semiconductors. Here interaction strengths between the exciton and the lattice sites can be tuned using the previously introduced Feshbach resonance, giving rise to tunable excitonic band structures.

In Chapter 4 we develop an ultracold atom inspired effective many-body model for exciton-electron scattering in TMDs and find a remarkably good agreement with the energies obtained from a few-body calculation. This further strengthens the analogy between ultracold atoms and two-dimensional materials.

Part II: Rydberg excitations as probe of quantum matter

The second part of this thesis is dedicated to the investigation of a particular bound state – an ultralong-range Rydberg molecule (ULRRM) – formed by a Rydberg atom and a ground state atom and how it can be used to probe correlations in ultracold quantum gases.

In Chapter 5 we review the basic concepts necessary to understand the interactions between Rydberg atoms and ground state atoms that lead to the formation of ULRRMs. In Chapter 6 we develop an approximate ansatz of ULRRM dimers in an ideal Fermi

sea which is used to calculate the dimer absorption signal using Fermi's golden rule. We find a direct connection between the absorption strength of the ULRRM-dimer and the pair correlation function of the quantum gas in which it was created. This allows to use Rydberg excitations as probe of correlations in ultracold gases on length scales given by the Rydberg radius, which is typically in the sub-optical regime.

In Chapter 7 this novel method of probing correlations in ultracold atoms using Rydberg excitations is theoretically applied to a dilute gas of Feshbach molecules and a heavy impurity in a Fermi gas. In the first case Rydberg spectroscopy grants access to the Feshbach-molecular wave function. In the second scenario the Rydberg spectroscopic measurement of correlations allows to map the density profile of the polaron cloud. This shows how Rydberg spectroscopy can be used to in-situ detect and study correlations in experimental setups.

In Chapter 8 we switch gears and investigate the loss dynamics of atoms from a BEC when one of the atoms is excited into a Rydberg state. Therefore we use a semiclassical theory where we solve the classical equations of motion for an ensemble of point-like particles. We compare our numerical results to the experimental findings of [34] and find good qualitative agreement.

Finally, Chapter 9 concludes the thesis, where we summarize its results and present an outlook on future directions.

Part I.

Tunable Exciton-Electron Scattering in Atomically Thin Semiconductors

Part I is based on the publications [P3] and [P5].
Additional unpublished material is discussed in Sections 3.1.1 and 3.3 and Chapter 4.

Low-energy scattering of particles is universal across physics, ranging from ultracold atoms to solids and high-energy physics. This allows to observe the same phenomena and similar features in entirely different areas of physics [35]. With their capability to act as quantum simulators ultracold atoms take a special role. This is in particular based on the astonishing control over interatomic scattering properties [32, 36] by making use of Feshbach resonances [37, 38].

In solid state physics, on the other hand, interactions between particles (charge carriers and emerging quasiparticles, such as excitons, phonons, or plasmons) are typically fixed by material properties with no possibility to easily tune and control interactions in a given sample. This naturally limits the versatility of solid-state systems as platform to study and simulate universal physics. The recent experimental observation of a Feshbach resonance in twisted bilayer TMDs [33] prompts questions about their microscopic origin and to which extent their tunability allows the exploration of many-body physics even beyond the reach of ultracold atomic quantum gases.

In this first part of this thesis, we investigate the emergence of tunable exciton-electron scattering in multi-layered heterostructures of two-dimensional materials. We start with a short reminder on Feshbach resonances in ultracold atoms in three dimensions and a short review of two-dimensional semiconductors. Then we show how Feshbach resonances between electrons and excitons in two-dimensional materials arise from a microscopic first-principle analysis of the underlying three-body problem. We specifically focus on how layer hybridization of excitons can lead to the emergence of Feshbach resonances that allow to tune interactions between electrons and both short-lived intralayer, as well as long-lived interlayer excitons. The first type of resonance gives access to the sensing of charge correlations via optical injection of excitons. The latter brings tunable interactions to Bose-Fermi mixtures consisting of electrons and long-lived interlayer excitons (bosons). This opens the avenue to explore Bose-Fermi mixtures in solid-state systems in regimes that were previously not accessible in ultracold atom experiments (due to their chemical instability [39]) by bringing fully controllable interactions to the field of two-dimensional semiconductors.

Based on this new possibility of tunable interactions between excitons and charges we investigate their implications for an exciton interacting with a charged-ordered many-body state. We find that the tunability of exciton-electron interactions leads to tunable excitonic band structures. Further we derive an effective description for two-dimensional Feshbach resonances motivated by two-channel models commonly used in ultracold atoms.

2. Overview: Van der Waals Materials and Feshbach Resonances

The goal of this chapter is to provide a short overview of transition metal dichalcogenides (TMDs) – a group of van der Waals materials with semiconducting band gaps – and Feshbach resonances in ultracold atoms. In Chapter 3 the combination of both fields will provide the theoretical foundation for the microscopic understanding of tunable exciton-electron scattering in TMD heterostructures.

2.1. Two-Dimensional Semiconductors

Van der Waals materials provide a fast evolving platform for the experimental investigation of strongly correlated quantum matter. Over the past years developments in the field of van der Waals heterostructures have led to new types of experiments allowing to study Mott phases [40, 41], insulating density waves [42–44], excitonic insulators [45], Wigner crystals [40, 46, 47], the quantum anomalous Hall effect [48], polaron-polariton-cavity physics [26] and fractional Chern insulators [49].

Monolayer TMDs – atomically thin semiconductors [50] – are a subgroup of van der Waals materials. A detailed review on the physics of these materials can be found in [51]. Their three-dimensional bulk versions consist of parallelly aligned crystalline monolayers which are held together by van der Waals forces. The robust mechanical properties of monolayers (caused by the strong inter-atomic binding within the layers) and the relatively weak adhesion between individual layers allow to extract single atomically thin sheets of these materials by exfoliation[1] [53]. Such monolayers can be stacked on top each other in a modular way [54], enabling the engineering of multilayer van der Waals heterostructures with specific properties. In this way a semiconducting monolayer can be, e.g., encapsulated by insulators, hexagonal boron nitride (hBN), or gated by a layer of graphene, which leads to ability to investigate and make use of the existence of deeply-bound two-dimensional excitons.

A TMD monolayer has a width of about 0.7 nm ($MoSe_2$) and has a crystalline structure with transition metal atoms being located in the central symmetry plane and chalcogen atoms located above and below (see Fig. 2.1a,b). Each transition metal atom (e.g., Mo,

[1] There are also other methods for creating layered structures of van der Waals materials such as chemical vapor deposition [52].

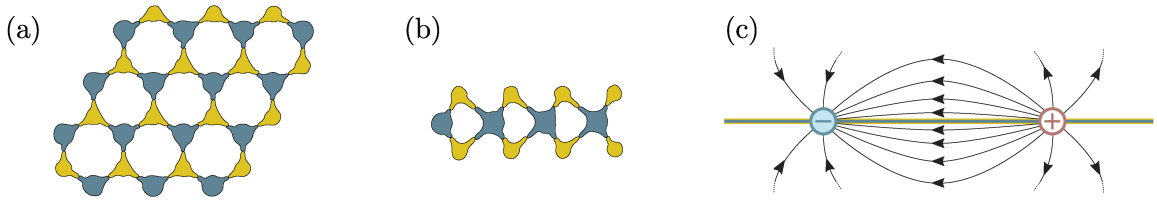

Figure 2.1.: Sketch of the crystal structure of a TMD monolayer; (a) top view, (b) side view along the axis where neighboring transition metal atoms align (freely based on [55]). The positions of transition metal atoms (e.g., Mo, W) are marked in blue and the ones of dichalcogenide atoms (e.g., S, Se) in yellow. The latter are pairwise aligned in the top view. (c) Illustration of the electrical field lines between an electron (blue) and a hole (red) in a TMD monolayer. Most of the field lines are out of plane (and pass through, e.g., vacuum).

W) is surrounded by six chalcogen atoms and each chalcogen atom (e.g., S, Se) neighbors three transition metal atoms, as reflected in their chemical formulas of, e.g., $MoSe_2$.

TMDs have direct band gaps [50] that appear at the high symmetry points K and K' within the Brillouin zone and are labeled K and K' valley respectively[2] (see Fig. 2.2). At these points electrons can be excited from the valence to the conduction band by the absorption of a photon of matching energy. This process annihilates an electronic state in the valence band leaving a 'hole' (a positively charged state) in the valence-band Fermi sea of electrons. The hole acts in a sense like the antiparticle of the annihilated electron [58].

Thus the absorption of a photon can create a pair of positive and negative charge which attract each other like electrons and positrons or like the proton and electron within a hydrogen atom. The bound state of a hole and an electron is a quasiparticle[3] called 'exciton'. It is found that spectroscopic results can be rather well described by an effective-mass model [51] where one extracts an effective mass for electrons and holes from the harmonic curvatures of the respective band extrema. Later we will follow this approach by treating electrons and holes in TMD monolayers to behave like particles with effective masses. The excitons in the different valleys can be addressed individually using circular polarized light. The K-valley exciton couples to σ^--polarized photons while the K'-valley exciton couples to σ^+ polarization [59–62].

In contrast to excitons in three-dimensional bulk semiconductors like gallium arsenide or cuprous oxide, only a small fraction of the electrical field lines between the electron and hole are located within the atomically thin monolayer as most of the electrical field lines are out of plane. An illustration of the electric field between the electron and hole can be found in Fig. 2.1(c). The screening of the out-of-plane electric field lines

[2]Theoretical calculations of band structures typically use density functional theory (DFT) [56, 57].

[3]I.e., an excitation out of a vacuum with a well defined dispersion relation that approximately has a well-defined quantum statistics.

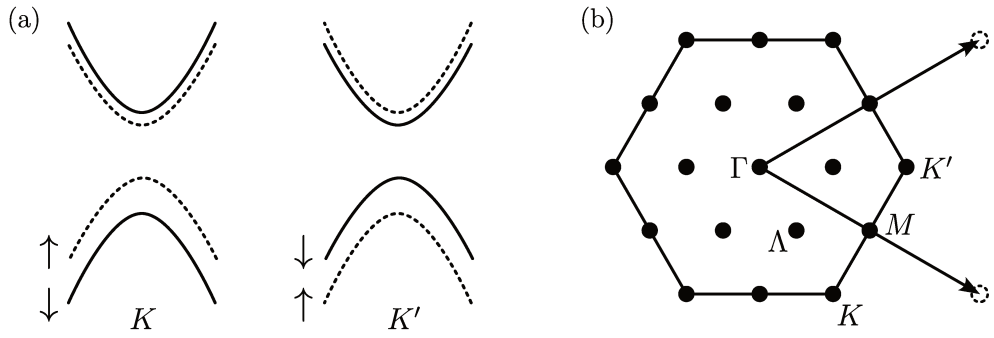

Figure 2.2.: (a) Illustration of the direct band gaps at the K and K' valleys of the band structure for $MoSe_2$ (freely based on [51]). The valence and conduction bands are split due to spin-orbit coupling where the valence band splitting is significantly larger than the conduction band splitting [66]. (b) Illustration of the Brillouin zone and symmetry points for a two-dimensional triangular lattice (freely based on [67]).The high symmetry points can be derived from the crystalline structure of the monolayer crystal (MoS_2: space group $P6m2$ [68]). The arrows mark the reciprocal lattice vectors.

[63–65] caused by the two-dimensional geometry of the system results in a modification of the Coulomb interaction potential. This screening can additionally be amplified by constructing heterostructures where the TMD monolayer is encapsulated by insulators. In the limit of vanishing layer thickness the modified interaction potential of two charges in a single monolayer is given by the Rytova-Keldysh potential [63, 64]

$$V(r) = -\frac{\pi e^2}{2r_0}\left[H_0\left(\frac{r}{r_0}\right) - Y_0\left(\frac{r}{r_0}\right)\right] , \tag{2.1}$$

where H_0 and Y_0 are the Struve and Neumann functions, and $r_0 = \alpha_{2d}/2$ is the screening length due to the polarizability α_{2d} of the atomically thin layer.

The excitonic binding energies resulting from this interaction potential are enhanced by up to two orders of magnitude compared to bulk semiconductors [69–71] justifying many-body theories approximating excitons as point-like particles by neglecting its internal structure. Fig. 2.3 shows the energies and radial states of excitons of different angular momenta in a $MoSe_2$ monolayer calculated in an effective mass model by numerically diagonalizing the radial Schrödinger equation

$$\left[-\frac{\hbar^2}{2\mu}\left(\partial_r^2 + \frac{1}{r}\partial_r\right) + V(r) + \frac{\hbar^2}{2\mu}\frac{m^2}{r^2}\right]\psi_m(r) = E\psi_m(r) , \tag{2.2}$$

with reduced mass μ and angular momentum m. The extent of the s-wave ground state is approximately 2 nm. The ground-state energy increases with angular momentum and the growing centrifugal barrier increasingly pushes the maximum of the radial wave function towards larger radii.

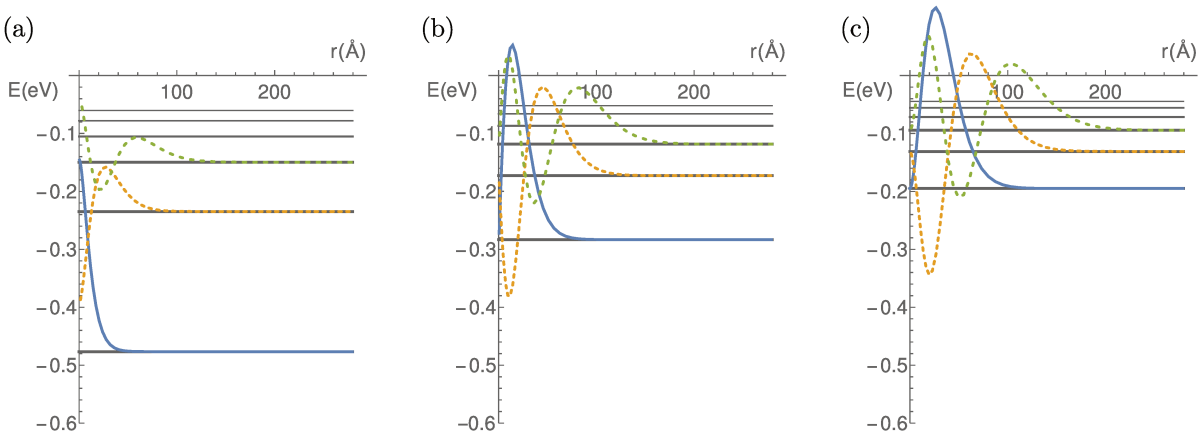

Figure 2.3.: Exciton binding energies (gray solid lines) and radial wave functions (colored lines) in a $MoSe_2$ monolayer for different angular momenta (a) $m = 0$, (b) $m = 1$ and (c) $m = 2$. The two-dimensional centrifugal potential for $m \neq 0$ causes the wave functions to be extended to larger radii.

Virtual electron-hole recombination in a many-body environment and the resulting exchange interactions modify the potential presented here which is the result of solely considering direct Coulomb interactions. The electrodynamic back-action of the excitonic dipole on the exciton itself additionally contributes to the interactions (known as long-range exchange interaction) [51]. The ratio of direct and exchange interactions is of the order 10:1 [72]. In our analysis of the exciton-electron three-body problem presented in Section 3.2 we will neglect exchange interactions and solely focus on direct Coulomb interactions.

In TMDs the interactions between charges are typically fixed by material parameters. On the other hand, in ultracold atoms, the ability to couple different scattering channels and energetically shifting them with respect to each other allows to control interaction strengths. In the next section we give a short introduction to the underlying concept within the context of ultracold atoms. Then in Chapter 3 we will translate this mechanism to TMDs.

2.2. Tunable Interactions in Ultracold Atoms

In the following we give a short review of Feshbach resonances [37, 38] as employed in ultracold atoms. They represent the elementary tuning knob for controlling interactions between atoms and thereby enable ultracold atoms to serve as a versatile platform for quantum simulation. A detailed coverage of Feshbach resonances can be found in [73, 74]. Here we state the idea and give a short overview of how the tuning of the scattering length a between ultracold atoms can be represented using a two-channel model.

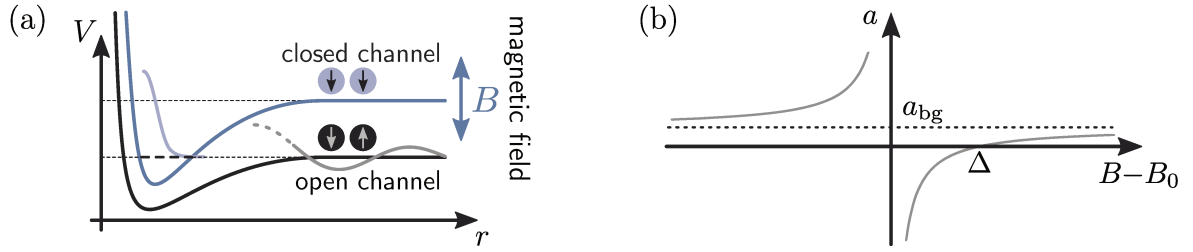

Figure 2.4.: (a) Illustration of open and closed channel of Feshbach resonances. Thin dashed lines mark scattering thresholds and the bold dashed line marks the energy of the closed-channel bound state. An external magnetic field B allows to shift the energy difference between the two channels. Sketches of the bound state and scattering wave function are also depicted in the figure. (b) Schematic showing the typical behavior of the scattering length for particles in the open channel according to Eq. (2.3).

2.2.1. Feshbach Resonances

Scattering resonances arise from the existence almost-bound states of the scattering particles which result from the coupling of a bound state in a so-called close scattering channel to to continuum states of the asymptotic (open) scattering channel. Generally this allows to change the properties of the scattering process (i.e., the phase shift). In the context of Feshbach resonances [37, 38, 75, 76] this occurs when two particles scatter with a certain kinetic energy and simultaneously (after a change of an internal degree of freedom) are able to form a resonant bound state. For magnetically tuned Feshbach resonances this is achieved by allowing the atoms to switch between two different interaction potentials belonging to different hyperfine manifolds and applying an external magnetic field B to shift the energies of the different hyperfine (spin) states via the Zeeman effect (see Fig. 2.4a).

Thus atoms can be in a scattering state for one spin configuration and in a bound state after (virtually) changing their spin state. The energetically lower scattering potential in which the particles enter the scattering process is commonly labeled as the open channel. Due to the fact that the bound state is formed in a potential with an energetically higher scattering threshold (see Fig. 2.4a) and particles can not leave the scattering process in this channel because of energy conservation, one refers to this scattering potential as the closed channel.

When B is tuned in a way that the zero-momentum scattering state of the open channel and the bound state in the closed channel (dressed by scattering states of the open-channel) have the same energy it is found that the scattering length in the open channel diverges. In the regime around the resonance where the bound and the scattering state are energetically very close to each other the scattering length changes significantly with their energy detuning and is positive (negative) when the bound state is energetically below (above) the open channel scattering threshold. This mechanism can be used to

realize all scattering lengths above/below the respective background scattering length by fine tuning the magnetic field around the resonance. The parametrization of the dependence of the scattering length a in terms of the magnetic field B

$$a(B) = a_{\mathrm{bg}} \left(1 - \frac{\Delta}{B - B_0}\right) \tag{2.3}$$

was first described in [77]. Here the background scattering length a_{bg} is given by the asymptotic behavior far away from the resonance and the resonance width Δ is defined by the distance between the resonance position B_0 and the magnetic field value where the scattering length a vanishes. The typical behavior of the scattering length around the resonance is sketched in Fig. 2.4(b).

Later we will see that the resonance width Δ, which is an important characteristics of three-dimensional Feshbach resonances, loses its meaning in a two-dimensional setting as here the resonance position and the zero crossing of the scattering length always coincide. Thus the resonance width Δ cannot be used in the context of two-dimensional materials to characterize Feshbach resonances.

2.2.2. Two-Channel Model

More insight into the physics of Feshbach resonances can be obtained by studying an effective two-channel model [78, 79]

$$\hat{H} = \underbrace{\sum_{\boldsymbol{k},\sigma} \varepsilon_{\boldsymbol{k}}\, \hat{c}^{\dagger}_{\boldsymbol{k},\sigma} \hat{c}_{\boldsymbol{k},\sigma} + \sum_{\boldsymbol{k}} \left(\frac{\varepsilon_{\boldsymbol{k}}}{2} + \nu_B\right) \hat{b}^{\dagger}_{\boldsymbol{k}} \hat{b}_{\boldsymbol{k}}}_{\hat{H}_0} + \underbrace{\frac{g}{\sqrt{V}} \sum_{\boldsymbol{k},\boldsymbol{q}} \left(\hat{b}^{\dagger}_{\boldsymbol{q}} \hat{c}_{\boldsymbol{k}+\boldsymbol{q}/2,\downarrow} \hat{c}_{-\boldsymbol{k}+\boldsymbol{q}/2,\uparrow} + \mathrm{h.c.}\right)}_{\hat{V}} , \tag{2.4}$$

here for simplicity in absence of background scattering. The $\hat{c}_{\boldsymbol{k}}$-operators create/annihilate an atom in the open channel with momentum $\boldsymbol{k}$, hyperfine spin $\sigma \in (\uparrow, \downarrow)$ and kinetic energy $\varepsilon_{\boldsymbol{k}} = \hbar^2 \boldsymbol{k}^2 / 2m$. The $\hat{b}_{\boldsymbol{k}}$-operators are compound operators that create/annihilate a bound state of two atoms in a momentum mode $\boldsymbol{k}$ with energy ν_B in the closed channel. As the bound state is formed out of two atoms its mass is twice the mass of an atom and hence the kinetic energy is given by $\varepsilon_{\boldsymbol{k}}/2$. The non-interacting Hamiltonian $\hat{H}_0$ describes the total kinetic energy of the system. The last term $\hat{V}$ couples the two channels by a coupling constant[4] g.

We now consider the center-of-mass zero-momentum sector of the Hilbert space and ask for the transition probabilities of an initial scattering state $\hat{c}^{\dagger}_{\boldsymbol{k},\downarrow} \hat{c}^{\dagger}_{-\boldsymbol{k},\uparrow} |0\rangle = |\boldsymbol{k}, -\boldsymbol{k}\rangle$ into a state $|\boldsymbol{k}', -\boldsymbol{k}'\rangle$. The transition matrix $\hat{T}$ describing this process can be expressed via the Lipmann-Schwinger equation

$$\hat{T} = \hat{V} + \hat{V}\, \hat{G}\, \hat{T} , \tag{2.5}$$

[4] If one would consider scattering at higher momenta one would need to include the momentum dependency of the coupling parameter $g_{\boldsymbol{k}}$ in order to resolve microscopic details of the interaction potentials. Here we consider the limit $k \to 0$ where $g_{\boldsymbol{k}} \approx g = \mathrm{const}$.

where $\hat{V}$ is the third term in Eq. (2.4) and $\hat{G} = 1/(E - \hat{H}_0 + \mathrm{i}\epsilon)$ the free Green's function. The transition element is then given by

$$\begin{aligned}
\langle \boldsymbol{k}', -\boldsymbol{k}'| \hat{T} |\boldsymbol{k}, -\boldsymbol{k}\rangle &= \langle \boldsymbol{k}', -\boldsymbol{k}'| \hat{V} + \hat{V}\,\hat{G}\,\hat{T} |\boldsymbol{k}, -\boldsymbol{k}\rangle \\
&= \langle \boldsymbol{k}', -\boldsymbol{k}'| \hat{V} |\boldsymbol{k}, -\boldsymbol{k}\rangle \\
&+ \langle \boldsymbol{k}', -\boldsymbol{k}'| \hat{V}\hat{G}\hat{V} |\boldsymbol{k}, -\boldsymbol{k}\rangle \\
&+ \langle \boldsymbol{k}', -\boldsymbol{k}'| \hat{V}\hat{G}\hat{V}\hat{G}\hat{V} |\boldsymbol{k}, -\boldsymbol{k}\rangle \\
&+ ... \\
&= \langle \boldsymbol{k}', -\boldsymbol{k}'| \hat{V} \sum_{n=0}^{\infty} (\hat{G}\hat{V})^{2n} \hat{G}\hat{V} |\boldsymbol{k}, -\boldsymbol{k}\rangle \ .
\end{aligned} \tag{2.6}$$

Here all terms where the application of the operators converts a scattering state into a bound state (whenever $1 + 4n$ operators appear) vanish, leading to the expression in the last line of the equation. This expression has the advantage that $\hat{G}\hat{V} |\boldsymbol{k}, -\boldsymbol{k}\rangle$ is an eigenstate of each term $(\hat{G}\hat{V})^{2n}$. To see this one realizes that during the evaluation of Eq. (2.6) four different types of terms may occur. Terms where $\hat{V}$ acts on a scattering state $|\boldsymbol{k}, -\boldsymbol{k}\rangle$

$$\begin{aligned}
\hat{V} |\boldsymbol{k}, -\boldsymbol{k}\rangle &= \frac{g}{\sqrt{V}} \sum_{\boldsymbol{p},\boldsymbol{q}} \left(\hat{b}^\dagger_{\boldsymbol{q}} \hat{c}_{\boldsymbol{p}+\boldsymbol{q}/2,\downarrow} \hat{c}_{-\boldsymbol{p}+\boldsymbol{q}/2,\uparrow} + \text{h.c.} \right) \hat{c}^\dagger_{\boldsymbol{k},\downarrow} \hat{c}^\dagger_{-\boldsymbol{k},\uparrow} |0\rangle \\
&= \frac{g}{\sqrt{V}} \sum_{\boldsymbol{p},\boldsymbol{q}} \hat{b}^\dagger_{\boldsymbol{q}} \delta_{\boldsymbol{p}+\boldsymbol{q}/2,\boldsymbol{k}}\, \delta_{-\boldsymbol{p}+\boldsymbol{q}/2,-\boldsymbol{k}} |0\rangle \\
&= \frac{g}{\sqrt{V}} \hat{b}^\dagger_{\boldsymbol{0}} |0\rangle \ ,
\end{aligned} \tag{2.7}$$

terms where $\hat{G}$ acts on a scattering state $|\boldsymbol{k}, -\boldsymbol{k}\rangle$

$$\begin{aligned}
\hat{G} |\boldsymbol{k}, -\boldsymbol{k}\rangle &= \frac{1}{E - \hat{H}_0 + \mathrm{i}\epsilon} \hat{c}^\dagger_{\boldsymbol{k},\downarrow} \hat{c}^\dagger_{-\boldsymbol{k},\uparrow} |0\rangle \\
&= \frac{1}{E - \varepsilon_{\boldsymbol{k}} + \mathrm{i}\epsilon} |\boldsymbol{k}, -\boldsymbol{k}\rangle \\
&= G_0(E, \boldsymbol{k})\ |\boldsymbol{k}, -\boldsymbol{k}\rangle \ ,
\end{aligned} \tag{2.8}$$

terms where $\hat{V}$ acts on a bound state $\hat{b}^\dagger_0 |0\rangle$

$$\begin{aligned}
\hat{V}\hat{b}^\dagger_0 |0\rangle &= \frac{g}{\sqrt{V}} \sum_{\boldsymbol{p},\boldsymbol{q}} \left(\hat{b}^\dagger_{\boldsymbol{q}} \hat{c}_{\boldsymbol{p}+\boldsymbol{q}/2,\downarrow} \hat{c}_{-\boldsymbol{p}+\boldsymbol{q}/2,\uparrow} + \text{h.c.} \right) \hat{b}^\dagger_0 |0\rangle \\
&= \frac{g}{\sqrt{V}} \sum_{\boldsymbol{p},\boldsymbol{q}} \hat{c}^\dagger_{\boldsymbol{p}+\boldsymbol{q}/2,\downarrow} \hat{c}^\dagger_{-\boldsymbol{p}+\boldsymbol{q}/2,\uparrow} \delta_{\boldsymbol{q},\boldsymbol{0}} |0\rangle \\
&= \frac{g}{\sqrt{V}} \sum_{\boldsymbol{p}} |\boldsymbol{p}, -\boldsymbol{p}\rangle \ ,
\end{aligned} \tag{2.9}$$

and terms where terms where $\hat{G}$ acts on a bound state $\hat{b}_0^\dagger |0\rangle$

$$\begin{aligned}\hat{G}\hat{b}_0^\dagger |0\rangle &= \frac{1}{E - \hat{H}_0 + \mathrm{i}\epsilon}\, \hat{b}_0^\dagger |0\rangle \\ &= \frac{1}{E - \nu_B + \mathrm{i}\epsilon}\, \hat{b}_0^\dagger |0\rangle \\ &= \mathcal{G}_0(E)\, \hat{b}_0^\dagger |0\rangle \ .\end{aligned} \tag{2.10}$$

Here we have defined

$$\mathcal{G}_0(E) = \frac{1}{E - \nu_B + \mathrm{i}\epsilon} \qquad \text{and} \qquad G_0(E,p) = \frac{1}{E - \varepsilon_{\boldsymbol{p}} + \mathrm{i}\epsilon} \ . \tag{2.11}$$

One now finds that the state

$$\hat{G}\hat{V}\, |\boldsymbol{k}, -\boldsymbol{k}\rangle = \frac{g}{\sqrt{V}}\, \mathcal{G}_0(E)\, \hat{b}_{\boldsymbol{0}}^\dagger |0\rangle \tag{2.12}$$

is an eigenstate of the operator $(\hat{G}\hat{V}\hat{G}\hat{V})^n$, i.e.,

$$\hat{G}\hat{V}\hat{G}\hat{V}\, \hat{b}_{\boldsymbol{0}}^\dagger |0\rangle = \frac{g^2}{V} \mathcal{G}_0(E) \sum_{\boldsymbol{p}} G_0(E, \boldsymbol{p})\, \hat{b}_{\boldsymbol{0}}^\dagger |0\rangle \ . \tag{2.13}$$

For details see Appendix A. We are now in the position to evaluate Eq. (2.6) to arrive at

$$\langle \boldsymbol{k}', -\boldsymbol{k}'|\, \hat{T}\, |\boldsymbol{k}, -\boldsymbol{k}\rangle = \frac{g^2}{V}\, \mathcal{G}_0(E) \sum_{n=0}^{\infty} \left(\mathcal{G}_0(E)\, g^2 \underbrace{\int \frac{\mathrm{d}^3\boldsymbol{p}}{(2\pi)^3} \frac{1}{E - \epsilon_{\boldsymbol{k}} + \mathrm{i}\epsilon}}_{:=\Sigma(E)} \right)^n \ , \tag{2.14}$$

where we identify the self energy

$$\begin{aligned}\Sigma(E) &= \int \frac{\mathrm{d}^3\boldsymbol{p}}{(2\pi)^3} \frac{1}{E - \epsilon_{\boldsymbol{p}} + \mathrm{i}\epsilon} \\ &= \frac{1}{V} \sum_{\boldsymbol{p}} \frac{1}{E - \epsilon_{\boldsymbol{p}} + \mathrm{i}\epsilon} \\ &\approx \frac{1}{V} \sum_{|\boldsymbol{p}|<\Lambda} \frac{1}{E - \epsilon_{\boldsymbol{p}} + \mathrm{i}\epsilon} \ ,\end{aligned} \tag{2.15}$$

with the momentum cutoff Λ. This allows to rewrite the transition matrix element

$$\langle \boldsymbol{k}', -\boldsymbol{k}'|\, \hat{T}\, |\boldsymbol{k}, -\boldsymbol{k}\rangle \approx \frac{1}{V} \frac{1}{\frac{E - \nu_B + \mathrm{i}\epsilon}{g^2} - \frac{1}{V} \sum\limits_{|\boldsymbol{p}|<\Lambda} \frac{1}{E - \epsilon_{\boldsymbol{p}} + \mathrm{i}\epsilon}} \ . \tag{2.16}$$

The transition matrix elements are linked to the scattering amplitude by

$$f_E(\boldsymbol{k},\boldsymbol{k}') = -\frac{\mu}{2\pi\hbar^2}\, V\, \langle \boldsymbol{k}', -\boldsymbol{k}'|\, \hat{T}\, |\boldsymbol{k}, -\boldsymbol{k}\rangle \ , \tag{2.17}$$

with the reduced mass $\mu = m/2$. This expression can be transformed for elastic and on-shell scattering where $|\boldsymbol{k}| = |\boldsymbol{k}'| = k$ and $E = \hbar^2 k^2/2\mu$ to

$$\begin{aligned} f(k) &= \int_0^{2\pi} \mathrm{d}\vartheta\, f_E(\boldsymbol{k},\boldsymbol{k}') \\ &\overset{k\to 0}{=} \frac{1}{\frac{4\pi\hbar^2\nu_B}{g^2 m} - \frac{2\Lambda}{\pi}} \ , \end{aligned} \tag{2.18}$$

with $\vartheta = \angle(\boldsymbol{k},\boldsymbol{k}')$. In the limit $k \to 0$ the scattering length a is direct proportional to the scattering amplitude

$$a = -\lim_{k\to 0} f(k) = -\left(\frac{4\pi\hbar^2\nu_B}{g^2 m} - \frac{2\Lambda}{\pi}\right)^{-1} \ , \tag{2.19}$$

which implies that the scattering length depends on the energy detuning ν_B of the closed-channel molecule with respect to the open-channel scattering threshold.

As we motivated above this energy of the closed-channel bound state can be controlled via an external magnetic field in the context of magnetically tuned Feshbach resonances. Away from the resonance the binding energy of the closed-channel bound state is linearly dependent on the magnetic field via the linear Zeeman effect and can thus be parametrized as

$$\nu_B = \delta_\mu (B - B_c) \ . \tag{2.20}$$

Here δ_μ is the difference of the magnetic moments of the closed-channel bound state and the atoms in the open channel and B_c is the magnetic field strength where the bare closed-channel bound state energy crosses the open-channel scattering threshold [80]. Further one finds

$$\begin{aligned} a^{-1} &= -\frac{4\pi\hbar^2\delta_\mu(B-B_c)}{g^2 m} + \frac{2\Lambda}{\pi} \\ &= \frac{2\Lambda}{\pi} - \frac{4\pi\hbar^2\delta_\mu(B-B_0)}{g^2 m} - \frac{4\pi\hbar^2\delta_\mu(B_0-B_c)}{g^2 m} \\ &\overset{!}{=} -\frac{m r^*}{\hbar^2}\delta_\mu(B-B_0) \ . \end{aligned} \tag{2.21}$$

If one identifies

$$g^2 = \frac{4\pi\hbar^2}{m^2 r^*} \ , \tag{2.22}$$

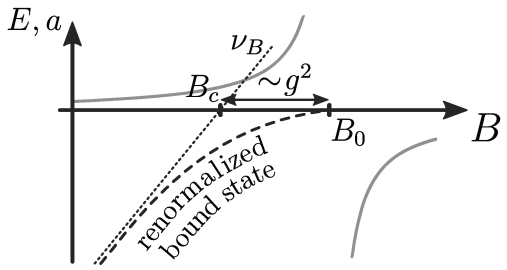

Figure 2.5.: Sketch of bound state energies (dashed lines) and the scattering length (solid gray line) around a Feshbach resonance. Here ν_b is the energy of the closed-channel bound state. The bound state energy is modified due to the coupling g of open and closed channel. Freely based on [80].

where r^* is the Feshbach range, one finds a shifted resonance position of the Feshbach resonance (see Fig. 2.5). The scattering length diverges at the resonance position $B = B_0$ where $1/a = 0$ in Eq. (2.21) such that

$$0 = \frac{2\Lambda}{\pi} - \frac{mr^*}{\hbar^2}\delta_\mu(B_0 - B_c) \qquad \Rightarrow \qquad \delta_\mu(B_0 - B_c) = \frac{2\Lambda\hbar^2}{\pi m r^*} = \frac{g^2 m \Lambda}{2\pi\hbar^2} \ . \tag{2.23}$$

Hence due to the coupling g of open and closed-channel the renormalized ground state is energetically below the bare closed channel-bound state.

In this chapter we have reviewed basic concepts in TMDs and Feshbach resonances that will allow to investigate exciton-electron scattering in TMD heterostructures in Chapter 3. In this course we will identify exciton-electron scattering resonances that resemble the picture of open and closed-channels introduced in the description of ultracold atomic Feshbach resonances. In the context of TMDs anticrossings between exciton-electron bound states (trions) and exciton-electron scattering thresholds will occur due to exciton hybridization resulting from interlayer hole tunneling, leading to the coupling of open and closed scattering channels. This will allow for a microscopic theory of exciton-electron Feshbach resonances in TMD heterostructures.

3. Tunable Exciton-Electron Interactions

In this chapter we show how two-dimensional Feshbach resonances result from an analysis of the two-dimensional exciton-electron scattering in a TMD heterostructure. In doing so, we first introduce a two-dimensional toy model for the scattering of two particles that captures the most important features to obtain tunable scattering phase shifts and use it to model impurity-bath interactions in the Fermi-polaron problem. This allows to understand optical signatures of Feshbach resonances in two dimensions. Afterwards we turn to the concrete example of a TMD heterostructure and show how two-dimensional exciton-electron Feshbach resonances arise from a microscopic theory of electron-hole scattering by solving the underlying three-body problem. This represents a central result of this thesis. Finally we investigate consequences of tunable exciton-electron interactions on excitons interacting with electrons in two-dimensional charge ordered states which arise naturally within TMD heterostructures.

3.1. A Toy Model - Two-Dimensional Scattering Resonances

First we consider two particles that interact via a square-well potential of variable depth. This allows to introduce bound states in a scattering potential while simultaneously monitoring the scattering wave functions. The analysis of this simple model[1] provides insights into scattering resonances in two-dimensional systems as it allows to calculate scattering phase shifts when new bound states are introduced into a two-body interaction potential. In Section 3.2 the same procedure will be applied to the three-body problem allowing to extract exciton-electron phase shifts.

We consider the relative two-body Hamiltonian

$$\left[\frac{\hat{\boldsymbol{p}}^2}{2\mu} + V(\hat{\boldsymbol{r}})\right] \Psi(\boldsymbol{r}) = E\Psi(\boldsymbol{r}) \ . \tag{3.1}$$

Here $\boldsymbol{r}$ is the relative coordinate between the particles, μ is the reduced mass and we

[1] The found mechanism is valid on a more general basis due to the universality of low-energy scattering.

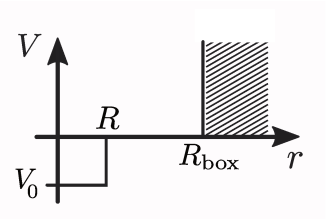

Figure 3.1.: Sketch of the radial potential landscape of the two-dimensional square-well-potential toy model. The infinite potential for $r > R_{\mathrm{box}}$ imposes hard-wall boundary conditions on the radial wave functions.

assume vanishing total momentum. The interaction potential reads

$$V(\boldsymbol{r}) = \begin{cases} V_0 & \text{if } |\boldsymbol{r}| \leq R \\ 0 & \text{else} \end{cases} . \tag{3.2}$$

To get grip on this problem numerically[2], we confine the system in a quantization box by demanding $V(\boldsymbol{r}) = \infty$ if $R_{\mathrm{box}} < |\boldsymbol{r}|$ and choose $R_{\mathrm{box}} \gg R$. Fig. 3.1 shows a sketch of the radial potential landscape of the toy model, with V_0 being the depth and R the range of the potential. The circular two-dimensional quantization box with radius R_{box} imposes hard-wall boundary conditions on the radial wave functions. We separate radial and angular wave functions by the ansatz

$$\Psi(\boldsymbol{r}) = \psi_m(r)\mathrm{e}^{\mathrm{i}m\varphi} \tag{3.3}$$

leading to the radial Schrödinger equation

$$\left[-\frac{\hbar^2}{2\mu}\left(\partial_r^2 + \frac{1}{r}\partial_r\right) + V(r) + \frac{\hbar^2}{2\mu}\frac{m^2}{r^2}\right]\psi_m(r) = E\psi_m(r) \ , \tag{3.4}$$

and restrict the following analysis on the s-wave sector of the Hilbert space containing the wave functions with zero angular momentum, i.e., $m = 0$. The Hamiltonian is implemented numerically where we make use of finite difference coefficients to represent the momentum operator and use exact diagonalization to calculate the low-energy spectrum and the corresponding eigenstates of Eq. (3.4).

A comparison of the resulting radial two-body wave functions (blue) and the corresponding non-interacting wave functions (black) can be found in Fig. 3.2. It shows three different choices of V_0 around the emergence of the second bound state at V_{res} in the interaction potential for a fixed range $R \ll R_{\mathrm{box}}$ (note, R is so small that it is not visible on the scale of the r-axis).

In (a) we can see how the scattering wave functions are pushed out of the potential well (i.e., $\delta > 0$). For excited states the particles repel each other despite the attractive

[2]Despite the existence of an analytical solution of this problem we apply the same numerical method as developed for the analysis of the three-body problem presented in the next section.

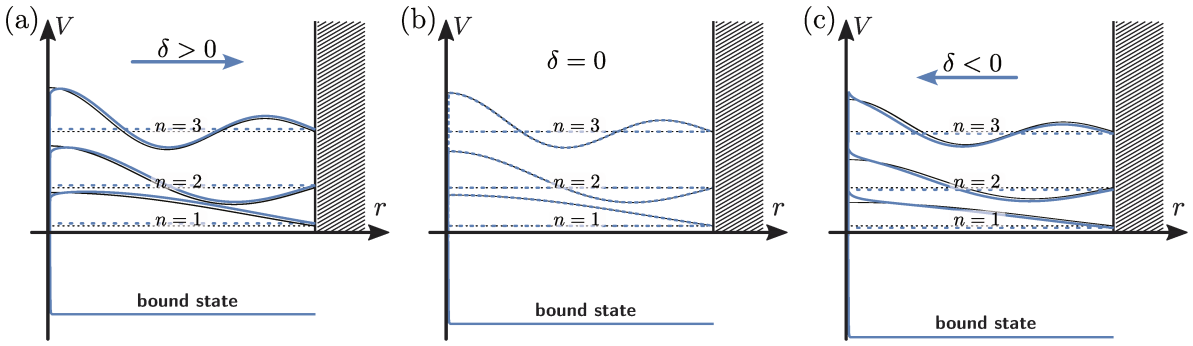

Figure 3.2.: Illustration of the relative radial two-body wave functions of a two-dimensional square-well interaction potential for $R \ll R_{\text{box}}$. Blue (interacting): wave functions of the system with square-well potential. Black (non-interacting): wave functions without square-well potential. The potential depth V_0 is chosen around the value V_{res} where the second bound state is created in the interaction potential. In (a) one bound state exists for $V_0 \gtrsim V_{\text{res}}$ and the interacting scattering wave functions are pushed out of the square-well potential. In (b) the interacting energy levels match for $V_0 = V_{\text{res}}$ and the long-distance behavior of the interacting states coincides with their non-interacting counterparts. In (c) two bound states exist for $V_0 \lesssim V_{\text{res}}$ as the previously lowest scattering state now shows an exponentially decaying wave function. The interacting scattering wave functions are pulled into the square-well potential.

character of the interaction potential (i.e., $V_0 < 0$, throughout the whole analysis). This scenario corresponds to $V_0 \gtrsim V_{\text{res}}$ where the potential hosts a single deeply-bound state and the scattering states are slightly shifted upwards in energy compared to their non-interacting counterparts.

If V_0 is only slightly lowered the point $V_0 = V_{\text{res}}$ is reached where the lowest scattering state has the same energy as the non-interacting ground state[3], see Fig. 3.2(b). A numerical analysis of the scattering wave functions suggests that their long-distance part matches exactly their corresponding non-interacting counterparts, i.e., that the phase shifts vanish ($\delta(k) = 0$ also for $k > 0$ in the limit of $R_{\text{box}} \to \infty$). Thus for $V_0 = V_{\text{res}}$ the effective interactions between the two particles vanish as the asymptotic scattering wave functions have no signature of the potential and pairwise match the non-interacting states. The system effectively behaves like two free particles, apart from the existence of the deeply-bound state.

By lowering V_0 slightly more a new bound state is created. For $V_0 \lesssim V_{\text{res}}$ in (c) the previously lowest scattering wave function is pulled into the potential well and its long-distance behavior decays exponentially, signaling bound-state formation. All energy levels of the interacting states (except the deeply-bound state) are now slightly below

[3]Due to the confinement in the box the non-interacting s-wave ground-state energy is given by $E_n = \hbar^2 j_{0,n}^2/(2\mu R_{\text{box}}^2)$ with $j_{0,n}$ the n-th zero of J_0 the Bessel function of first kind.

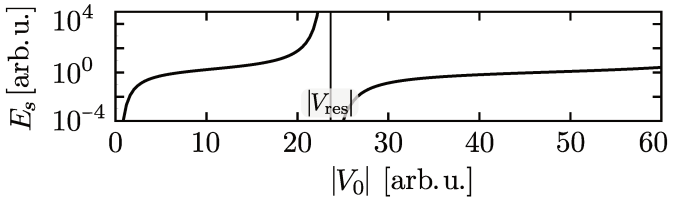

Figure 3.3.: Energy scale E_s extracted from the lowest scattering wave function. Whenever a bound state is introduced into the scattering potential E_s diverges and jumps to zero. The zero at $V_0 = 0$ corresponds to the emergence of the first bound state.

their non-interacting counterparts and the phase shifts δ are negative (or $\delta \lesssim \pi$ when restricted to the interval $\delta \in [0, \pi)$).

This simple analysis already shows a remarkable feature of two-dimensional scattering physics. Whenever a two-particle scattering potential is modified in a way that the two particles obtain (lose) the ability to form a bound state, the system becomes effectively non-interacting[4], and the phase shifts jump from 0 to π (or vise versa).

To substantiate these statements found from this simple analysis of scattering wave functions we extract the phase shifts of the low-energy scattering states by a numerical fit of their radial long-distance behavior with the two-dimensional scattering functions

$$R_n(r) = \alpha_m(k_n) J_m(k_n r) + \beta_m(k_n) Y_m(k_n r) \ , \tag{3.5}$$

where J_m and Y_m are the Bessel functions of first and second kind, and k_n labels the scattering momentum of the n-th state. Note $m = 0$ as we consider s-wave scattering. Using [30, 82]

$$\delta_m(k_n) = -\arctan\left(\beta_m(k_n)/\alpha_m(k_n)\right) \ , \tag{3.6}$$

we obtain the two-dimensional phase shift $\delta \equiv \delta_0(k)$, which is linked to the energy scale E_s by

$$\cot(\delta) \overset{E\to 0}{=} 1/\pi \ln(E/E_\mathrm{s}) \ , \tag{3.7}$$

where $E = \hbar^2 k^2/\mu$. E_s is connected to the two-dimensional scattering length a_2d by

$$a_\mathrm{2d} = \sqrt{\frac{\hbar^2}{2E_\mathrm{s}\mu}} \ . \tag{3.8}$$

In Fig. 3.3, we show E_s obtained from an analysis of the lowest two-body scattering wave function. When crossing the resonance at $|V_\mathrm{res}|$ from left to right (introducing a new bound state to the interaction potential) E_s diverges and jumps to zero. The

[4]For the transition of repulsive to attractive potentials (when V_0 changes its sign), this is a direct consequence of the fact that in two-dimensions all attractive potentials host at least one bound state [81].

divergence of the two-dimensional scattering length and simultaneous vanishing of interactions whenever a bound state is created in an interaction potential is a peculiar feature of two-dimensional scattering [83]. This pinpoints the loss of meaning of the resonance width as defined in three-dimensional ultracold atomic systems[5].

The analysis of s-wave scattering states[6] in this section shows how the interactions between particles can be tuned by will analogously to a Feshbach resonance in ultracold atoms, if one is able to introduce/remove bound states from a two-dimensional scattering potential. This has important consequences for the optical response of the two-dimensional Fermi-polaron problem (also discussed in [84]) which will be laid out in the following (for a review of polarons in three dimensions see [24]).

3.1.1. Fermi-Polaron Problem with Tunable Square-Well Interactions in Two Dimensions

Impurity problems show universal features across physics. The emerging polaron allows to study a many-body system when brought away from its non-interacting state, making it essential for the understanding of the phase diagrams of strongly interacting quantum systems. In the upcoming subsection we investigate a static impurity (with infinite mass) in a Fermi sea. The interactions between fermions and the impurity are modeled by the square-well potential introduced in the previous section. We use a direct functional determinant approach [24] (see Appendix B) to calculate the Fermi polaron spectrum (cf. Fig. 3.4) while lowering V_0 (i.e., increasing $|V_0|$) around V_{res} where the second bound state emerges in the impurity-bath interaction potential. An analogous generic behavior of attractive and repulsive polaron branches is found whenever a bound state is introduced into (or removed from) the interaction potential.

Importantly the universality of s-wave scattering allows to replace any physical interaction potential by a model potential that reproduces the same phase shifts (and in consequence E_{s} parameters) to describe the scattering physics. Hence despite the relative simplistic choice of a square-well interaction potential the resulting polaron spectrum still resembles the physics for more realistic choices of interaction potentials for given values of E_{s}.

At the resonance marked with V_{res} in Fig. 3.4 the second bound state appears in the interaction potential and a new repulsive polaron branch emerges in the spectrum with zero spectral weight. The repulsive branch on the left of $|V_{\mathrm{res}}|$ emerged in the same way at the point where the first bound state is introduced in the system (i.e., at $V_0 = 0$, see Fig. 3.3 where E_{s} vanishes at $V_0 = 0$). At $V_0 = V_{\mathrm{res}}$ this repulsive branch maximizes its spectral weight, crosses the energy of the two-body scattering threshold and is then converted into an attractive polaron. When moving to the right it begins

[5] Here the resonance width (as discussed in Section 2.2.1) was defined as the distance of the zero crossing of the scattering length and the resonance position, which coincide in two dimensions.

[6] A similar analysis can be done for higher angular momentum states.

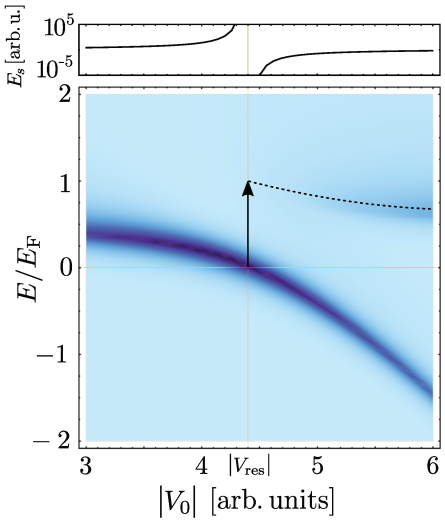

Figure 3.4.: Polaron spectrum in dependence of the potential depth V_0 and energy with respect to the impurity-fermion scattering threshold in units of the Fermi energy E_F. V_0 is chosen around the resonance at V_{res} where the second bound state is introduced to the square-well potential. In the top panel the corresponding E_s parameter is shown. The colors correspond to the absorption strength in arbitrary units, where darker colors indicate larger absorption. The dashed line is a guide to the eye of the emerging repulsive polaron branch at E_F the resonance. At this point the repulsive branch crosses the energy of the two particle scattering threshold at zero with maximal spectral weight and is converted into an attractive polaron branch. When moving to the right the attractive branch looses spectral weight while the repulsive branch gains spectral weight (until it would reach the point where the third bound state is created, where it has maximal spectral weight, is converted into an attractive polaron, yet another repulsive polaron is created, and the whole process repeats itself). Note that the attractive polaron branch caused by the deeply-bound state is not shown in the figure. This branch also looses spectral weight while increasing $|V_0|$.

to lose spectral weight. Analogously the energetically lower attractive polaron caused by the deeply-bound state (which is not shown in Fig. 3.4) looses spectral weight. The combined loss of the spectral weight of the attractive branches is transferred to the repulsive branch, which emerges at the Fermi energy $E = \epsilon_F$. When increasing $|V_0|$ until it reaches the point where the third bound state would be introduced to the interaction potential (not shown in the figure). At this point (analogously to $V_0 = V_{res}$) the repulsive branch crosses the two-body scattering threshold, maximizes its spectral weight and is converted into an attractive polaron, while a new repulsive polaron branch emerges with zero spectral weight. This process repeats itself whenever a new bound state is generated in the two-body interaction potential and is linked to the reallocation of scattering states when the lowest scattering state becomes a new bound state.

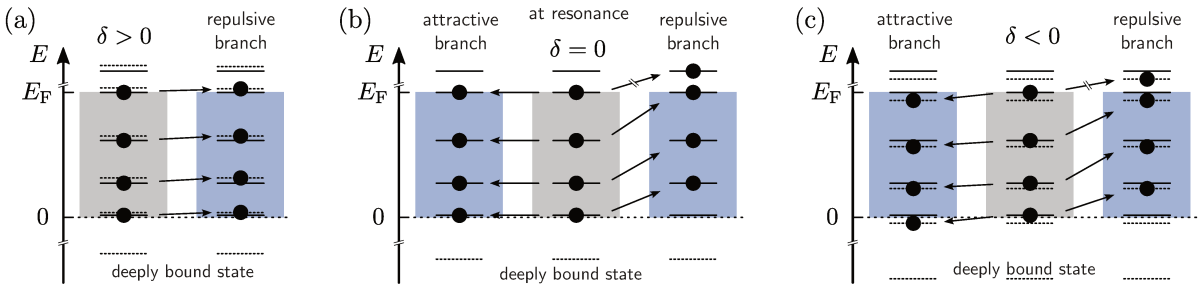

Figure 3.5.: Illustration of energy levels and transitions of states which determine the strength of the different polaron branches. The non-interacting states are marked in gray (free Fermi sea). The arrows indicate the refilling of single particle orbitals during the formation of the respective polarons. Note that the deeply-bound state also causes an attractive polaron branch that is present in (a) $V_0 \gtrsim V_{\mathrm{res}}$, (b) $V_0 = V_{\mathrm{res}}$ and (c) $V_0 \lesssim V_{\mathrm{res}}$ which is again neglected due to illustrative reasons. In (a) the interacting energy levels (dashed lines) are slightly shifted upwards with respect to the non-interacting ones (solid lines). In (b) the interacting energy levels match their non-interacting counterparts (solid lines). Note that in contrast to Fig. 3.4 the energy of the lowest non-interacting state (i.e., scattering threshold) is not at 0 this is only true in an infinite system. Inside the quantization box the non-interacting s-wave energy levels are given by $E_n = \hbar^2 j_{0,n}^2/(2\mu R_{\mathrm{box}}^2)$ with $j_{0,n}$ the n-th zero of J_0 the Bessel function of first kind. Note that $\mu = m_{\mathrm{Fermion}}$ as we consider an immobile impurity. For the case of an infinitely heavy impurity in a three-dimensional Fermi sea see [24].

This scheme can be easily understood from a picture of many-body states created from filling up single-particle orbitals illustrated in Fig. 3.5. The horizontal dashed lines correspond to the interacting single-particle energy levels which are shifted either up or downwards with respect to their non-interacting counterparts (solid black lines). In this simple picture the overlap of interacting and non-interacting single-particle scattering states is large if their energies are similar. The occupation of the respective single-particle state in a many-body state is represented by a black dot.

In the following the interacting single particle states are labeled by $|\nu\rangle$ and the corresponding non-interacting single particle states by $|n\rangle$, respectively. In Fig. 3.5(a) the interacting energy levels (dashed lines) are slightly shifted upwards with respect to the non-interacting ones (solid lines). The polaron energy is given by the sum of these energy differences

$$E_{\mathrm{pol}} = \sum_{n \leq n_{\mathrm{F}}} \Delta E_n \ , \tag{3.9}$$

with $|n_{\mathrm{F}}\rangle$ the free single-particle mode at the Fermi level and the energy difference $\Delta E = E_\nu - E_n$ of the respective interacting and non-interacting single-particle orbitals E_ν and E_n. Hence the corresponding repulsive polaron is shifted slightly upwards in

energy with respect to the impurity-bath scattering threshold (c.f. Fig. 3.5a). The respective many-body states (Slater determinants of the corresponding interacting and non-interacting single-particle orbitals, connected by arrows in a) have a rather good overlap causing the spectral weight of the repulsive polaron to be substantial.

At the resonance $V_0 = V_{\mathrm{res}}$, the interacting and non-interacting energy levels match (in the limit $R_{\mathrm{box}} \to \infty$) shown on the left side of (b) causing the polaron energy to match the impurity-fermion scattering threshold (see Fig. 3.4, the polaron energy changing its sign at the resonance). Also the asymptotic interacting orbitals $|\nu\rangle$ exactly match their non-interacting counterparts $|n\rangle$ causing a maximized spectral weight. At this point a different rearrangement of single-particle orbitals becomes possible, illustrated on the right panel of (b). This leads to the emergence of a new repulsive polaron branch with zero spectral weight as its Slater determinant contains a state that causes the overlap with the non-interacting many-body state to vanish. The onset of the newly emerging repulsive branch is then given by summing the offsets of neighboring energy levels, i.e., $\nu = n + 1$,

$$\sum_{n \leq n_{\mathrm{F}}} \Delta E_n = \sum_{n \leq n_{\mathrm{F}}} E_{n+1} - E_n \overset{\mathrm{n}\to\infty}{\approx} E_{\mathrm{F}} \ , \tag{3.10}$$

which sum up trivially to the Fermi energy (in the limit $R_{\mathrm{box}} \to \infty$).

The above investigation of a toy model clarified the ingredients needed for the realization of tunable interactions in two dimensions and how they could be observed via clear optical signatures in a many-body setting. We now turn to the microscopic analysis of Feshbach resonances in atomically thin semiconductors, where exciton-electron Feshbach resonances will enable to study the mobile[7] Fermi-polaron problem with tunable interaction.

3.2. Feshbach Resonances in Two-Dimensional Materials from First Principles

The following section summarizes [P5] and presents one of the main results of this thesis. We show how two-dimensional electron-exciton Feshbach resonances result from first-principles by analyzing the underlying microscopic three-body problem. To this end, we solve the problem of two electrons and one hole interacting with each other in a bilayer TMD structure. In contrast to the two-body toy model studied above the three particles are now interacting with more realistic interaction potentials. We find that the excited states of the low-energy spectrum always contain a bound electron-hole pair, an exciton, that scatters with the third charge carrier. In this context it is the exciton-electron

[7] In this context the impurity is given by an exciton.

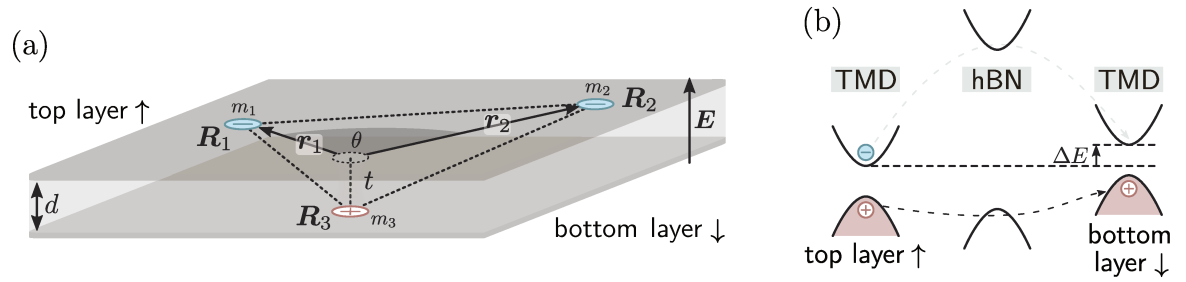

Figure 3.6.: (a) Sketch of the bilayer system. The two TMD layers are separated by a distance d, which will be later set to a value that reflects the thickness of a hBN monolayer. The blue (red) circles represent the electrons (holes). The system is subject to an external perpendicular electric field $\boldsymbol{E} = E_z \hat{\mathbf{e}}_z$. (b) Illustration of the band structure offset in the TMD-hBN-TMD heterostructure. The hBN conduction-band offset suppresses the tunneling amplitude of the electron. The external electric field allows to shift the TMD band structures with respect to each other.

scattering properties that can be manipulated by allowing the three particles to form a three-body bound state, a trion (that can be effectively viewed as an exciton-electron bound state and is sometimes also called 'charged exciton' in literature).

An illustration of the system is shown in Fig. 3.6(a). The electrons are fixed to one layer while the hole can tunnel between the layers. In experiments this condition can be realized by placing a layer of hexagonal boron nitride (hBN) between the TMD layers. The conduction band of the hBN layer represents an energy barrier for the electrons which they need to overcome when tunneling between the layers (see Fig. 3.6b). Thus, suppressing electron tunneling compared to hole tunneling, justifying the approximation of fixing the electrons to one layer of the bilayer structure while the holes are able to tunnel between them.

The Hamiltonian we investigate reads

$$\hat{H} = \sum_{i=1}^{3} \left[\frac{-\hbar^2}{2m_i} \Delta_{\boldsymbol{R}_i} - \frac{q_i \Delta E}{2} (\mathbb{1} - \tau_z^i) + t_i \tau_x^i \right] + \sum_{a,b} \sum_{i<j}^{3} V_{ab}(|\hat{\boldsymbol{R}}_i - \hat{\boldsymbol{R}}_j|) \ , \tag{3.11}$$

with the mass m_i, the spacial coordinate vector $\boldsymbol{R}_i$ of the i-th particle, the band detuning of top and bottom layer ΔE (cf. [85] for the monolayer scenario) and the Pauli matrices

$$\tau_x = \begin{pmatrix} 0 & 1 \\ 1 & 0 \end{pmatrix} \quad , \quad \tau_z = \begin{pmatrix} 1 & 0 \\ 0 & -1 \end{pmatrix} \ , \tag{3.12}$$

which act on the layer subspace (pseudospin) of each particle.

First, we will derive the kinetic part of the Hamiltonian in relative coordinates, keeping the interaction potential V_{ab} between charges in layer a and b unspecified. We however assume that V_{ab} only depends on the layer projected charge separation and the layer

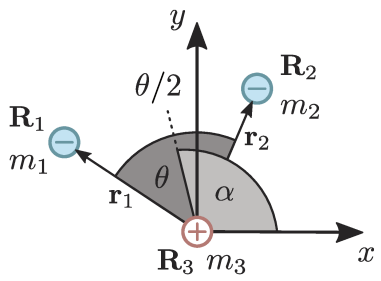

Figure 3.7.: Illustration of the relative three-body coordinate system used to parametrize the Hamilonian when viewed orthogonally on the plane of the heterostructure. The electron-hole distances are given by r_1 and r_2. The in-plane separations span the angle θ. The overall orientation of the three particles is parametrized by the angle α.

configuration of the involved charges, i.e., $V_{ab}(\boldsymbol{r}) = V_{ab}(|\boldsymbol{r}|)$, where $\boldsymbol{r}$ is a two-dimensional vector. In doing so, we separate the center-of-mass motion via the transformation

$$\boldsymbol{r}_1 = \boldsymbol{R}_1 - \boldsymbol{R}_3 \quad , \quad \boldsymbol{r}_2 = \boldsymbol{R}_2 - \boldsymbol{R}_3 \quad , \quad \boldsymbol{r}_{\mathrm{CM}} = \frac{1}{M}(m_1\boldsymbol{R}_1 + m_2\boldsymbol{R}_2 + m_3\boldsymbol{R}_3) \ , \tag{3.13}$$

with the total mass M, leading to the Hamiltonian

$$\begin{aligned}\hat{H} = \sum_{i=1}^{2} \frac{-\hbar^2}{2\mu_i}\Delta_{\boldsymbol{r}_i} - \frac{\hbar^2}{m_3}\nabla_{\boldsymbol{r}_1}\cdot\nabla_{\boldsymbol{r}_2} - \frac{\hbar^2}{2M}\Delta_{r_{\mathrm{com}}} - \sum_{i=1}^{3}\frac{q_i\Delta E}{2}(\mathbb{1}-\tau_z^i) + t_i\tau_x^i \\ + \sum_{a,b}\sum_{i=1}^{2} V_{ab}(|\hat{\boldsymbol{r}}_i|) + V_{ab}(|\hat{\boldsymbol{r}}_1 - \hat{\boldsymbol{r}}_2|) \ ,\end{aligned} \tag{3.14}$$

where $\mu_i = m_i m_3/(m_i + m_3)$ is the reduced mass. Using the electron-hole distances r_1, r_2 and the in-plane angle spanned between the electrons θ and α the orientation of the three particles (see Fig. 3.7) to parametrize the relative distances

$$\begin{aligned}\boldsymbol{r}_1 &= r_1(\cos(\alpha+\theta/2)\mathbf{e}_x + \sin(\alpha+\theta/2)\mathbf{e}_y) \ , \\ \boldsymbol{r}_2 &= r_1(\cos(\alpha-\theta/2)\mathbf{e}_x + \sin(\alpha-\theta/2)\mathbf{e}_y) \ ,\end{aligned} \tag{3.15}$$

one arrives at the Hamiltonian in the relative coordinate system with the hole in its center

$$\begin{aligned}\hat{H}_{\mathrm{rel}}^{\mathrm{kin}} = &\sum_{i=1}^{2}\frac{-\hbar^2}{2\mu_i}\left(\partial_{r_i}^2 + \frac{\partial_{r_i}}{r_i} + \frac{\partial_\theta^2}{r_i^2} + \frac{\partial_\alpha^2}{4r_i^2} - \frac{\partial_\theta\partial_\alpha}{r_i^2}\right) \\ &- \frac{\hbar^2}{m_3}\left(\cos\theta\,\partial_{r_1}\partial_{r_2} - \frac{\cos\theta\,\partial_\theta^2}{r_1 r_2} - \left(\frac{\partial_{r_1}}{r_2} + \frac{\partial_{r_2}}{r_1}\right)\sin\theta\,\partial_\theta\right. \\ &\left. + \frac{\cos\theta\,\partial_\alpha^2}{4r_1 r_2} + \left(\frac{\partial_{r_2}}{r_1} - \frac{\partial_{r_1}}{r_2}\right)\frac{\sin\theta\,\partial_\alpha}{2}\right) \ .\end{aligned} \tag{3.16}$$

The ansatz for the relative wave functions

$$\Psi(r_1, r_2, \theta, \alpha) = \psi(r_1, r_2, \theta)\mathrm{e}^{\mathrm{i}m\alpha} \tag{3.17}$$

includes the conservation of angular momentum m. In the following we focus on the zero angular momentum case $m = 0$. The kinetic Hamiltonian acting on the $m = 0$ subspace is given by

$$\begin{aligned}\hat{H}_{\mathrm{rel}}^{\mathrm{kin}} =& \sum_{i=1}^{2} \frac{-\hbar^2}{2\mu_i}\left(\partial_{r_i}^2 + \frac{\partial_{r_i}}{r_i} + \frac{\partial_\theta^2}{r_i^2}\right) \\ &- \frac{\hbar^2}{m_3}\left(\cos\theta\,\partial_{r_1}\partial_{r_2} - \frac{\cos\theta\,\partial_\theta^2}{r_1 r_2} - \left(\frac{\partial_{r_1}}{r_2} + \frac{\partial_{r_2}}{r_1}\right)\sin\theta\,\partial_\theta\right) .\end{aligned} \tag{3.18}$$

Including the interaction potential as well as the hopping between layers, the total Hamiltonian can be written as

$$\begin{aligned}\hat{H} = \hat{H}_{\mathrm{rel}}^{\mathrm{kin}} &- \sum_{i=1}^{3} \frac{q_i \Delta E}{2}(\mathbb{1} - \tau_z^i) + t_i \tau_x^i \\ &+ \sum_{a,b}\sum_{i=1}^{2} V_{ab}(r_i) + V_{ab}\left(\sqrt{r_1^2 + r_2^2 - 2r_1 r_2 \cos\theta}\right) .\end{aligned} \tag{3.19}$$

Now we turn to the interaction potential between the two charges that is obtained by solving Poisson's equation

$$\Delta\Phi(\boldsymbol{r}) = -\frac{1}{\varepsilon_0}\rho \tag{3.20}$$

for two identical layers separated by a distance of $d = 1.03\,\mathrm{nm}$ that accounts for the separation of the TMD centers by a monolayer of hBN[8] of thickness 0.33 nm [86] and the thickness of $MoSe_2$ (0.7 nm [87]). In Eq. (3.20) $\Phi(\boldsymbol{r})$ is the electrostatic potential, ε_0 the vacuum permittivity and the total charge density is given by

$$\rho = \rho_{\mathrm{ext}} + \rho_{\mathrm{ind}_1} + \rho_{\mathrm{ind}_2} , \tag{3.21}$$

where ρ_{ind_i} is the induced charge density in layer i,

$$\rho_{\mathrm{ind}_i} = -\nabla \boldsymbol{P}_{2\mathrm{d}_i} , \tag{3.22}$$

with the two-dimensional polarizarion vector of layer i

$$\boldsymbol{P}_{2\mathrm{d}_i} = -\varepsilon_0 \alpha_{2\mathrm{d}} \nabla_{\boldsymbol{x}} \Phi_{3\mathrm{d}}(\boldsymbol{x})\delta(z) , \tag{3.23}$$

[8]Note that the layer of hBN is treated here as a layer of vacuum with a thickness according to a monolayer of hBN. This causes our results to underestimate binding energies, however the general mechanism described here remains valid.

with the TMD layer's two-dimensional polarizability $\alpha_{2\mathrm{D}}$ and $\boldsymbol{x} = (\boldsymbol{r}, z)$, where $\boldsymbol{r}$ is the two-dimensional in-plane relative coordinate vector.

The layer dependent interaction potential for charges Q_i and Q_j in momentum space is then obtained as

$$\Phi_{\mathrm{intra}}(q) = \frac{Q_i Q_j \left((1 + r_0 q)\mathrm{e}^{2dq} - r_0 q\right)}{2\varepsilon_0 \left((1 + r_0 q)^2 q \mathrm{e}^{2dq} - r_0^2 q^3\right)} \tag{3.24}$$

for two charges in the same layer, and

$$\Phi_{\mathrm{inter}}(q) = \frac{Q_i Q_j \mathrm{e}^{dq}}{2\varepsilon_0 \left((1 + r_0 q)^2 q \mathrm{e}^{2dq} - r_0^2 q^3\right)} \tag{3.25}$$

for charges in different layers (for details see the supplemental material of [P5]). The electrostatic screening of a monolayer is described by the screening length $r_0 = \alpha_{2\mathrm{D}}/2$. A numerical Fourier transformation links the momentum- and real-space potentials

$$\begin{aligned} \Phi_{\mathrm{intra}}(q) &\xrightarrow{\mathcal{F}} V_{ab}(r) \quad , \quad \text{with } a = b \ , \\ \Phi_{\mathrm{inter}}(q) &\xrightarrow{\mathcal{F}} V_{ab}(r) \quad , \quad \text{with } a \neq b \ , \end{aligned} \tag{3.26}$$

which are used in the following to describe the interactions between charges in a bilayer TMD system. Note that in the limit $d \to 0$ Eq. (3.24) converges to the Rytova-Keldysh potential (see Eq. (2.1)) [63, 64] which is used in Literature to model the interaction potential between charges in TMD monolayers or to approximate the potential in bilayer systems with vanishing layer separation, $d \to 0$.

3.2.1. Feshbach Resonances from Solving the Three-Body Problem

To obtain a better understanding of two-dimensional exciton-electron scattering we now turn to the discussion of the results of the numerical diagonalization of the Schrödinger equation

$$\hat{H}\,\psi(r_1, r_2, \theta) = E\,\psi(r_1, r_2, \theta) \ , \tag{3.27}$$

with the three-body Hamiltonian $\hat{H}$ in the zero angular momentum sector given in Eq. (3.19). To obtain the results we use a discrete variable representation (DVR) [71, 88] (also see Appendix C) and a standard Arnoldi diagonalization method. We focus on a bilayer system made from two $MoSe_2$ monolayers and use material parameters obtained from DFT [57]. An extension to heterostructures made out of different TMDs is straight forward.

We assume the absence of electron hopping, which makes the layer index of the electrons a conserved quantity, causing the Hilbert space to decouple into three invariant subspaces (both electrons in either the top or bottom layer and one electron in either layer respectively). Further, the Hamiltonian (3.19) is invariant with respect

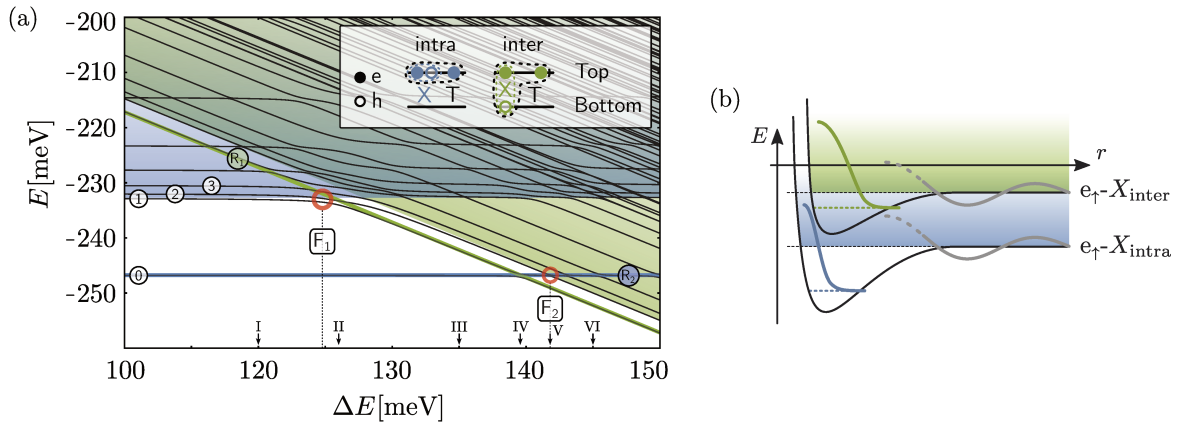

Figure 3.8.: (a) Spectrum of spatially symmetric three-body states with respect to electron exchange, as function of the band detuning ΔE and a hole tunneling amplitude $t = 2\,\mathrm{meV}$ [33]. Bold colored lines mark trion energies for $t = 0$, whereas black lines show the eigenenergies (including trion and exciton-electron scattering states) in presence of hole tunneling. Shaded areas are guides to the eye representing the different scattering continua. Blue color indicates intralayer and green color interlayer configurations as shown in the pictogram. Feshbach resonances appear at the positions labeled F_1 and F_2. Symbols I-VI mark ΔE values for which the states labeled by 0-3, R_1 and R_2 are visualized in Fig. 3.9. (b) Sketch of the Feshbach-resonance channel description. A resonance occurs when an exciton scatters with a top layer electron and can resonantly couple to a trion state (bold colored line). The energy offset between both configurations (channels) can be tuned via the band offset ΔE.

to the exchange of electrons, leading to wave functions ψ that are either symmetric $\psi(r_1, r_2, \theta) = \psi(r_2, r_1, -\theta)$ or antisymmetric $\psi(r_1, r_2, \theta) = -\psi(r_2, r_1, -\theta)$ under electron exchange. Each of these sets of wave functions again span an invariant subspace of the Hilbert space. In the following we solely focus on the symmetric subspace containing states with electrons (of unequal spin) in the top layer. The two possible particle configurations are depicted in the inset of Fig. 3.8(a), which shows how the symmetric low-energy spectrum depends on the detuning of the band structures ΔE for a hole tunneling amplitude of $t = 2$ meV [33]. The tunneling of holes couples intralayer (blue) and interlayer (green) states. For a better visual identification of the energies corresponding to hybridized states (thin black lines) energies of trion states in the $t = 0$ scenario are plotted in respective bold colored lines, the intralayer trion in blue and the interlayer trion in green. In the following we address these states as bare trions. The lower edge of the shaded areas correspond to the respective exciton-electron scattering thresholds (energies of the lowest scattering states) in the $t = 0$ scenario. Due to the finite size of the system the scattering states form a set of discrete states rather than a continua that would be obtained in the infinite box limit $R_{\mathrm{box}} \to \infty$.

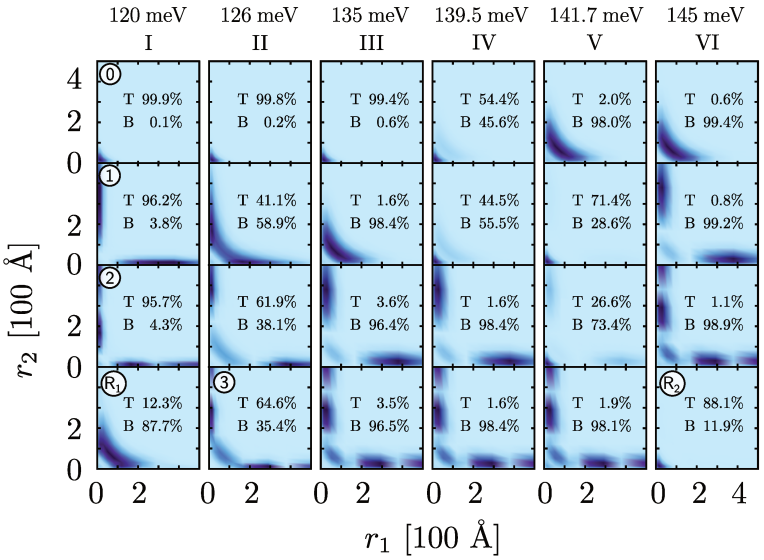

Figure 3.9.: Angle averaged probability densities of electrons $n(r_1, r_2) \propto \int \mathrm{d}\theta \, |\psi(r_1, r_2, \theta)|^2$ for the lowest states at the ΔE values (shown above the figure) marked with labels I-VI in Fig. 3.8. Dark colors indicate a large probability density. The hybridization of intralayer (hole in top layer, T) and interlayer (hole in bottom layer, B) configuration is indicated for each state.

Particularly interesting points are those where the bare trions cross the exciton-hole scattering thresholds. The respective anticrossings of hybridized eigenstates signals strong couping of open and closed channels at these points, marked with red circles in Fig. 3.8(a).

This motivates to think of two-dimensional exciton-hole scattering in TMDs in the usual Feshbach resonance picture known from ultracold atoms (see Fig. 3.8b). The exciton-hole scattering threshold is equivalent to the open channel whereas the bare trions (bold colored lines) take the role of closed-channel molecules that are coupled to continuum states via exciton layer hybridization.

One bound state always remains separate from the scattering threshold for all values of ΔE. This indicates that the effective exciton-electron interaction is always attractive, as in two-dimensional systems any attractive interaction causes the presence of a bound state. Note that the attractive character of exciton-electron interactions is not trivial, despite the two-particle electron-hole interactions being attractive, as the effective interactions between an exciton and an electron can turn out to be repulsive, not allowing for the formation of a bound trion state.

In Fig. 3.9, the θ-averaged probability densities $n(r_1, r_2) \propto \int \mathrm{d}\theta \, |\psi(r_1, r_2, \theta)|^2$ of the lowest states (thin black lines labeled with 0-3, R_1 and R_2 in Fig. 3.8a) are shown for different band detunings ΔE labeled with I-VI in Fig. 3.8(a). For each state we give the probability of finding the hole in the top (T) or bottom (B) layer.

For $\Delta E = 120\,\text{meV}$ (I) the ground-state probability density is shown in the top of the first column in Fig. 3.9. The probability of finding both electrons close to the hole is high. This state is the deeply-bound intralayer trion. The two states below are the first and second exciton-electron scattering states. Here the probability density is high along the r_1 and r_2 axis, i.e., when one electron is close (bound) to the hole, the other is far away. Thus, these states can be effectively viewed as exciton-electron scattering states. Their wave functions exhibiting the typical lobe structure of scattering states confined in a box (see second and third line of column I in Fig. 3.9).

The bottom panel of the first column shows the resonant interlayer trion (marked with R_1 in Fig. 3.8) immersed in the intralayer scattering 'continuum'. The spatial extent of this interlayer trion is much larger compared to the intralayer trion due to the more pronounced effect of electron repulsion in the interlayer configuration.

While crossing the first resonance F_1 at $\Delta E \approx 125$ meV, we observe a continuous transformation of the first excited state from being the first intralayer scattering state into the interlayer trion (see second line in Fig. 3.9 across columns I-III). In the same way the second excited state changes from being the second intralayer scattering state (showing two lobes) into being the first interlayer scattering state (showing only one lobe). Analogously, higher excited states change their number of radial lobes by one when crossing the resonant state. The ground-state wave function remains nearly unchanged (bottom line) for values of $\Delta E < 139.5$ meV.

A further increase of ΔE leads to an anticrossing of the bound states at IV. At this point the bound state wave functions show signatures of the nearly maximally hybridized inra and interlayer trions.

While crossing the second resonance F_2 at V (here $\Delta E \approx 141.7\,\text{meV}$) the excited states gain an additional lobe. Here the hybridized intralayer trion crosses into the interlayer scattering continuum turning into a resonant state (labeled R_2 in Figs. 3.8(a) and 3.9).

This analysis further substantiates the picture of tightly bound excitons scattering with an additional electron. However, it also shows that the layer hybridization[9] of excitons can play a key role in the emergence of exciton-electron Feshbach resonances.

To further establish the notion of Feshbach resonances in two-dimensional semiconductors, we investigate the scattering properties of the lowest scattering state (open channel) when tuning ΔE across the resonances by determining the exciton-electron phase shifts characterizing the extent of the wave-function modification due to exciton-electron interactions. To this end, we again fit the long-distance part of the lowest scattering state to the asymptotic scattering wave function, analogously to the analysis of scattering wave functions in the previous part, see Eq. (3.5). We then extract E_s as defined in Eq. (3.7) as parameter that characterizes exciton-electron interactions in two dimensions.

In Fig. 3.10, we show E_s obtained from an analysis of the lowest exciton-electron

[9]Note that the layer hybridization found in Fig. 3.9 implies a modification of the electric dipole of the excitons and trions. This might give rise to interesting, tunable many-body physics of long-lived excitons and trions at finite density.

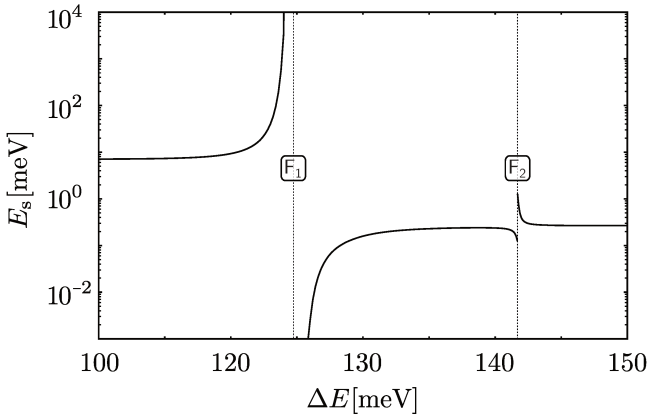

Figure 3.10.: Band detuning dependence of the exciton-electron scattering parameter E_s. The broad and narrow Feshbach resonances are labeled as F_1 and F_2, respectively (as shown in Fig. 3.8a).

scattering wave functions across the resonances F_1 and F_2. On the left, far away from the resonance F_1, E_s is approximately constant and takes a value linked to the background scattering length $a_\mathrm{2d} = \sqrt{\hbar^2/2E_\mathrm{s}\mu}$ of excitons and electrons in the intralayer configuration. When approaching F_1 the parameter E_s increases, diverges and jumps to zero. At this point a new bound state, the interlayer trion, appears and the system becomes effectively non-interacting. In the regime shortly after the appearance of the newly emerging Feshbach bound trion, E_s follows its binding energy. After crossing the narrow resonance F_2 the parameter E_s converges to a value linked to the background scattering length in the interlayer configuration.

The equivalence of vanishing and diverging scattering lengths at F_1 and F_2 is inherent for two-dimensional systems [83] as we have seen in the discussion of the toy model in Section 3.1. In contrast to three-dimensional Feshbach resonances in ultracold gases, the concept of the resonance width, defined as the separation of the zero crossing of the scattering length and the resonance position, is not practicable in TMDs. Namely, the zero of $a_\mathrm{2d} = \sqrt{\hbar^2/2\,E_\mathrm{s}(\Delta E)}$ coincides with the two-dimensional Feshbach resonance position.

The hybridization of intra and interlayer scattering thresholds in the vicinity of F_1 causes a large overlap of open and closed channel. This results in a relatively broad resonance at the position F_1. At the more narrow resonance F_2 the parameter E_s quickly vanishes and returns from infinity as the intralayer Feshbach trion crosses the interlayer scattering threshold.

Further the character of the resonances F_1 and F_2 differ with respect to lifetime and oscillator strength of excitons in the open channel. The resonance F_1 allows to manipulate the scattering of electrons and short-lived intralayer excitons with a large oscillator strength, while the scattering properties of long-lived intralayer excitons (small oscillator strength) can be tuned via F_2. This allows to either use optically injected intralayer

excitons (at F_1) to probe correlations of electronic systems, or to bring tunable interactions (at F_2) to the many-body system comprising stable interlayer excitons and electrons, paving the way to the realization of long-lived exciton-electron mixtures at strong-coupling, and thus enables a new approach to explore the Fermi-polaron problem and the phase diagram of Bose-Fermi mixtures in regimes that have so far been out of reach in ultracold atomic systems due to their chemical instability [39].

Note, we have focused on one specific configuration that is directly relevant for ongoing experiments. Allowing for different van der Waals heterostructures and electron-hole layer configurations (including modified tunneling strength, charge, valley and spin degrees of freedom) will give rise to an even richer set of Feshbach resonances to be explored.

In this section we have shown how electrically tunable two-dimensional Feshbach resonances emerge from the states within a TMD heterostructure. We found two distinct resonances that allow to control scattering processes of both short and long-lived excitons with electrons.

3.3. An Application - Tunable Exciton Band Structures in Charged Ordered States

We now turn to an effective model to investigate how Feshbach resonances can be used to introduce tunable band structures for excitons interacting with lattices of charges. In two-dimensional semiconductors such lattices arise naturally in form of charge ordered states such as Wigner crystals or correlated Mott insulators [41, 46, 47]. Their interactions with excitons give rise to Bragg scattering, leading to the appearance of an Umklapp peak in the optical response of the material [41, 46].

However, in these systems the trion binding energy E_T is typically fixed and large compared to the energy scale of many-body excitations. This prohibits the resonant formation of molecular bands arising from excitons 'hopping' between charges that can be viewed as lattice sites in this tight-binding regime. As a consequence the exploration of the emergence of Hubbard-type physics governed by hopping of excitons in a tight-binding-model-type fashion is not possible. This can be overcome by using Feshbach resonances as discussed above to tune exciton-lattice interactions and thereby manipulating the trion binding energy.

We consider a lattice of electrons and describe the electron density effectively within a mean field model

$$\begin{aligned} H &= \sum_{\boldsymbol{\mathcal{G}}} \frac{(\boldsymbol{k}+\boldsymbol{\mathcal{G}})^2}{2m} + H_{\text{int}} \ , \\ H_{\text{int}} &\approx \boldsymbol{r} \int \mathrm{d}^2\boldsymbol{r}' n_X(\boldsymbol{r}) V_{\text{eff}}(|\boldsymbol{r}-\boldsymbol{r}'|) \langle n_{\text{e}}(\boldsymbol{r}')\rangle \ , \end{aligned} \tag{3.28}$$

where $\boldsymbol{k}$ is the momentum in the first Brillouin zone, the sum runs over the reciprocal lattice ($\boldsymbol{\mathcal{G}} = i\boldsymbol{G}_1 + j\boldsymbol{G}_2$ with $i, j \in \mathbb{Z}$) and $\langle n_\mathrm{e}(\boldsymbol{r}')\rangle$ is the average electron density. We consider the case of perfectly localized electrons, i.e., $\langle n_\mathrm{e}(\boldsymbol{r})\rangle = \sum_{\boldsymbol{R}} \delta^{(2)}(\boldsymbol{r} - \boldsymbol{R})$, ordered in a triangular lattice with lattice vectors

$$\mathbf{R}_1 = \frac{d}{2}\begin{pmatrix} 1 \\ \sqrt{3} \end{pmatrix} \quad , \qquad \mathbf{R}_2 = \frac{d}{2}\begin{pmatrix} -1 \\ \sqrt{3} \end{pmatrix} \ , \tag{3.29}$$

lattice constant d and reciprocal lattice vectors

$$\mathbf{G}_1 = \frac{2\pi}{d}\begin{pmatrix} 1 \\ 1/\sqrt{3} \end{pmatrix} \quad , \qquad \mathbf{G}_2 = \frac{2\pi}{d}\begin{pmatrix} -1 \\ 1/\sqrt{3} \end{pmatrix} \tag{3.30}$$

(see also Fig. 2.2b).

We assume a lattice spacing $d = 25$ nm and use an effective Gaussian exciton-electron model potential

$$V_\mathrm{eff}(r) = -V_0\, \mathrm{e}^{-(r/\sigma)^2/2} \ , \tag{3.31}$$

with width $\sigma \approx 2.4$ nm to approximate the behavior far away from the resonance found from the three-body results for exciton-electron scattering ($E_s \approx 6$ meV). The exciton band structure that results from the diagonalization of the Hamiltonian in reciprocal space is shown in the upper half of Fig. 3.11 as the system is tuned across the Feshbach resonance. As shown in Fig. 3.11(d) the potential depth V_0 (measured in units of the characteristic lattice energy $E_\mathrm{rec} = \hbar^2\mathbf{G}^2/2m_X = 2.81$ meV, with exciton mass m_X and reciprocal lattice vector $\mathbf{G}$) is tuned to generate scattering parameters E_s as relevant for our Feshbach resonance data in Fig. 3.10. Fig. 3.11(a) corresponds to the scenario realized in presence of a single deeply-bound trion (blue in (c), not shown on the scale of the figure); in this case, the band structure is renormalized upwards with respect to the free bands (shown in gray).

As the resonance is crossed, the newly emerging trion state creates a molecular band (see Fig. 3.11(b), orange band), while the first excited exciton band (corresponding to a repulsive polaron in the continuum case) now features a negative band mass. Interestingly, both bands feature a significant oscillator strength, as can be seen from the linear-response absorption spectra shown in the respective right subpanels of Fig. 3.11(a,b). The combination of large oscillator strength and negative effective mass may provide a way to study anomalous exciton diffusion. In the regime where the molecular band (corresponding to an attractive polaron in the continuum case) is slightly below the first excited band, it takes the role of a tight binding band. Since this band is addressable spectroscopically, the direct realization of tight-binding Hubbard models of exciton should become possible.

We now turn to the spectral signatures of the different bands, whose oscillator strengths are proportional to the overlap with the bare zero momentum exciton

$$A(\omega) \propto |\, \langle X^\mathrm{bare}_{k=0} | X_{k=0} \rangle \,|^2 \ . \tag{3.32}$$

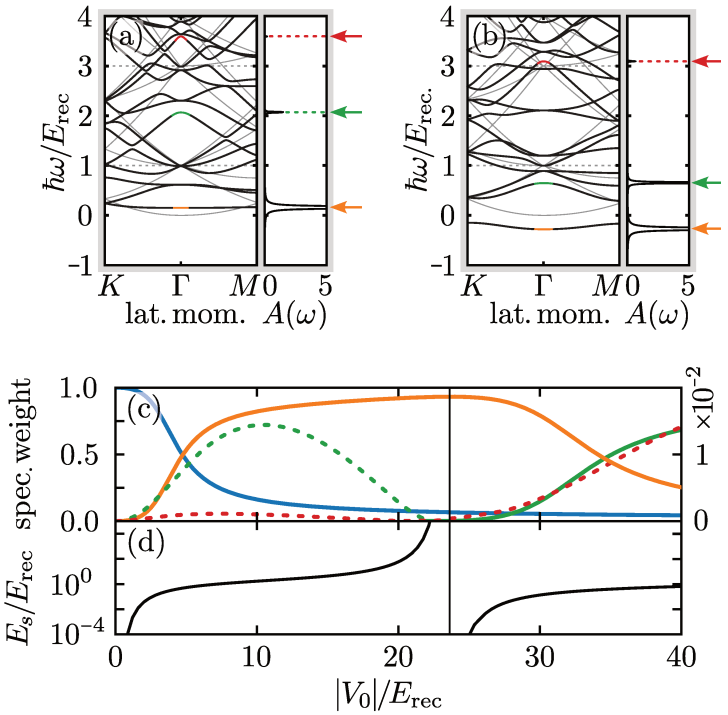

Figure 3.11.: Band structures of excitons in a triangular lattice of electrons for different depths of the Gaussian model potential $V_0 = 10\,E_{\mathrm{rec}}$ (a) and $V_0 = 30\,E_{\mathrm{rec}}$ (b) with $E_{\mathrm{rec}} = \hbar^2\mathbf{G}^2/2m_X$. The absorption spectra $A(\omega)$ are shown in the right panels respectively. Colored arrows mark the absorption peak positions corresponding to their spectral weight shown in (c) as color matching lines. The energy corresponding to the blue line exceeds the scale of (a,b). (c) shows the spectral weight of the corresponding peaks where dashed lines correspond to Umklapp peaks plotted against the zoomed-in right y-axis (while solid lines correspond to the spectral weight of polaron branches in the continuum limit). (d) shows the two-dimensional scattering parameter E_s resulting from a fit to the first scattering state obtained from diagonalizing the Hamiltonian describing an exciton interacting with an immobile electron via the Gaussian model potential inside a two-dimensional box.

Following the computational procedure in Ref. [41], we show the oscillator strength of the lowest four absorption peaks across the Feshbach resonance in Fig. 3.11(c). The peaks can be assigned to states that arise from Umklapp scattering (dashed lines plotted against the zoomed in right axis). Peaks that correspond to trions and the exciton-charge scattering threshold (solid lines) correspond to polarons in the continuum case.

On the left, a single trion state (attractive polaron, blue line) is present which becomes increasingly bound for growing V_0 where the binding energy of this artificial state quickly becomes too large, exceeding the physical regime. The Umklapp peak (dashed green line) is rather small compared to the strength of the repulsive polaron peak (orange line in

Fig. 3.11c). While the oscillator strength of the first Umklapp peak increases at first it becomes again smaller as the Feshbach resonance (vertical solid line in Fig. 3.11c,d) is approached, where it eventually vanishes and the system becomes effectively non-interacting.

At the resonance the absorption spectrum is dominated by the previously repulsive polaron which has maximal oscillator strength and is converted into an attractive polaron while a new repulsive branch emerges with zero oscillator strength (see solid green line in Fig. 3.11c). After crossing the resonance the oscilator strength of the Umklapp peak (now dashed red line, which was the second Umklapp peak on the left side of the resonance) again increases. This process of conversion and emerging of peaks repeats itself whenever a new bound state is created in the interaction potential by increasing $|V_0|$. This is in full accordance to the discussion of the Fermi-polaron problem in Section 3.1.1. Also see Fig. 3.4.

3.4. Summary

In this chapter we have shown how tunable exciton-electron interactions in two-dimensional TMD heterostructures arise from first principles. We found two types of resonances that allow to tune the interaction strength of either short-lived intralayer or long-lived interlayer excitons and electrons. The first may allow to use optically injected excitons as a probe of electronic states in van der Waals heterostructures, by controllably coupling them to electrons. The latter promise the prospect to realize controllable many-body systems comprised of long-lived, dipolar interlayer excitons and electrons. In this context the tunability of interactions following from the Feshbach resonances described in this chapter might enable exciton-induced superconductivity [89–91] or supersolidity in dipolar exciton condensates [92–94].

Further we have studied excitons moving in lattices formed by two-dimensional charge-ordered states in TMDs. Here the previously introduced Feshbach resonances were used to tune the exciton-lattice interactions. The emerging excitonic bands could be tuned to a regime with negative curvature, suggesting a negative effective exciton mass, indicating the presence of anomalous exciton diffusion.

4. Towards an Effective Theory Description of Exciton-Charge Feshbach Resonances

The development of effective models is crucial for the understanding of many-body systems, e.g., BCS theory for the understanding of superconductivity [19] that describes the binding of electrons into Cooper pairs by an exchange of phonons, or the theory of strong forces that describes the scattering of bound nucleons instead the detailed physics of quarks and gluons [95]. In the context of ultracold atoms, two-channel models for Feshbach resonances were crucial to get key insight into the physics of polarons or the BEC-BCS crossover [96]. In this chapter we aim to develop an effective theory for excitons scattering with electrons in TMDs that does not rely on resolving the full dynamics of all charge carriers, but rather describes the scattering of excitons and electrons. The approach we use here is heavily inspired by two-channel models [73] and aims to establish an even closer connection between the scattering of excitons and electrons in TMDs and atoms in ultracold atomic systems. In this regard our approach differs crucially from our recent work in [P3] where the coupling of the different scattering channels is achieved by explicitly including hole tunneling in the effective Hamiltonian. Here we use the conversion of scattering states and bound states to couple open and closed-channels, as known from typical two-channel models used for describing Feshbach resonances in ultracold gases (see Section 2.2.2). The results of this chapter represent another so far unpublished result of this thesis.

The ab initio results for the low-energy spectrum obtained from an exact diagonalization of the three-body problem (discussed in Section 3.2) have revealed two interesting anticrossings between different exciton-electron scattering thresholds and trions. The strong coupling between these states in the vicinity of these anticrossings modifies the scattering processes similar to the situation in ultracold atoms. Motivated by these findings we develop an effective many-body description of exciton-charge scattering that captures the binding energies of trions within a model correctly describing exciton-electron scattering while being simple enough to be suitable for many-body calculations. To establish the approach the results of this effective description are compared to a simplified

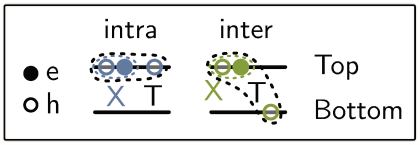

Figure 4.1.: Illustration of the different charge configurations and possible intra and interlayer trions used in the multi-channel model. Please note that the interlayer trion (depicted in green) is not bound within the more physical interaction potential used in Section 3.2.

three-body calculation, where a bilayer Rytova-Keldysh potential[1] is used to model the electron-hole interactions. This approximation is valid if the layer separation vanishes and the two hypothetical layers, in which the particles are confined, lie directly on top of each other.

Further, in contrast to the previous discussion, the three-body results are obtained for two holes and one electron (again in a bilayer structure of $MoSe_2$). The configurations relevant to the following discussion are illustrated in Fig. 4.1. Although the interlayer trion formed by the scattering of an intralayer exciton and a hole in the bottom layer (found to exist using the bilayer Rytova-Keldisch model potential) is not present in the more physical potential used above in Section 3.2 (see Eq. (3.26)), the overall ability of the effective theory to capture the behavior of the three-body results is expected to remain valid, e.g., in the context of two electrons interacting with one hole as studied in Section 3.2.

4.1. Model

Motivated by the parallels to ultracold atoms, we investigate a two-channel like model by considering the following Hamiltonian

$$\begin{aligned}\hat{H} = &\sum_{s\boldsymbol{k}} \left(\tilde{\epsilon}^s_{\boldsymbol{k}} + \xi^s\,\Delta E\right) \hat{h}^{s\,\dagger}_{\boldsymbol{k}} \hat{h}^s_{\boldsymbol{k}} + \sum_{\boldsymbol{k}} (\tilde{\omega}_{\boldsymbol{k}} + E_X)\, \hat{X}^\dagger_{\boldsymbol{k}} \hat{X}_{\boldsymbol{k}} \\ &+ \sum_{s\boldsymbol{k}} \left(\tilde{\Omega}^s_{\boldsymbol{k}} + E^s_t + \xi^s \Delta E\right) \hat{t}^{s\,\dagger}_{\boldsymbol{k}} \hat{t}^s_{\boldsymbol{k}} \\ &+ \sum_{ss'\boldsymbol{pq}} g^{s'}_s\, \chi_s\!\left(\frac{m_h \boldsymbol{q} - m_x \boldsymbol{p}}{m_h + m_x}\right) \hat{t}^{s\,\dagger}_{\boldsymbol{p}+\boldsymbol{q}} \hat{X}_{\boldsymbol{p}} \hat{h}^{s'}_{\boldsymbol{q}} + \text{h.c.}\,,\end{aligned} \tag{4.1}$$

where $\hat{X}_{\boldsymbol{k}}$ is an annihilation operator of an intralayer exciton (treated as a rigid point-like particle) with energy $\tilde{\omega}_{\boldsymbol{k}}$ in the top layer. The operator $\hat{h}^s_{\boldsymbol{k}}$ annihilates a hole in

[1] We use Eq. (2.1) with the substitutions $r_0 \to r_0^{\mathrm{TMD}_1} + r_0^{\mathrm{TMD}_2}$ and $r \to \rho^{ab}(r) = \sqrt{r^2 + \delta_{ab} d^2}$ to account for the layer separation d caused by the finite thickness of the TMD layers separated by a monolayer of hBN. Note this approximation is strictly only valid in the limit $d \to 0$.

layer $s \in \{\mathrm{T}, \mathrm{B}\}$ with dispersion relation $\tilde{\epsilon}^s_{\boldsymbol{k}}$, and $\hat{t}^s_{\boldsymbol{k}}$ is the annihilation operator of the corresponding trion with dispersion $\tilde{\Omega}^s_{\boldsymbol{k}}$. Here we aim to study a model that reproduces the scattering of holes and excitons where both particles have fixed effective layer index (thus layer tunneling is effectively integrated out). The last term couples excitons and holes via the formation of trions with coupling strengths $g^{s'}_s$ (for the connection between real space and momentum space formulation of the interaction term, see Appendix D). The parameters E_X and E^s_t represent the bare binding energies of excitons and trions that are renormalized due to the Yukawa type interactions terms in the last line of Eq. (4.1). In the following we choose the notation

$$\begin{aligned} \epsilon^s_{\boldsymbol{k}} &= \tilde{\epsilon}^s_{\boldsymbol{k}} + \xi^s \, \Delta E \ , \\ \omega_{\boldsymbol{k}} &= \tilde{\omega}_{\boldsymbol{k}} + E_X \ , \\ \Omega^s_{\boldsymbol{k}} &= \tilde{\Omega}^s_{\boldsymbol{k}} + E^s_t + \xi^s \Delta E \ . \end{aligned} \tag{4.2}$$

The factors $\xi^{\mathrm{T}} = 0$ and $\xi^{\mathrm{B}} = -1$ account for the energy shift of holes in the intralayer (T) and interlayer (B) configuration due to the band detuning ΔE. The form factors $\chi_s(\boldsymbol{k})$ arise from a finite extent of the trion wave function. In order to obtain analytical solvable expressions we choose modified Bessel functions of the second kind $K_0(x)$ to describe the real-space form factors

$$\tilde{\chi_s}(r) = \frac{1}{\sqrt{\pi}\sigma_s} K_0\left(\frac{r}{\sigma_s}\right) \ , \tag{4.3}$$

from which the momentum-dependent form factors are obtained via Fourier transformation

$$\tilde{\chi_s}(r) \quad \overset{\mathcal{F}}{\to} \quad \chi_s(k) = \frac{2\sqrt{\pi}\,\sigma_s}{1 + k^2\sigma_s^2} \ . \tag{4.4}$$

4.2. Two-Body Solution

We are interested in the spectrum of Eq. (4.1) in the vicinity of the anticrossings of the exciton-electron scattering threshold and trions related to the Feshbach resonances obtained in the three-body solution. To analyze the spectrum we solve the Schrödinger equation using a wave function ansatz of the form (which is exact for the two-body problem considered here within our exciton-electron scattering model)

$$|\psi\rangle = \sum_s \alpha^s \hat{t}^{s\,\dagger}_0 \, |0\rangle + \sum_{s\boldsymbol{k}} \beta^s_{\boldsymbol{k}} \hat{X}^\dagger_{-\boldsymbol{k}} \hat{h}^{s\,\dagger}_{\boldsymbol{k}} \, |0\rangle \ . \tag{4.5}$$

The parameters α, β are determined from the Schroedinger equation by (functional) derivatives of

$$L = \frac{\langle\psi| \, \hat{H} \, |\psi\rangle}{\langle\psi|\psi\rangle} = \min \quad \Leftrightarrow \quad \langle\psi| \, \hat{H} - E \, |\psi\rangle = \min \ , \tag{4.6}$$

with respect to $\alpha^{\mathrm{T/B}}$ and $\beta_{\boldsymbol{k}}^{\mathrm{T/B}}$. To this end, we compute

$$\begin{aligned}\langle\psi|\,\hat{H}-E\,|\psi\rangle = &\sum_{s}|\alpha^{\mathrm{s}}|^2\Omega_0^{\mathrm{s}}+\sum_{s\,\boldsymbol{k}}|\beta_{\boldsymbol{p}}^{s}|^2\big(\epsilon_{\boldsymbol{k}}^{s}+\omega_{\boldsymbol{k}}\big)\\ &+\sum_{ss'}\alpha^{s}g_{s}^{s'}\frac{1}{\sqrt{A}}\sum_{\boldsymbol{p}}\beta_{\boldsymbol{p}}^{s'}\chi_s(\boldsymbol{p})+\mathrm{h.c.}\\ &-E\left(\sum_{s}|\alpha^{s}|^2+\sum_{s\,\boldsymbol{p}}|\beta_{\boldsymbol{p}}^{s}|^2\right)\,,\end{aligned}\tag{4.7}$$

allowing to arrive at

$$\begin{aligned}&\frac{\partial L}{\partial\alpha^{s*}}\overset{!}{=}0\quad\Leftrightarrow\quad\alpha^{s}\Omega_0^{s}+\sum_{s'}g_{s}^{s'}\frac{1}{\sqrt{A}}\sum_{\boldsymbol{p}}\beta_{\boldsymbol{p}}^{s'}\chi_s(\boldsymbol{p})-\alpha^{s}E\overset{!}{=}0\,,\\ &\frac{\partial L}{\partial\beta_{\boldsymbol{p}}^{s'*}}\overset{!}{=}0\quad\Leftrightarrow\quad\sum_{s}\alpha^{s}g_{s}^{s'}\frac{1}{\sqrt{A}}\chi_s(\boldsymbol{p})+\beta_{\boldsymbol{p}}^{s'}\Big(\epsilon_{\boldsymbol{p}}^{s'}+\omega_{\boldsymbol{p}}-E\Big)\overset{!}{=}0\,.\end{aligned}\tag{4.8}$$

The second equation yields relations for $\beta_{\boldsymbol{p}}^{s'}$

$$\beta_{\boldsymbol{p}}^{s'}=-\frac{\sum_{s''}\alpha^{s''}g_{s''}^{s'}\frac{1}{\sqrt{A}}\chi_{s''}(\boldsymbol{p})}{\epsilon_{\boldsymbol{p}}^{s'}+\omega_{\boldsymbol{p}}-E}\,,\tag{4.9}$$

that can be used to eliminate the $\beta_{\boldsymbol{p}}^{s'}$ dependency in the first line of Eq. (4.8) what implicitly solves the momentum dependent part of the of the Schrödinger equation allowing to reduce the infinite-dimensional set of equations (given in Eq. (4.8)) to two equations (i.e., $s\in\{\mathrm{T},\mathrm{B}\}$)

$$\alpha^{s}\Omega_0^{s}-\sum_{s'}g_{s}^{s'}\frac{1}{A}\sum_{\boldsymbol{p}}\frac{\sum_{s''}\alpha^{s''}g_{s''}^{s'}\chi_{s''}(\boldsymbol{p})}{\epsilon_{\boldsymbol{p}}^{s'}+\omega_{\boldsymbol{p}}-E}\chi_s(\boldsymbol{p})-\alpha^{s}E\overset{!}{=}0\,.\tag{4.10}$$

It is instructive to take the continuum limit by replacing

$$\frac{1}{A}\sum_{\boldsymbol{p}}\quad\longrightarrow\quad\int\frac{\mathrm{d}^2\boldsymbol{p}}{(2\pi)^2}\,,\tag{4.11}$$

and identify the respective self-energies

$$\Sigma^{s_1,s_2,s_2}(E)=\int\frac{\mathrm{d}^2\boldsymbol{p}}{(2\pi)^2}\frac{\chi_{s_2}(p)\,\chi_{s_3}(p)}{E-\epsilon_{\boldsymbol{p}}^{s_1}+\mathrm{i}\epsilon}\,.\tag{4.12}$$

This allows to rewrite Eq. (4.10)

$$\alpha^{s}\left(\Omega_0^{s}-E\right)-\sum_{s'\,s''}\alpha^{s''}g_{s}^{s'}g_{s''}^{s'}\Sigma^{s',s'',s}(E)\overset{!}{=}0\,,\tag{4.13}$$

which can be expressed as a matrix equation[2] with an energy dependent coefficient

[2] Eigenstates of the Schrödinger equation (see Eq. (4.5)) fulfill this relation. Note that $\det[\boldsymbol{M}]=0$ in order to ensure the existence of a nontrivial solution.

matrix $\boldsymbol{M}$

$$\underbrace{\begin{pmatrix} a & b \\ c & d \end{pmatrix}}_{=\boldsymbol{M}} \begin{pmatrix} \alpha^{\mathrm{T}} \\ \alpha^{\mathrm{B}} \end{pmatrix} = \mathbf{0} \ , \tag{4.14}$$

where

$$\begin{aligned} a &= \Omega_0^{\mathrm{T}} - E - |g_{\mathrm{T}}^{\mathrm{B}}|^2 \frac{1}{A} \Sigma^{\mathrm{BTT}}(E) - |g_{\mathrm{T}}^{\mathrm{T}}|^2 \frac{1}{A} \Sigma^{\mathrm{TTT}}(E) \ , \\ d &= \Omega_0^{\mathrm{B}} - E - |g_{\mathrm{B}}^{\mathrm{B}}|^2 \frac{1}{A} \Sigma^{\mathrm{BBB}}(E) - |g_{\mathrm{B}}^{\mathrm{T}}|^2 \frac{1}{A} \Sigma^{\mathrm{TBB}}(E) \ , \\ b &= g_{\mathrm{T}}^{\mathrm{B}} g_{\mathrm{B}}^{\mathrm{B}*} \frac{1}{A} \Sigma^{\mathrm{BBT}}(E) - g_{\mathrm{T}}^{\mathrm{T}} g_{\mathrm{B}}^{\mathrm{B}*} \frac{1}{A} \Sigma^{\mathrm{TBT}}(E) \ , \\ c &= g_{\mathrm{B}}^{\mathrm{B}} g_{\mathrm{T}}^{\mathrm{B}*} \frac{1}{A} \Sigma^{\mathrm{BTB}}(E) - g_{\mathrm{B}}^{\mathrm{T}} g_{\mathrm{T}}^{\mathrm{T}*} \frac{1}{A} \Sigma^{\mathrm{TTB}}(E) \ . \end{aligned} \tag{4.15}$$

The spectral functions are given by the imaginary part of the retarded Green's functions $G_s^{\mathrm{r}} = \langle 0 | \, \hat{t}_0^s \ 1/[\hat{H} - E - \mathrm{i}0^+] \, \hat{t}_0^{s\,\dagger} \, | 0 \rangle$, i.e.,

$$A^s(E, \Delta E) = \mathrm{Im} \left[G_s^{\mathrm{r}}(E, \Delta E) \right] \ , \tag{4.16}$$

that follow from the resolvent $1/[\hat{H} - E]$ by shifting the energy $E \to E + \mathrm{i}0^+$. As Eq. (4.14) is nothing but a reformulation of the system of equations obtained from the variation of the eigenvalues of the inverse resolvent after solving the momentum dependence (see Eq. (4.8)), i.e.,

$$\frac{\partial}{\partial \alpha^{s\,*}} \langle \psi | \, \hat{H} - E \, | \psi \rangle \stackrel{!}{=} 0 \ , \tag{4.17}$$

the retarded Green's functions are given directly by the entries of the main diagonal of the matrix $\boldsymbol{M}^{-1}$ after shifting $E \to E + \mathrm{i}0^+$.

4.3. Results and Discussion

We can now turn to the question how well the model Eq. (4.1) can reproduce the energy spectrum of the underlying three-body problem. To this end, the parameters $\sigma^s, g_s^{s\prime}$, E_X^s and E_t^s of the model are obtained by fitting the spectrum to the three-body results. The resulting spectrum is shown in Fig. 4.2, where the discrete set of energies of the underlying three-body solution is shown as orange curves. The spectrum obtained from Eq. (4.16) in turn is overlaid as an density (color) plot. As evident, we find a remarkable capability of the effective multi-channel model to reproduce the spectrum of the first-principle three-body calculation. Our preliminary findings thus demonstrate

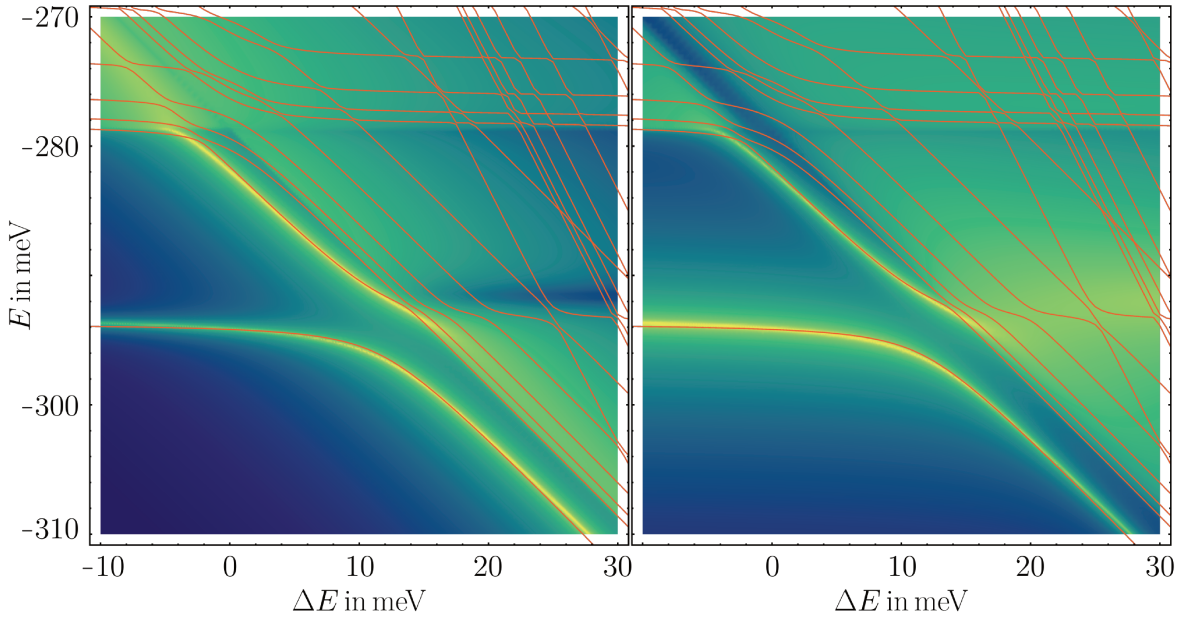

Figure 4.2.: The left (right) panel shows the interlayer (intralayer) spectral function $A(E, \Delta E)$ in arb. units, with band detuning ΔE, where bright colors indicate large weight. The orange lines are the eigenenergies of the corresponding three-body problem (two holes and one electron interacting via a bilayer Rytova-Keldysh potential).

that exciton-electron scattering in two-dimensional semiconductors is well described by essentially the same type of models used in ultracold atoms to effectively describe the scattering of ultracold atoms close to Feshbach resonances. This further strengthens the analogy between two-dimensional materials and ultracold atoms.

4.4. Open Questions

In the same way the spectral properties can be reproduced by an ultracold-atom inspired effective many-body model, we expect that the study of the corresponding T-matrix (similarly to the two-channel model presented in Section 2.2.2) will exhibit scattering properties that can reproduce also the low-energy phase shift as found in the three-body solution. Moreover, we expect that this low-energy scattering can be described using relations similar to Eq. (2.3) where the band detuning ΔE takes over the role of the magnetic field B in the parameterization of the scattering length around the Feshbach resonance. This derivation of a relation that allows to characterize Feshbach resonances in atomically thin semiconductors is left for future work.

Part II.

Rydberg Excitations as a Probe of Quantum Matter

Part II is based on the publications [P1], [P2] and [P4].
Additional unpublished material is discussed in Chapter 6.

Ultracold atoms provide a versatile platform to study quantum many-body physics. In this context Rydberg excitations – atoms in which an electron is excited to an orbital with high principal quantum number – are naturally embedded in a many-body environment, as they are usually excited from within a cloud of atoms. The Rydberg blockade radius is typically much larger than the inter-particle distance, and can, in extreme cases, even reach up to the extent of the ultracold cloud, ensuring that Rydberg atoms immersed in ultracold atoms are well described by single impurity models [97]. The interactions between a Rydberg impurity and the surrounding atoms are dominated by the attraction mediated by the scattering of the neutral atoms and the Rydberg electron on its highly excited orbit. The resulting attractive interaction potential can support the formation of bound states, ultralong-range Rydberg molecules (ULRRMs) [98, 99]. Further, these bound states which may contain multiple atoms (dimer, trimer, tetramer states, and so on) themselves are dressed by excitations of atoms in the vicinity of the Rydberg atom. This leads to the formation of a series of Rydberg polarons, which manifest in characteristic peaks in the Rydberg absorption spectrum [100, 101].

In an intuitive, semiclassical picture one can think of the Rydberg electron as a point-like particle orbiting the core at a distance given by the Rydberg radius. The scattering of a ground-state atom and the Rydberg electron, leads to the formation of a bound state with a well defined binding length, precisely given by the Rydberg radius. The probability that such bound-state formation occurs grows with increasing number of ground-state atoms located on the Rydberg electron orbit.

The following second part of this thesis is focused around the idea to use Rydberg excitations as a means to detect correlations in ultracold atomic systems. To this end, one may recognize that, if a ground-state atom is excited to a Rydberg state by a laser with narrow line width, and the laser frequency is detuned by the ULRRM binding energy, only ULRRMs of a matching binding length (determined by the principal quantum number n of the Rydberg excitation) and matching number of neutral atoms bound in the Rydberg potential are created. Focusing here on the dimer, this establishes a direct connection between the absorption of photons of a certain frequency and the creation of an ULRRM with matching binding length, which itself reflects the probability of two atoms (one being the Rydberg atom, the other the neutral atom) having this particular separation in the ultracold cloud. Therefore the strength of the dimer-peak in the absorption spectrum should be related to the probability distribution of inter-particle spacings in the ultracold gas, i.e., the pair correlation function, evaluated at the binding length of the ULRRM, given by the respective Rydberg radius. Importantly, the ULRRM formation takes place on timescales set by the molecular binding energies in the MHz range, which is fast compared to time scales of typical ultracold-atom dynamics. This suggests that the ULRRM formation process can be used as an in-situ, time-resolved probe of the quantum gas surrounding the Rydberg atom.

In the following we develop a theoretical description of this idea, i.e., of using Rydberg excitations as a probe of correlations within a cloud of ultracold atoms in which the Rydberg state is created. First we provide a short reminder of ULRRMs before we show

that the spectroscopic response of the ULRRM-dimer peak is indeed proportional to the pair correlation function when the quantum state from which it was created can be represented as Fock state. We then apply this method on two examples and outline possible future research directions. In the end of this part we discuss a related topic, studying how Rydberg impurities in a BEC can be described by a semiclassical theory.

5. Ultralong-Range Rydberg Molecules

In order to understand how Rydberg excitations can be used to detect correlations in ultracold quantum gases we first give a short overview of the effects dominating the Rydberg-ground-state-atom interaction, leading to the formation of ultralong-range Rydberg molecules (ULRRMs). More detailed information on the underlying physics can be found in the reviews [102, 103].

5.1. Rydberg-Ground-State-Atom Interaction

When a Rydberg atom is excited within a cloud of ultracold atoms the Rydberg electron scatters with atoms in its environment, thereby mediating an interaction (see Fig. 5.1). This interaction leads to shift of the energy of the collective state of the Rydberg atom and the neighboring atoms, which modify (perturb) the bare Rydberg excitation and are therefore called 'perturbers' in this context. The Rydberg-atom-perturber interaction potential has two contributions

$$V(\boldsymbol{r}) = V_{\mathrm{ca}}(\boldsymbol{R}) + V_{\mathrm{ea}}(\boldsymbol{R}, \boldsymbol{r}) \ , \tag{5.1}$$

namely the Rydberg-core-perturber interaction V_{ca} and the Rydberg-electron-perturber interaction V_{ea}. They are given by the polarization potential of the neutral ground-state atom in the electric field of the Rydberg ionic core and the Rydberg electron

$$V_{\mathrm{ca}}(\boldsymbol{R}) = -\frac{e^2}{(4\pi\varepsilon_0)^2}\frac{\alpha}{2\boldsymbol{R}^4} \quad , \quad V_{\mathrm{ea}}(\boldsymbol{R}, \boldsymbol{r}) = -\frac{e^2}{(4\pi\varepsilon_0)^2}\frac{\alpha}{2|\boldsymbol{R}-\boldsymbol{r}|^4} \ , \tag{5.2}$$

where e is the elementary charge, ε_0 the vacuum permittivity and α the polarizability of the ground-state atom.

The Hamiltonian describing the Rydberg electron is given by

$$\hat{H}_{\mathrm{el}} = -\frac{\hbar^2}{2m_{\mathrm{e}}}\Delta - \frac{e^2}{4\pi\varepsilon_0}\frac{1}{|\hat{\boldsymbol{r}}|} - \frac{e^2}{(4\pi\varepsilon_0)^2}\sum_i \frac{\alpha}{2|\boldsymbol{R}_i - \hat{\boldsymbol{r}}|^4} \ , \tag{5.3}$$

where the first term accounts for the kinetic energy of the Rydberg electron with the electron mass m_{e}, the second term accounts for its approximate Coulomb interaction with the Rydberg core and the last term for its interaction with the ground-state atoms

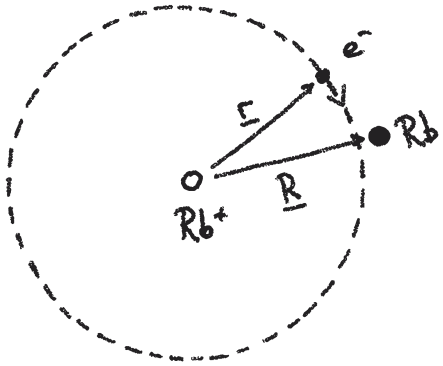

Figure 5.1.: Sketch of the Rydberg atom interacting with a ground-state atom, at the example of Rb. The dashed line marks the semi-classical Rydberg orbit.

which depends parametrically on their positions $\boldsymbol{R}_i$. The Rydberg-electron-perturber interaction can be treated within the framework of Fermi pseudopotentials[1] [105]. The idea behind the introduction of Fermi pseudopotentials is based on a low-energy expansion that allows to simplify the treatment of the last term in Eq. (5.3) which would otherwise only be possible in a purely numerical fashion. The idea that the electronic wave function is modified only locally in close vicinity of the perturbers allows to effectively describe their interaction in terms of contact interactions [106]

$$\frac{e^2}{(4\pi\varepsilon_0)^2}\frac{\alpha}{2|\boldsymbol{R}_i-\hat{\boldsymbol{r}}|^4} \quad \rightarrow \quad \int \mathrm{d}^3\boldsymbol{r} V_{\mathrm{pseudo}}(\boldsymbol{r}-\boldsymbol{R}_i)|\psi_{\mathrm{el}}(\boldsymbol{r})|^2 \ , \tag{5.4}$$

with the Fermi pseudopotential

$$V_{\mathrm{pseudo}}(\boldsymbol{r}) = \frac{2\pi\hbar^2 a_{\mathrm{s}}}{m_{\mathrm{e}}}\ \delta^{(3)}(\boldsymbol{r}) \ , \tag{5.5}$$

where a_s is the s-wave scattering length between the electron and the neutral atom. Higher-order order scattering terms can be treated in a similar way and one obtains the Born-Oppenheimer energy curves by solving the electronic problem for fixed perturber positions $\boldsymbol{R}$ (here in case of a single perturber)

$$E(\boldsymbol{R}) = -\frac{m_e e^4}{8\varepsilon_0^2 h^2}\frac{1}{2(n-\delta_0)} - \frac{e^2}{(4\pi\varepsilon_0)^2}\frac{\alpha}{2R^4} + \frac{2\pi\hbar^2 a_{\mathrm{s}}}{m_{\mathrm{e}}}|\psi_{\mathrm{el}}(\boldsymbol{R})|^2 + \frac{6\pi\hbar^2 a_{\mathrm{p}}^3}{m_{\mathrm{e}}}|\boldsymbol{\nabla}\psi_{\mathrm{el}}(\boldsymbol{R})|^2 \ , \tag{5.6}$$

where δ_0 is the quantum defect that accounts for the effects of the shielding of the Rydberg atom nucleus by tightly bound electrons, and a_{p} is the p-wave scattering length of Rydberg-electron-ground-state-atom scattering. The function $E(\boldsymbol{R})$ represents the

[1] Fermi introduced this description of quantum scattering including zero-range pseudopotentials as explanation of spectral excitation lines of Rydberg excitations in a dense gas of atoms [104].

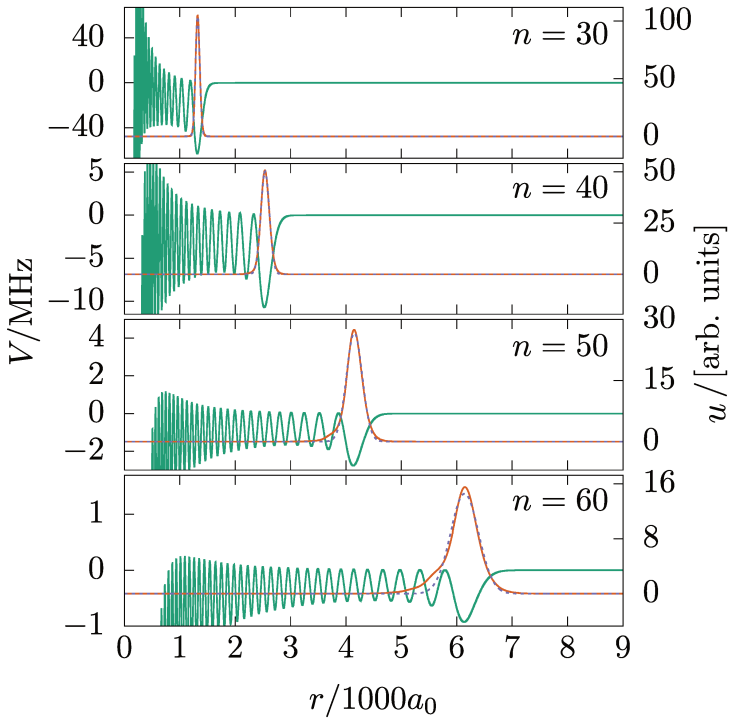

Figure 5.2.: Radial s-wave potential landscape V_{ULRRM} (green) and radial wave functions $u(r)$ (orange) of the lowest ULRRM-dimer state for ^{87}Sr and different principal quantum numbers n. The dashed lines show Gaussian fits of the radial wave functions.

energy landscape for perturbers around a Rydberg atom. Thus the interaction potential of a ground-state and a Rydberg atom is given by

$$V_{\mathrm{ULRRM}}(\boldsymbol{r}) = -\frac{e^2}{(4\pi\varepsilon_0)^2}\frac{\alpha}{2r^4} + \frac{2\pi\hbar^2 a_{\mathrm{s}}}{m_{\mathrm{e}}}|\psi_{\mathrm{el}}(\boldsymbol{r})|^2 + \frac{6\pi\hbar^2 a_{\mathrm{p}}^3}{m_{\mathrm{e}}}|\boldsymbol{\nabla}\psi_{\mathrm{el}}(\boldsymbol{r})|^2 \ , \tag{5.7}$$

whose long range behavior is dominated by the terms caused by the highly oscillating Rydberg electronic wave function (see green curves in Fig. 5.2).

The next step is to solve the relative Schrödinger equation for a ground-state atom interacting with a Rydberg atom

$$\left[-\frac{\hbar^2}{2\mu}\Delta + V_{\mathrm{ULRRM}}(r)\right]\phi_{\nu lm}(\boldsymbol{r}) = E_{\nu l}\,\phi_{\nu lm}(\boldsymbol{r}) \ , \tag{5.8}$$

where μ is the reduced mass. The indices ν, l and m label the principal quantum number, angular momentum quantum number and angular momentum projection quantum number. The ansatz for the wave functions

$$\phi_{\nu lm}(\boldsymbol{r}) = \frac{u_{\nu l}(r)}{r}\,Y_{lm}(\theta,\varphi) \tag{5.9}$$

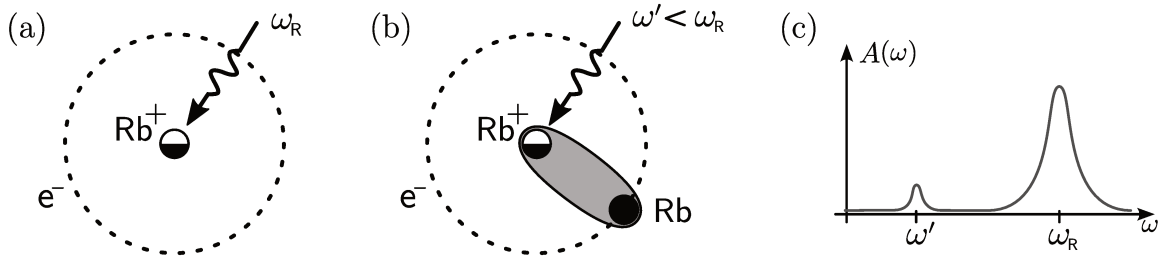

Figure 5.3.: (a) A Rydberg atom is excited at frequency ω_{R}. (b) A Rydberg molecule is excited at frequency $\omega' < \omega_{\mathrm{R}}$. (c) Simplified sketch of a typical Rydberg absorption spectrum (freely based on [99]).

separates the radial and angular part and allows to find the radial Schrödinger equation

$$\left[-\frac{\hbar^2}{2\mu}\partial_r^2 + \frac{\hbar^2}{2\mu}\frac{l(l+1)}{r^2} + V_{\mathrm{ULRRM}}(r)\right] u_{\nu l}(r) = E_{\nu l}\, u_{\nu l}(r)\ . \tag{5.10}$$

Fig. 5.2 shows the $l = 0$ ULRRM interaction potential and the resulting radial wave functions of the corresponding lowest ULRRM-dimer states, which are well approximated by a Gaussian (dashed lines in Fig. 5.2)

$$u_{\nu 0}(r) \sim \mathrm{e}^{-\frac{(r-r_{\mathrm{D}})^2}{4\sigma_\nu^2}}\ . \tag{5.11}$$

These bound states of Rydberg atoms and ground-state atoms were first observed by Bendkowsky et al. [99] using spectroscopic methods where one detects (via ionization of the Rydberg atom) if Rydberg excitations were created at a specific laser frequency which is detuned from the atomic Rydberg excitation energy. This allows for the reconstruction of Rydberg absorption spectra (see Fig. 5.3). In general such spectra contain two types of absorption peaks that can be either associated with the atomic Rydberg excitation or the formation of ULRRM bound states of on one or multiple neutral atoms. Depending on the density of the background gas these peaks are shifted with respect to the respective *bare* absorption peaks due to single-particle excitations of ground-state atoms in close vicinity of the Rydberg atom or ULRRM, reflecting the formation of Rydberg polarons [100]. Absorption peaks originating from ULRRM bound states exhibit a sub-structure of peaks, where each peak corresponds to a vibrational state of the underlying ULRRM [97].

It was found that the density of the ultracold background gas in which the Rydberg atom is excited affects the Rydberg absorption spectrum, specifically the mean of the absorption spectrum, which is red shifted with increasing density of the background gas [106, 107]. This indicates that Rydberg excitations in ultracold quantum gases can be used as a sensing tool of the ultracold environment.

In the following chapter we will expand on this idea. The particular shape of the ULRRM bound states, a ground-state atom located on a thin spherical shell (resembling the Rydberg orbit) with the Rydberg atom in its center in case of s-wave states, combined with the separation of timescales of molecule formation (∼MHz, fast) and typical dynamics of the environment (∼kHz, slow) will allow to use these molecules as probes for inter-particle distances in ultracold quantum gases.

6. Rydberg Excitations as a Probe of Quantum Gases

Interesting effects in systems of ultracold atoms (e.g., the formation Feshbach molecules, polarons, superfluid fermion pairs) typically occur on sub-optical length scales ($\lesssim 380$ nm) which makes them inherently difficult to in-situ detect and study in experimental setups. The typical radii of Rydberg atoms (50-500 nm), however, coincidentally fall into this regime. Combined with their ability to form detectable bound states with ground-state atoms, Rydberg excitations thus open up the possibility to probe inter-particle distances in ultracold quantum gases in the sub-optical regime that was previously inaccessible via standard optical detection methods.

Here we investigate the connection between the ULRRM-dimer response in the absorption spectrum and the pair correlation function of an ultracold gas from which the Rydberg atom is excited. The results of this chapter present another (so far unpublished) central result of this thesis. When the excitation frequency is detuned from the bare Rydberg excitation by the binding energy of an ULRRM dimer and the line width of the excitation laser is narrow enough such that the absorption of photons solely leads to the formation of ULRRM-dimer states with a specific binding length (see Fig. 6.1 a), the absorption rate of photons is a measure of the excitation probability of ULRRM-dimer states. In particular we use Fermi's golden rule to show that the ULRRM-dimer absorption strength is directly related to the system's pair correlation function.

6.1. A Molecule in an Ideal Fermi Sea

Having the ULRRM states in mind, we first investigate the creation of a general dimer molecule in a Fermi sea. Later we use the results of this section to compute the dimer absorption rate in the specific case of an ULRRM state created in a Fermi sea.

We use Fermi's golden rule and focus on the zero-temperature case, i.e.,

$$A(\omega) = \sum_{\mathrm{f}} \left| \langle \mathrm{f} | \, \hat{V}_{\mathrm{L}} \, | \mathrm{i} \rangle \right|^2 \delta\big(\omega - (E_{\mathrm{f}} - E_{\mathrm{i}})\big) \tag{6.1}$$

to predict the transition rate of the fermionic initial state $|\mathrm{i}\rangle$ into a final state $|\mathrm{f}\rangle$ caused by the laser operator $\hat{V}_{\mathrm{L}}$ that transfers a ground-state atom into a Rydberg state. Here ω is the laser frequency and the sum runs over all possible final states with energies E_{f}.

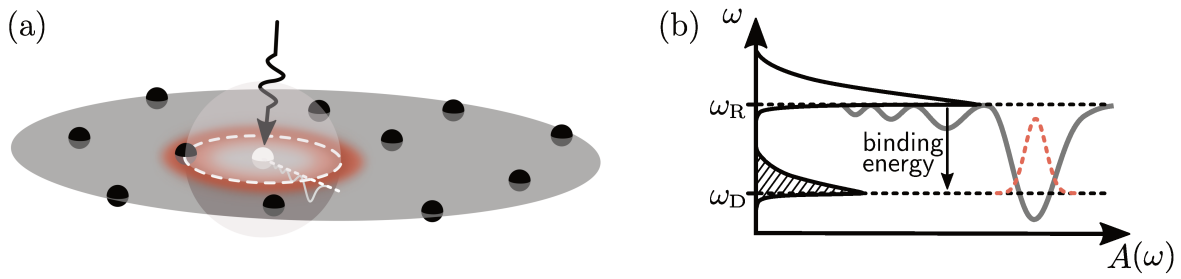

Figure 6.1.: (a) An atom from a cloud of ultracold atoms is excited into a Rydberg state (the illustration shows a cross section of a three-dimensional cloud). The excitation probability of an ULRRM dimer (i.e., absorption probability of a photon of the final excitation laser) scales with the probability of finding a ground-state atom within the outermost well (sphere and red shaded region) of the interaction potential. (b) Sketch of the corresponding Rydberg absorption spectrum. The ULRRM-dimer wave function in the ULRRM potential (bold gray line) is indicated as red dashed line.

The initial state $|i\rangle$ (with energy E_i) containing only ground-state atoms is an eigenstate of the Hamiltonian

$$H = \sum_{\boldsymbol{k}} \epsilon_{\boldsymbol{k}} \hat{c}^\dagger_{\boldsymbol{k}} \hat{c}_{\boldsymbol{k}} + \sum_{\boldsymbol{k}} \omega_{\boldsymbol{k}} \hat{d}^\dagger_{\boldsymbol{k}} \hat{d}_{\boldsymbol{k}} + \int \mathrm{d}^3\boldsymbol{r} \int \mathrm{d}^3\boldsymbol{r}' \; \hat{d}^\dagger_{\boldsymbol{r}} \hat{d}_{\boldsymbol{r}} V(\boldsymbol{r}-\boldsymbol{r}') \hat{c}^\dagger_{\boldsymbol{r}'} \hat{c}_{\boldsymbol{r}'} \;, \tag{6.2}$$

with momentum mode creation (annihilation) operators $\hat{c}^\dagger_{\boldsymbol{k}}$ ($\hat{c}_{\boldsymbol{k}}$) of ground-state fermions and Rydberg-atom momentum-mode creation (annihilation) operators $\hat{d}^\dagger_{\boldsymbol{k}}$ ($\hat{d}_{\boldsymbol{k}}$). The respective field operators are conveniently labeled by an index $\boldsymbol{r}$, where we use the convention

$$\hat{c}_{\boldsymbol{r}} = \frac{1}{\sqrt{V}} \sum_{\boldsymbol{k}} \mathrm{e}^{\mathrm{i}\boldsymbol{r}\boldsymbol{k}} \hat{c}_{\boldsymbol{k}} \;. \tag{6.3}$$

The interaction potential $V(\boldsymbol{r}-\boldsymbol{r}')$ may be given by the ULRRM potential Eq. (5.7) and the laser operator

$$\begin{aligned} \hat{V}_\mathrm{L} &= \int \mathrm{d}^3\boldsymbol{r} \; \hat{d}^\dagger_{\boldsymbol{r}} \hat{c}_{\boldsymbol{r}} + \mathrm{h.c.} \\ &= \sum_{\boldsymbol{k}} \hat{d}^\dagger_{\boldsymbol{k}} \hat{c}_{\boldsymbol{k}} + \mathrm{h.c.} \end{aligned} \tag{6.4}$$

excites a ground-state atom into a Rydberg state.

We assume the initial state to be given by a fermionic momentum-mode Fock state

$$|\mathrm{F}\rangle = \prod_{i=1}^{\infty} \left(\hat{c}^\dagger_{\boldsymbol{k}_i}\right)^{n_i} |0\rangle = |n_1, n_2, \ldots, n_i, \ldots, n_\infty\rangle \;, \tag{6.5}$$

which is equivalent to a Fermi sea of N particles if only the N lowest N modes are filled

$$|\mathrm{Fs}\rangle = \prod_{i=1}^{N} \left(\hat{c}^\dagger_{\boldsymbol{k}_i}\right) |0\rangle = |1, \ldots, \underset{(N)}{1}, 0, \ldots\rangle \ . \tag{6.6}$$

By a careful analysis of the commutation relations one finds that any Fock state results in the exact same expressions as the Fermi sea. Therefore we restrict the following discussion to the Fermi-sea scenario where the initial state is given by

$$|\mathrm{i}\rangle = \prod_{i=1}^{N} \left(\hat{c}^\dagger_{\boldsymbol{k}_i}\right) |0\rangle = |1, \ldots, \underset{(N)}{1}, 0, \ldots\rangle_c \otimes |0\rangle_d =: |\mathrm{FS}_c\rangle \ , \tag{6.7}$$

i.e., a Fermi sea of ground-state atoms and a vacuum of Rydberg atoms.

The relevant final states that are compatible with a laser frequency detuned from the Rydberg line by the ULRRM-dimer binding energy, are then states that result from the excitation of a single ground-state atom into a Rydberg state which is bound to another ground-state atom forming an ULRRM-dimer state. To describe these dimer bound states embedded in a fermionic environment we choose the ansatz

$$\begin{aligned} |\mathrm{f}\rangle &= |\mathrm{f}(\boldsymbol{\lambda}, \boldsymbol{\alpha}, \boldsymbol{p}, \boldsymbol{p}')\rangle \\ &= \int \mathrm{d}^3\boldsymbol{R} \int \mathrm{d}^3\boldsymbol{r}\, \Psi_{\boldsymbol{\lambda},\boldsymbol{\alpha}}(\boldsymbol{R}, \boldsymbol{r})\, \hat{d}^\dagger_{\boldsymbol{R}-\frac{\boldsymbol{r}}{2}}\, \hat{c}^\dagger_{\boldsymbol{R}+\frac{\boldsymbol{r}}{2}}\, \hat{c}_{\boldsymbol{p}}\, \hat{c}_{\boldsymbol{p}'}\, |\mathrm{i}\rangle \\ &= \int \mathrm{d}^3\boldsymbol{R}\, \Phi_{\boldsymbol{\lambda}}(\boldsymbol{R}) \int \mathrm{d}^3\boldsymbol{r}\, \phi_{\boldsymbol{\alpha}}(\boldsymbol{r})\, \hat{d}^\dagger_{\boldsymbol{R}-\frac{\boldsymbol{r}}{2}}\, \hat{c}^\dagger_{\boldsymbol{R}+\frac{\boldsymbol{r}}{2}}\, \hat{c}_{\boldsymbol{p}}\, \hat{c}_{\boldsymbol{p}'}\, |\mathrm{FS}_c\rangle \ , \end{aligned} \tag{6.8}$$

where $\boldsymbol{R}$ is the center-of-mass coordinate and $\boldsymbol{r}$ the relative distance between the dimer atoms. In this ansatz

$$\Psi_{\boldsymbol{\lambda},\boldsymbol{\alpha}}(\boldsymbol{R}, \boldsymbol{r}) = \Phi_{\boldsymbol{\lambda}}(\boldsymbol{R})\, \phi_{\boldsymbol{\alpha}}(\boldsymbol{r}) \tag{6.9}$$

are the molecular wave functions that will later be taken to describe the ULRRM dimer discussed in the previous chapter (see Chapter 5). The collective indices $\boldsymbol{\alpha}$ and $\boldsymbol{\lambda}$ combine all additional parameters on which the dimer state may depend (e.g., center-of-mass momentum or angular momentum of the molecule, etc.). We assume that any of the ground-state atoms can be excited to a Rydberg state. Further, it is possible for any ground-state atom to form a molecule with the excited Rydberg atom. Therefore any two of the ground-state atoms in modes $p, p' \leq k_\mathrm{F}$ may be annihilated from the initial Fermi sea and converted into a two-body bound state with wave function $\Psi_{\boldsymbol{\lambda},\boldsymbol{\alpha}}(\boldsymbol{R}, \boldsymbol{r})$. Within the bound state the position of the Rydberg atom is $\boldsymbol{R} + \frac{\boldsymbol{r}}{2}$ and the ground-state atom is located at $\boldsymbol{R} - \frac{\boldsymbol{r}}{2}$ (note that not all momentum modes can be occupied due to the Pauli exclusion principle). In Appendix E.1 we show that the resulting final states $|f\rangle$ defined by Eq. (6.8) are normalized.

We are interested in the absorption strength of all possible dimer states given by the ansatz in Eq. (6.8)

$$\bar{A} = \int_{\omega_{\mathrm{D}-}\frac{\Delta\omega}{2}}^{\omega_{\mathrm{D}+}\frac{\Delta\omega}{2}} \mathrm{d}\omega\, A(\omega) \approx \sum_{\mathrm{f}} \left| \langle \mathrm{f}| \hat{V}_{\mathrm{L}} |\mathrm{i}\rangle \right|^2 . \tag{6.10}$$

By averaging over a small frequency window $\Delta\omega$, centered around the excitation frequency of the dimer state ω_{D}, we are restricting all possible final states to the relevant subset which describes these dimer states embedded in a Fermi sea[1]. Thereby we assume that no other processes contribute to the absorptive response in this frequency window (cf. Fig. 6.1b). It is important to keep in mind that the final states $|f\rangle$ are not a complete set of basis states in the corresponding Hilbert space, i.e.,

$$\sum_{\mathrm{f}} |\mathrm{f}\rangle\langle \mathrm{f}| \neq \mathbb{1} . \tag{6.11}$$

By inserting all definitions into Eq. (6.10) we obtain

$$\begin{aligned}
\bar{A} &\approx \sum_{\mathrm{f}} \left| \langle \mathrm{f}| \hat{V}_{\mathrm{L}} |\mathrm{i}\rangle \right|^2 \\
&= \sum_{\boldsymbol{\lambda},\boldsymbol{\alpha}} \sum_{\boldsymbol{p},\boldsymbol{p}'} \Big| \langle \mathrm{FS}_c| \int \mathrm{d}^3\boldsymbol{R} \int \mathrm{d}^3\boldsymbol{r}\, \Psi^*_{\boldsymbol{\lambda},\boldsymbol{\alpha}}(\boldsymbol{R},\boldsymbol{r})\, \hat{c}^\dagger_{\boldsymbol{p}'}\, \hat{c}^\dagger_{\boldsymbol{p}}\, \hat{c}_{\boldsymbol{R}+\frac{\boldsymbol{r}}{2}}\, \hat{d}_{\boldsymbol{R}-\frac{\boldsymbol{r}}{2}} \\
&\qquad\qquad \times \left(\int \mathrm{d}^3\boldsymbol{r}_{\mathrm{L}}\, \hat{d}^\dagger_{\boldsymbol{r}_{\mathrm{L}}}\, \hat{c}_{\boldsymbol{r}_{\mathrm{L}}} + \mathrm{h.c.} \right) |\mathrm{FS}_c\rangle \Big|^2 \\
&= \sum_{\boldsymbol{\lambda},\boldsymbol{\alpha}} \sum_{\boldsymbol{p},\boldsymbol{p}'} \Big| \langle \mathrm{FS}_c| \int \mathrm{d}^3\boldsymbol{R} \int \mathrm{d}^3\boldsymbol{r}\, \Psi^*_{\boldsymbol{\lambda},\boldsymbol{\alpha}}(\boldsymbol{R},\boldsymbol{r})\, \hat{c}^\dagger_{\boldsymbol{p}'}\, \hat{c}^\dagger_{\boldsymbol{p}}\, \hat{c}_{\boldsymbol{R}+\frac{\boldsymbol{r}}{2}}\, \hat{c}_{\boldsymbol{r}_{\mathrm{L}}} \\
&\qquad\qquad \times \int \mathrm{d}^3\boldsymbol{r}_{\mathrm{L}}\, \delta^{(3)}\Big(\boldsymbol{r}_{\mathrm{L}} - \Big(\boldsymbol{R} - \frac{\boldsymbol{r}}{2} \Big) \Big) |\mathrm{FS}_c\rangle \Big|^2 \\
&= \sum_{\boldsymbol{\lambda},\boldsymbol{\alpha}} \int \mathrm{d}^3\boldsymbol{R} \int \mathrm{d}^3\boldsymbol{R}' \int \mathrm{d}^3\boldsymbol{r} \int \mathrm{d}^3\boldsymbol{r}'\, \Psi^*_{\boldsymbol{\lambda},\boldsymbol{\alpha}}(\boldsymbol{R},\boldsymbol{r}) \Psi_{\boldsymbol{\lambda},\boldsymbol{\alpha}}(\boldsymbol{R}',\boldsymbol{r}') \\
&\qquad \times \langle \mathrm{FS}_c|\, \hat{c}^\dagger_{\boldsymbol{R}'-\frac{\boldsymbol{r}'}{2}}\, \hat{c}^\dagger_{\boldsymbol{R}'+\frac{\boldsymbol{r}'}{2}} \underbrace{\sum_{\boldsymbol{p},\boldsymbol{p}'} \hat{c}_{\boldsymbol{p}}\, \hat{c}_{\boldsymbol{p}'}\, |\mathrm{FS}_c\rangle \langle \mathrm{FS}_c|\, \hat{c}^\dagger_{\boldsymbol{p}'}\, \hat{c}^\dagger_{\boldsymbol{p}}\, \hat{c}_{\boldsymbol{R}+\frac{\boldsymbol{r}}{2}}\, \hat{c}_{\boldsymbol{R}-\frac{\boldsymbol{r}}{2}}}_{=B} |\mathrm{FS}_c\rangle .
\end{aligned} \tag{6.12}$$

[1] Note that the condition imposed by $\delta\big(\omega-(E_{\mathrm{f}}-E_{\mathrm{i}})\big)$ (in Fermi's golden rule) can not be trivially fulfilled within the small frequency interval $\Delta\omega$ for high momentum modes $\boldsymbol{p},\boldsymbol{p}'$ (i.e., high temperatures). Making the extension to the case $T \neq 0$ a nontrivial venture.

This expression can be further simplified using the relation

$$B = \left[\sum_{\boldsymbol{p},\boldsymbol{p}'} \hat{c}_{\boldsymbol{p}}\, \hat{c}_{\boldsymbol{p}'}\, |\mathrm{FS}_c\rangle\, \langle \mathrm{FS}_c|\, \hat{c}^\dagger_{\boldsymbol{p}'}\, \hat{c}^\dagger_{\boldsymbol{p}} \right] \hat{c}_{\boldsymbol{R}+\frac{\boldsymbol{r}}{2}}\, \hat{c}_{\boldsymbol{R}-\frac{\boldsymbol{r}}{2}}\, |\mathrm{FS}_c\rangle = 2\, \hat{c}_{\boldsymbol{R}+\frac{\boldsymbol{r}}{2}}\, \hat{c}_{\boldsymbol{R}-\frac{\boldsymbol{r}}{2}}\, |\mathrm{FS}_c\rangle \ , \tag{6.13}$$

derived in Appendix E.2. It holds for all initial states that are given by a single Fock state (i.e., $|\mathrm{FS}\rangle \to |\mathrm{F}\rangle$, see Appendix E.3). Making use of Eq. (6.13) in Eq. (6.12) we obtain an expression from which the relation between the absorption rate and the pair correlation function

$$n^2 g^{(2)}(\boldsymbol{r}-\boldsymbol{r}') = \langle \hat{c}^\dagger_{\boldsymbol{r}}\, \hat{c}^\dagger_{\boldsymbol{r}'}\, \hat{c}_{\boldsymbol{r}'}\, \hat{c}_{\boldsymbol{r}} \rangle \tag{6.14}$$

already becomes evident, i.e.,

$$\begin{aligned} \bar{A} = 2 \sum_{\boldsymbol{\lambda},\boldsymbol{\alpha}} \int \mathrm{d}^3\boldsymbol{R} \int \mathrm{d}^3\boldsymbol{R}' \int \mathrm{d}^3\boldsymbol{r} \int \mathrm{d}^3\boldsymbol{r}'\, \Psi^*_{\boldsymbol{\lambda},\boldsymbol{\alpha}}(\boldsymbol{R},\boldsymbol{r}) \Psi_{\boldsymbol{\lambda},\boldsymbol{\alpha}}(\boldsymbol{R}',\boldsymbol{r}') \\ \times \langle \mathrm{FS}_c|\, \hat{c}^\dagger_{\boldsymbol{R}'-\frac{\boldsymbol{r}'}{2}}\, \hat{c}^\dagger_{\boldsymbol{R}'+\frac{\boldsymbol{r}'}{2}}\, \hat{c}_{\boldsymbol{R}+\frac{\boldsymbol{r}}{2}}\, \hat{c}_{\boldsymbol{R}-\frac{\boldsymbol{r}}{2}}\, |\mathrm{FS}_c\rangle \ . \end{aligned} \tag{6.15}$$

Depending on the wave functions Ψ the expectation value may reduce directly to the pair correlation function. For instance, approximating the final dimer state as

$$|\mathrm{f}\rangle = \frac{V}{\sqrt{2}} \int \mathrm{d}^3\boldsymbol{R} \int \mathrm{d}^3\boldsymbol{r}\ \delta^{(3)}\big(\boldsymbol{R}-\boldsymbol{R}_\mathrm{C}\big)\, \delta^{(3)}\big(\boldsymbol{r}-\boldsymbol{r}_\mathrm{D}\big)\, d^\dagger_{\boldsymbol{R}-\frac{\boldsymbol{r}}{2}}\, c^\dagger_{\boldsymbol{R}+\frac{\boldsymbol{r}}{2}}\, c_{\boldsymbol{p}}\, c_{\boldsymbol{p}'}\, |\mathrm{FS}_c\rangle \ , \tag{6.16}$$

with fixed positions of the atoms forming the ULRRM-dimer state (see also Appendix E.1) one finds a direct proportionality of $\bar{A} \sim g^{(2)}(r_\mathrm{D})$.

Note that in Eq. (6.15) the concrete shape of the wave functions Ψ characterizing the dimer molecule is not specified. In the following discussion other molecular states (created by photoassociation) could be used as well, as long as their wave functions imply a sufficiently well defined (sharp) binding length. Next we will study how the exact shape of the bound state wave functions impacts the relation between the absorption strength and the pair correlation function.

6.2. ULRRM Dimer in an Ideal Fermi Sea

In the following we show how the specific choice of the ULRRM-dimer wave functions allows to reconstruct $g^{(2)}$ from the absorption spectrum. We now start by taking an explicit form of the center-of-mass wave function while keeping the relative dimer wave function unspecified. In the following we investigate wave functions of the type

$$\begin{aligned} \Psi_{\boldsymbol{K},\boldsymbol{\alpha}}(\boldsymbol{R},\boldsymbol{r}) &= \Phi_{\boldsymbol{K}}(\boldsymbol{R})\, \phi_{\boldsymbol{\alpha}}(\boldsymbol{r}) \ , \\ \Phi_{\boldsymbol{K}}(\boldsymbol{R}) &= \frac{1}{\sqrt{V}}\, \mathrm{e}^{-\mathrm{i}\boldsymbol{K}\cdot\boldsymbol{R}} \ , \end{aligned} \tag{6.17}$$

where $\boldsymbol{K}$ is the center-of-mass momentum of the ULRRM dimer. This allows to perform the integration over one of the center-of-mass coordinates in Eq. (6.15)

$$\begin{aligned}
\bar{A}_{r_\mathrm{D}} &= 2\sum_{\boldsymbol{K},\boldsymbol{\alpha}} \int \mathrm{d}^3\boldsymbol{R} \int \mathrm{d}^3\boldsymbol{R}' \int \mathrm{d}^3\boldsymbol{r} \int \mathrm{d}^3\boldsymbol{r}'\, \phi^*_{\boldsymbol{\alpha}}(\boldsymbol{r})\, \phi_{\boldsymbol{\alpha}}(\boldsymbol{r}')\, \frac{1}{V}\, \mathrm{e}^{\mathrm{i}\boldsymbol{K}\cdot(\boldsymbol{R}'-\boldsymbol{R})} \\
&\qquad \times \langle \mathrm{FS}_c|\, \hat{c}^\dagger_{\boldsymbol{R}'+\frac{\boldsymbol{r}'}{2}}\, \hat{c}^\dagger_{\boldsymbol{R}'-\frac{\boldsymbol{r}'}{2}}\, \hat{c}_{\boldsymbol{R}-\frac{\boldsymbol{r}}{2}}\, \hat{c}_{\boldsymbol{R}+\frac{\boldsymbol{r}}{2}}\, |\mathrm{FS}\rangle \\
&= 2\sum_{\boldsymbol{\alpha}} \int \mathrm{d}^3\boldsymbol{R} \int \mathrm{d}^3\boldsymbol{R}' \int \mathrm{d}^3\boldsymbol{r} \int \mathrm{d}^3\boldsymbol{r}'\, \phi^*_{\boldsymbol{\alpha}}(\boldsymbol{r})\, \phi_{\boldsymbol{\alpha}}(\boldsymbol{r}')\, \delta^{(3)}(\boldsymbol{R}'-\boldsymbol{R}) \\
&\qquad \times \langle \mathrm{FS}_c|\, \hat{c}^\dagger_{\boldsymbol{R}'+\frac{\boldsymbol{r}'}{2}}\, \hat{c}^\dagger_{\boldsymbol{R}'-\frac{\boldsymbol{r}'}{2}}\, \hat{c}_{\boldsymbol{R}-\frac{\boldsymbol{r}}{2}}\, \hat{c}_{\boldsymbol{R}+\frac{\boldsymbol{r}}{2}}\, |\mathrm{FS}\rangle \\
&= 2\sum_{\boldsymbol{\alpha}} \int \mathrm{d}^3\boldsymbol{R} \int \mathrm{d}^3\boldsymbol{r} \int \mathrm{d}^3\boldsymbol{r}'\, \phi^*_{\boldsymbol{\alpha}}(\boldsymbol{r})\, \phi_{\boldsymbol{\alpha}}(\boldsymbol{r}') \\
&\qquad \times \langle \mathrm{FS}_c|\, \hat{c}^\dagger_{\boldsymbol{R}+\frac{\boldsymbol{r}'}{2}}\, \hat{c}^\dagger_{\boldsymbol{R}-\frac{\boldsymbol{r}'}{2}}\, \hat{c}_{\boldsymbol{R}-\frac{\boldsymbol{r}}{2}}\, \hat{c}_{\boldsymbol{R}+\frac{\boldsymbol{r}}{2}}\, |\mathrm{FS}\rangle \ .
\end{aligned} \tag{6.18}$$

For the relative wave functions we choose the ansatz

$$\phi_{\boldsymbol{r}_\mathrm{D} l m}(\boldsymbol{r}) = \chi_{r_\mathrm{D} l}(r)\, Y_{lm}(\theta,\varphi)\ , \tag{6.19}$$

where $\chi_{r_\mathrm{D} l}(r)$ is the radial wave function and $Y_{lm}(\theta,\varphi)$ are the spherical harmonics. The sum over $\boldsymbol{\alpha}$ becomes a sum over l, m and an integral over the solid angle $\Omega_{\boldsymbol{r}_\mathrm{D}}$. We use the notation $\mathrm{d}\Omega_{\boldsymbol{r}} = \sin(\theta)\,\mathrm{d}\theta\,\mathrm{d}\varphi$ and obtain

$$\begin{aligned}
\bar{A}_{r_\mathrm{D}} &= 2\sum_{lm} \int \mathrm{d}\Omega_{\boldsymbol{r}_\mathrm{D}} \int \mathrm{d}^3\boldsymbol{R} \int \mathrm{d}^3\boldsymbol{r} \int \mathrm{d}^3\boldsymbol{r}'\, \chi^*_{r_\mathrm{D} l}(r)\, Y^*_{lm}(\theta,\varphi)\ \ \chi_{r_\mathrm{D} l}(r')\, Y_{lm}(\theta',\varphi') \\
&\qquad \times \langle \mathrm{FS}_c|\, \hat{c}^\dagger_{\boldsymbol{R}+\frac{\boldsymbol{r}'}{2}}\, \hat{c}^\dagger_{\boldsymbol{R}-\frac{\boldsymbol{r}'}{2}}\, \hat{c}_{\boldsymbol{R}-\frac{\boldsymbol{r}}{2}}\, \hat{c}_{\boldsymbol{R}+\frac{\boldsymbol{r}}{2}}\, |\mathrm{FS}\rangle \\
&\approx 2 \int \mathrm{d}\Omega_{\boldsymbol{r}_\mathrm{D}} \int \mathrm{d}^3\boldsymbol{R} \int_0^\infty \mathrm{d}r \int_0^\infty \mathrm{d}r'\, r^2 r'^2\, \chi^*_{r_\mathrm{D}}(r)\, \chi_{r_\mathrm{D}}(r') \int \mathrm{d}\Omega_{\boldsymbol{r}} \int \mathrm{d}\Omega_{\boldsymbol{r}'} \\
&\qquad \times \sum_{lm} Y^*_{lm}(\theta,\varphi)\, Y_{lm}(\theta',\varphi')\, \langle \mathrm{FS}_c|\, \hat{c}^\dagger_{\boldsymbol{R}+\frac{\boldsymbol{r}'}{2}}\, \hat{c}^\dagger_{\boldsymbol{R}-\frac{\boldsymbol{r}'}{2}}\, \hat{c}_{\boldsymbol{R}-\frac{\boldsymbol{r}}{2}}\, \hat{c}_{\boldsymbol{R}+\frac{\boldsymbol{r}}{2}}\, |\mathrm{FS}\rangle \ .
\end{aligned} \tag{6.20}$$

Here we have assumed that the Rydberg atom is large in comparison to the range of the centrifugal potential, i.e., that the energies of the centrifugal barrier is sufficiently small compared to the ULRRM potential at the dimer binding length r_D

$$\frac{\hbar^2}{2\mu}\frac{l(l+1)}{r_\mathrm{D}^2} \ll |V(r_\mathrm{D})|\ . \tag{6.21}$$

In this limit the radial ULRRM-dimer wave functions do not depend on the angular momentum and we can make use of the identity

$$\sum_{l=0}^{\infty}\sum_{m=-l}^{l} Y_{lm}^{*}(\theta,\varphi)\,Y_{lm}(\theta',\varphi') = \delta(\varphi-\varphi')\,\delta(\cos\theta-\cos\theta')\ , \tag{6.22}$$

allowing to perform the integration over $\mathrm{d}\Omega_{\boldsymbol{r}'}$

$$\begin{aligned}\bar{A}_{r_\mathrm{D}} = 2\int \mathrm{d}\Omega_{\boldsymbol{r}_\mathrm{D}}\int \mathrm{d}\Omega_{\boldsymbol{r}}\int \mathrm{d}^3\boldsymbol{R}\int_0^\infty \mathrm{d}r\int_0^\infty \mathrm{d}r'\, r^2 r'^2\,\chi_{r_\mathrm{D}}^{*}(r)\,\chi_{r_\mathrm{D}}(r') \\ \times\langle \mathrm{FS}_c|\,\hat{c}^{\dagger}_{\boldsymbol{R}+\frac{r'\mathbf{e}_r}{2}}\,\hat{c}^{\dagger}_{\boldsymbol{R}-\frac{r'\mathbf{e}_r}{2}}\,\hat{c}_{\boldsymbol{R}-\frac{\boldsymbol{r}}{2}}\,\hat{c}_{\boldsymbol{R}+\frac{\boldsymbol{r}}{2}}\,|\mathrm{FS}\rangle\ .\end{aligned} \tag{6.23}$$

This expression can be further simplified as shown in Appendix E.4

$$\bar{A}_{r_\mathrm{D}} = 2(4\pi)^2\,V\int_0^\infty \mathrm{d}r\int_0^\infty \mathrm{d}r'\, r^2 r'^2\,\chi_{r_\mathrm{D}}^{*}(r)\ \chi_{r_\mathrm{D}}(r')\,\xi(r,r')\ , \tag{6.24}$$

where the function $\xi(r,r')$ takes the form

$$\begin{aligned}\xi(r,r') = \left(\frac{k_\mathrm{F}^3}{2\pi^2}\right)^2\left[h\left(k_\mathrm{F}\frac{r-r'}{2}\right)^2 - h\left(k_\mathrm{F}\frac{r+r'}{2}\right)^2\right]\ , \\ \text{with:}\quad h(x) = \frac{\sin(x)-x\,\cos(x)}{x^3}\ .\end{aligned} \tag{6.25}$$

Now we turn to the radial wave functions $\chi_{r_\mathrm{D}}(r')$. The deepest ULRRM-dimer bound state is situated in the outer most well of the ULRRM potential at distance r_D (see Fig. 5.2b). Since the potential well is approximately harmonic we first investigate an approximation of the ULRRM dimer state in form of a radial Gaussain wave function

$$\begin{aligned}\chi_{r_\mathrm{D}}(r) &= \frac{u_{r_\mathrm{D}}(r)}{r}\ , \\ u_{r_\mathrm{D}}(r) &= \frac{1}{(2\pi\sigma_{r_\mathrm{D}}^2)^{\frac{1}{4}}}\,\mathrm{e}^{-\frac{(r-r_\mathrm{D})^2}{4\sigma_{r_\mathrm{D}}^2}}\ .\end{aligned} \tag{6.26}$$

To obtain some analytical insight, before we turn to the numerical evaluation of Eq. (6.24), we consider the limiting case of small σ_{r_D} (see Fig. 6.2). In this case we may replace

$$u_\nu(r) = \frac{1}{(2\pi\sigma_{r_\mathrm{D}}^2)^{\frac{1}{4}}}\,\mathrm{e}^{-\frac{(r-r_\mathrm{D})^2}{4\sigma_{r_\mathrm{D}}^2}} \underset{\sigma_{r_\mathrm{D}}\to\sigma=0}{\longrightarrow} (2\pi\sigma^2)^{\frac{1}{4}}\,\delta(r-r_\mathrm{D})\ . \tag{6.27}$$

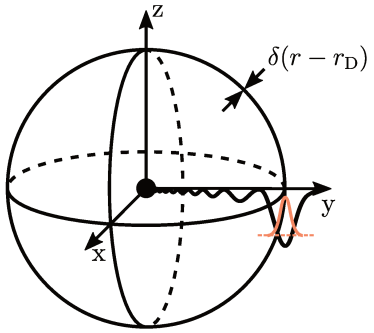

Figure 6.2.: Illustration of the limiting case of a dimer ULRRM wave functions with zero-radial-width wave functions.

This results in an absorption response which is directly proportional to $g^2(r_D)$ as can be seen from an evaluation of

$$\begin{aligned}\bar{A}_{r_D} &= 2V\,(4\pi)^2\sqrt{2\pi}\sigma \int_0^\infty \mathrm{d}r \int_0^\infty \mathrm{d}r'\, rr'\,\delta(r - r_D)\,\delta(r' - r_D)\,\xi(r, r') \\ &= 2V\,(4\pi)^2\sqrt{2\pi}\sigma\, r_D^2 \left(\frac{k_F^3}{2\pi^2}\right)^2 \left(h(0)^2 - h(k_F r_D)^2\right) \\ &= 8\,V\,\frac{1}{\pi^2}\sqrt{2\pi}\sigma\, r_D^2 k_F^6 \left(h(0)^2 - h(k_F\, r_D)^2\right)\ .\end{aligned} \tag{6.28}$$

First we determine the value of $h(0)$ using L'Hôspital's rule

$$\lim_{r\to 0} h(r) = \lim_{r\to 0} \frac{\sin(k_F r) - k_F r\,\cos(k_F r)}{(k_F r)^3} = \lim_{r\to 0} \frac{k_F\,\cos(k_F r)}{3\,k_F} = \frac{1}{3}\ . \tag{6.29}$$

Identifying $g^{(2)}(r_D) = 1 - (3\,h(k_F\,r_D))^2$ (see Appendix E.5) Eq. (6.28) yields the dimer absorption strength in the δ-shell limiting case

$$\bar{A}_{r_D} = 8\,V\sqrt{2\pi}\sigma\,4\,n^2\,r_D^2\,g^{(2)}(r_D)\ . \tag{6.30}$$

This shows the direct relation between the dimer absorption line strength and the pair correlation function $g^{(2)}(r_D)$. As we show by a comparison with the results of a direct numerical evaluation of Eq. (6.24) using finite-width Gaussian wave functions in this turns out to be a remarkably good approximation. The comparison is shown in Fig. 6.3, where we have normalized the numerical results by the prefactor obtained in the case of zero-width Gaussian wave functions. Specifically, we have used here a Fermi momentum motivated by typical experimental settings

$$k_F = (6\pi^2 n)^{\frac{1}{3}} = \left(6\pi^2\, 3\times 10^{13}\frac{1}{\mathrm{cm}^3}\right)^{\frac{1}{3}} \approx 6.4\times 10^{-4}\frac{1}{a_0}\ . \tag{6.31}$$

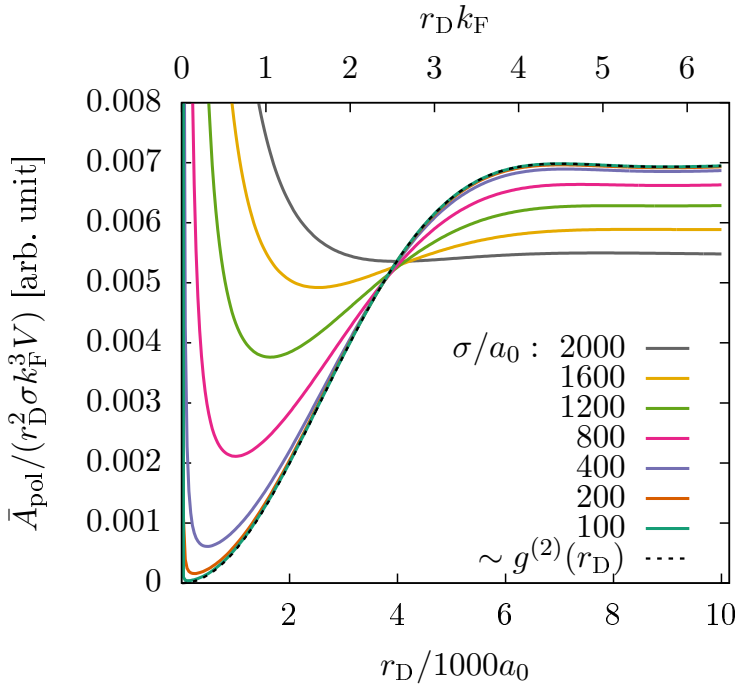

Figure 6.3.: Normalized absorption strength obtained from a numerical evaluation of Eq. (6.24) using Gaussian radial wave functions for different values σ. Here we renamed $\bar{A}_{r_D} \mapsto \bar{A}_{pol}$. A fit of the fermionic zero-temperature pair correlation function, i.e., $f(r_D) = \text{const.} \times g^{(2)}(r_D)$ to the results for a Gaussian radial wave function with $\sigma = 100\, a_0$ is shown as a dashed line.

The comparison of the normalized absorption signal with $g^{(2)}(r_D)$ shows that the pair correlation function can indeed be reconstructed from the Rydberg absorption spectra for sufficiently narrow radial wave functions. Figure 6.4 shows the width of Gaussian fits (see Fig. 5.2) to the ULRRM wave functions for different principle quantum numbers $n^* = n - \delta$, suggesting that Rydberg excitations up to large principal values of $n^* \lesssim 80$ are still sufficiently narrow to act as a probe for quantum correlations in ultracold gases. The ULRRM-dimer binding length (Rydberg radius) r_D is related to n by $r_D \approx n^{*2} a_0$. The effect that Rydberg excitations with smaller n^* have smaller Rydberg radii and narrower radial ULRRM-dimer wave functions results in an increased sensitivity of Rydberg excitations as probe of correlations closer to the Rydberg core. This additionally supports the usage of Rydberg excitations as probe of the fermionic pair correlation function as the relative change of the local density is bigger at small distances where the sensitivity of the Rydberg probe is enhanced.

In the specific experimental setting [P1] we found a scaling of the integrated dimer response deviating from $g^{(2)}$ by binding length dependent prefactor (e.g., $\bar{A}_{r_D} \sim n^2 r_D^2 g^{(2)}(r_D)$ in Eq. (6.30)). This prefactor turns out to be the same for ULRRMs formed by atoms with equal spin (where the respective creation and annihilation operators anticommute)

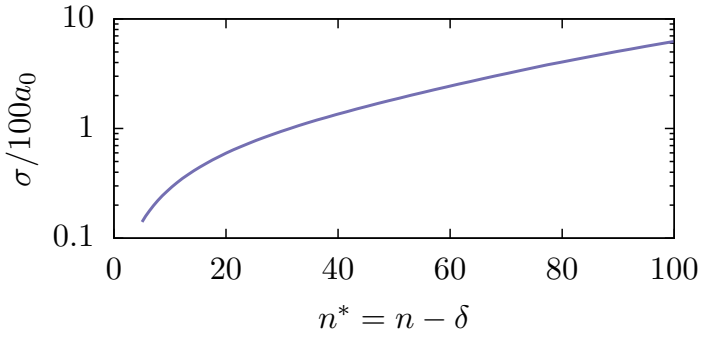

Figure 6.4.: Gaussian width σ obtained trough Gaussian fits to the radial ULRRM wave functions $\chi(r)$ with respect to the principal quantum number of the Rydberg excitation.

and for ULRRMs made out of atoms with different spins (commuting creation and annihilation operators). As a result the ratio of the absorption signals obtained in these two cases allows to, again, exactly reconstruct $g^{(2)}$.

Following this discussion, we now repeat the calculation of the ULRRM-dimer absorption strength for an initial state that is a two-component Fermi gas and an ULRRM final state that consists of two distinguishable fermions, i.e.,

$$\begin{aligned} |\mathrm{i}\rangle &= |\mathrm{FS}_\uparrow\rangle \otimes |\mathrm{FS}_\downarrow\rangle \ , \\ |\mathrm{f}\rangle &= |\mathrm{f}(\boldsymbol{\lambda}, \boldsymbol{\alpha}, \boldsymbol{p}, \boldsymbol{p}')\rangle \\ &= \int \mathrm{d}^3\boldsymbol{R} \int \mathrm{d}^3\boldsymbol{r}\, \Psi_{\boldsymbol{\lambda},\boldsymbol{\alpha}}(\boldsymbol{R}, \boldsymbol{r})\, \hat{d}^\dagger_{\uparrow \boldsymbol{R}-\frac{\boldsymbol{r}}{2}}\, \hat{c}^\dagger_{\downarrow \boldsymbol{R}+\frac{\boldsymbol{r}}{2}}\, \hat{c}_{\uparrow \boldsymbol{p}}\, \hat{c}_{\downarrow \boldsymbol{p}'}\, |\mathrm{FS}_\uparrow\rangle \otimes |\mathrm{FS}_\downarrow\rangle \ , \end{aligned} \tag{6.32}$$

which results in (for details see Appendix E.6)

$$\bar{A}_{\mathrm{unpol}} = \frac{4}{\pi^2}\, V \int_0^\infty \mathrm{d}r \int_0^\infty \mathrm{d}r'\, r r'\, u^*_{\nu r_\mathrm{D}}(r)\, u_{\nu r_\mathrm{D}}(r')\, k_\mathrm{F}^6\, h\Big(k_\mathrm{F}\, \frac{r - r'}{2}\Big)^2 \ . \tag{6.33}$$

This allows to numerically evaluate the ratio $\bar{A}_{\mathrm{pol}}/\bar{A}_{\mathrm{unpol}}$ where factors other than the pair correlation function $g^{(2)}$ cancel. In Fig. 6.5 we show the result of the normalized ULRRM-dimer absorption strength obtained from a numerical evaluation of Eqs. (6.24) and (6.33) using the ULRRM wave functions obtained from the analysis of the radial Schrödinger equation in Eq. (5.10) and compare the results to the signal obtained from Gaussian radial wave functions. We find an excellent agreement of the predicted normalized ULRRM-dimer absorption strength and the fermionic pair correlation function.

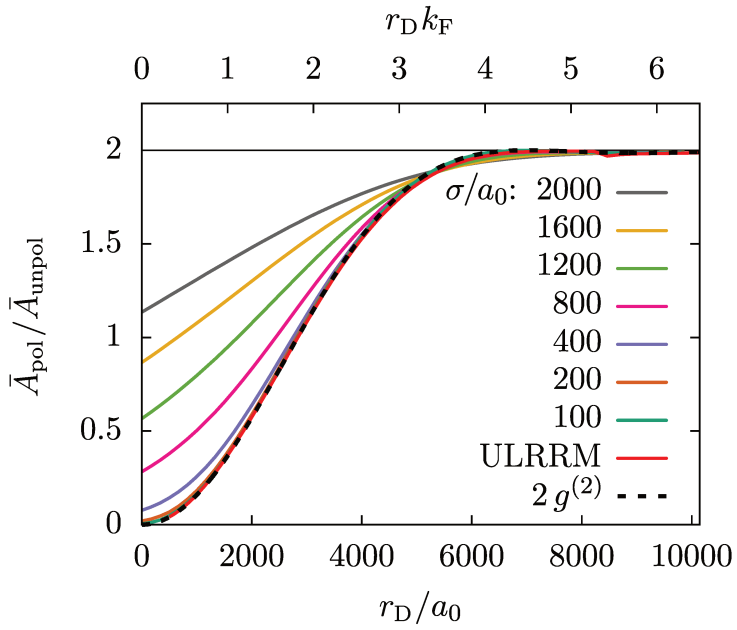

Figure 6.5.: Normalized integrated absorption signals for spin-polarized ULRRMs by the signal for unpolarized ULRRMs, obtained from Eqs. (6.24) and (6.33). The ratio $\bar{A}_{\mathrm{pol}}/\bar{A}_{\mathrm{unpol}}$ converges to $g^{(2)}(r_{\mathrm{D}})$, shown as dashed line, for narrow radial wave functions. The red line marks the result obtained using the actual ^{87}Sr ULRRM-dimer wave functions obtained from solving the Schrödinger equation (see Eq. (5.10)).

6.3. Summary

In this chapter we have shown how Rydberg spectroscopy can be used to probe correlations in ultracold quantum gases at the example of a non-interacting Fermi gas. In our recent work [P4] we also showed that this principle works, e.g., for the detection of Fermi polarons, suggesting a much more general applicability of this idea. Nonetheless, the general relation between the correlations within an arbitrary quantum state and the Rydberg absorption spectrum remains an open question. In Appendix F we provide details on the application of the ansatz Eq. (6.8) on an arbitrarily correlated fermionic initial state (i.e., a superposition state of Fock states $|\mathrm{F}\rangle$)

$$|\mathrm{i}\rangle = \sum_{\mathrm{F}} \alpha_{\mathrm{F}} \, |\mathrm{F}\rangle \otimes |0\rangle_d \ , \tag{6.34}$$

with

$$|\mathrm{F}\rangle = \prod_{i=1}^{\infty} \left(\hat{c}^{\dagger}_{\boldsymbol{k}_i}\right)^{n_i^{\mathrm{F}}} |0\rangle = |n_1^{\mathrm{F}}, n_2^{\mathrm{F}}, \ldots, n_i^{\mathrm{F}}, \ldots, n_{\infty}^{\mathrm{F}}\rangle \ , \tag{6.35}$$

where

$$\sum_{i=1}^{\infty} n_i^{\mathrm{F}} = N \quad , \forall \mathrm{F} \; . \tag{6.36}$$

The possibility to use optical tweezers [108–110] to fix the position of one species of atoms that can be later excited to a Rydberg state should allow for the measurement of the local density around the Rydberg excitation in a quantum gas (see our work [P4] for the case of infinitely heavy Rydberg impurities). Further, Rydberg excitations as probe of quantum matter could make it possible to probe ferromagnetic domain walls [111–114] that possibly form in strongly interacting Fermi gases in the context of stoner ferromagnetism. The presence of such domains would results in a suppression of ULRRM formation at their boundaries. In the same way Rydberg excitations could provide a probe for domain walls in a phase separated state of Bose–Fermi mixtures [115] or spin-imbalanced Fermi gases [116].

Probing correlations of interacting many-body systems presents a major experimental challenge and was so far only possible using standard methods in restricted settings such as absorption imaging of ultracold atoms in optical lattices. Hence, the general study of non-equilibrium quantum dynamics in strongly correlated systems depends upon the development of new methods that allow for spacial and time-resolved sensing of the quantum state. The presented method of Rydberg excitation microscopy where Rydberg excitations are used to probe quantum states addresses this challenge. In the next chapter we present two scenarios – a gas of Feshbach molecules and the formation of a polaron cloud around a quantum impurity in ultracold atoms – where Rydberg excitations allow to detect correlations and local densities of strongly correlated quantum states.

7. Applications to Experiments

In this chapter we study examples of how Rydberg excitations can be used as probe of quantum matter. First we investigate a dilute gas of weakly bound Feshbach halo molecules. Here the excitation of one of the atoms within the molecule into a Rydberg state allows to detect the characteristic Feshbach-molecule wave function. Then we turn to the Fermi-polaron problem and propose how the excitation of ULRRMs, containing the impurity as Rydberg atom, can be used to detect the density of the polaron cloud around an impurity in a Fermi gas.

7.1. Rydberg Excitations as Probe of Feshbach Molecules

As seen in Chapter 6, the resonant creation of Rydberg excitations at the ULRRM-dimer frequency probes the probability of finding two atoms in a certain distance from each other. Hence this scheme of probing correlations can be used for the detection of molecular states with characteristic binding behavior. Below we discuss the example of a dilute gas of Feshbach halo dimers [117] whose individual relative wave functions are described by

$$\phi_{lm}^{\mathrm{FM}}(\boldsymbol{r}) = \sqrt{\frac{2}{a}}\,\frac{\mathrm{e}^{-\frac{r}{a}}}{r}\,Y_{lm}(\Omega_{\boldsymbol{r}})\ , \tag{7.1}$$

where a is the s-wave scattering length[1], and $l = 0$ for such weakly bound states. Out of the two atoms one is excited into into a Rydberg state which can then form an ULRRM dimer with the second atom. We will now show that the respective absorption strength allows to reconstruct the Feshbach-molecule's wave function.

We assume the system to be initially prepared in gas of Feshbach-dimers with wave-function Eq. (7.1) for l=0. Further we assume the gas of Feshbach molecules to be dilute, such that the overlap of two halo dimers is negligible and also the typical distance between two molecules is large compared to the ULRRM binding length used to probe the quantum gas. This ensures that the contribution of the ULRRM absorption signal of molecules formed from atoms belonging to different Feshbach molecules can be neglected. Due to the conservation of angular momentum the ULRRM-dimer state has to be a $l = 0$ state. The absorption strength of a resonant excitation of Rydberg atoms at the ULRRM-dimer frequency is then proportional to the Franck-Condon overlap of

[1]Here the scattering length can be tuned using Feshbach resonances as described in Section 2.2.

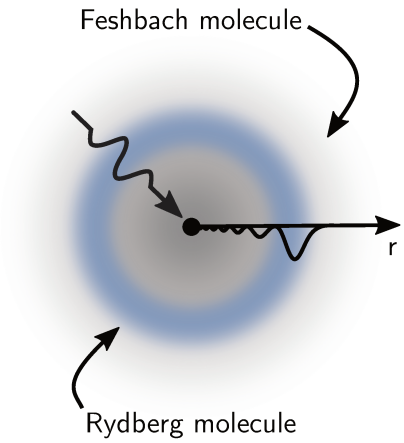

Figure 7.1.: Illustration of the excitation of an atom bound in a Feshbach molecule (gray) with an exponential decaying tail into a Rydberg state that forms an ULRRM with the second atom from the Feshbach molecule.

the Feshbach-molecule initial state and the Rydberg-molecule final state wave functions (see Fig. 7.1)

$$\begin{aligned}\bar{A} &= \left| \int \mathrm{d}\boldsymbol{r}\, \phi^*_{\mathrm{RM}}(\boldsymbol{r}) \phi_{\mathrm{FM}}(\boldsymbol{r}) \right|^2 \\ &= (2\pi)^3 \frac{2}{a} \left| \int_0^\infty \mathrm{d}r\, r\, \chi^*_{\nu\, l=0}(r)\, \mathrm{e}^{-\frac{r}{a}} \right|^2 \quad .\end{aligned} \tag{7.2}$$

We again choose a Gaussian to approximate the radial ULRRM-dimer wave functions

$$\begin{aligned}\chi_{r_\mathrm{D}}(r) &= \frac{u_{r_\mathrm{D}}(r)}{r} \ , \\ u_{r_\mathrm{D}}(r) &= \frac{1}{(2\pi\sigma^2_{r_\mathrm{D}})^{\frac{1}{4}}}\, \mathrm{e}^{-\frac{(r-r_\mathrm{D})^2}{4\sigma^2_{r_\mathrm{D}}}} \ ,\end{aligned} \tag{7.3}$$

and consider the limiting case of small σ_{r_D} (see Fig. 6.2). Here we may again replace the Gaussian by a δ-function

$$u_\nu(r) = \frac{1}{(2\pi\sigma^2_{r_\mathrm{D}})^{\frac{1}{4}}}\, \mathrm{e}^{-\frac{(r-r_\mathrm{D})^2}{4\sigma^2_{r_\mathrm{D}}}} \underset{\sigma_{r_\mathrm{D}} \to \sigma = 0}{\longrightarrow} (2\pi\sigma^2)^{\frac{1}{4}}\, \delta(r - r_\mathrm{D}) \ . \tag{7.4}$$

This allows us to rewrite the ULRRM-dimer absorption strength as

$$\begin{aligned}\bar{A} &= \frac{2}{a} (2\pi)^3 (2\pi\sigma^2)^{\frac{1}{2}} \left| \int_0^\infty \mathrm{d}r\, \delta(r - r_\mathrm{D})\, \mathrm{e}^{-\frac{r}{a}} \right|^2 \\ &= \frac{2}{a} (2\pi)^3 \sqrt{2\pi\sigma^2}\, \mathrm{e}^{-2\frac{r_\mathrm{D}}{a}} \sim n^2\, r_\mathrm{D}^2\, g^{(2)}(r_\mathrm{D}) \ ,\end{aligned} \tag{7.5}$$

where we used that the pair correlation function of two particles described by a relative two particle wave function $\phi(\boldsymbol{r})$ is given by the corresponding probability density $g^{(2)}(|\boldsymbol{r}|) \sim |\phi(\boldsymbol{r})|^2$ (see Appendix G). We find the same scaling of $\bar{A} \sim r_{\mathrm{D}}^2\, g^{(2)}(r_{\mathrm{D}})$ as in the scenario of an ULRRM dimer excited in a Fermi sea (see Eq. (6.30)).

This analysis shows that Rydberg spectroscopic measurements of a dilute gas of Feshbach molecules allow to extract information about the wave function of the Feshbach halo molecules and thus the scattering length a of the interactions of the ultracold atoms.

7.2. Towards the Rydberg Spectroscopic Detection of a Polaron Cloud

Following our recent publication [P4] we here briefly discuss how Rydberg excitation spectroscopy can be used to measure the density profile of a polaron cloud around an immobile impurity when the impurity atom itself can be excited into a Rydberg state (see Fig. 7.2). In an experimental setting this can be approximated by using an ultracold quantum gas comprising two different atomic species, where one, the minority species, is heavy compared to the other. The Hamiltonian describing the system reads

$$H_{\mathrm{imp}} = \sum_{\boldsymbol{k}} \epsilon_{\boldsymbol{k}} \hat{c}_{\boldsymbol{k}}^\dagger \hat{c}_{\boldsymbol{k}} + \sum_{\boldsymbol{k},\sigma} \omega_{\boldsymbol{k}} \hat{d}_{\boldsymbol{k},\sigma}^\dagger \hat{d}_{\boldsymbol{k},\sigma} + \sum_{\sigma} \int \mathrm{d}^3\boldsymbol{r} \int \mathrm{d}^3\boldsymbol{r}'\; \hat{d}_{\boldsymbol{r},\sigma}^\dagger \hat{d}_{\boldsymbol{r},\sigma} V_\sigma(\boldsymbol{r}' - \boldsymbol{r}) \hat{c}_{\boldsymbol{r}'}^\dagger \hat{c}_{\boldsymbol{r}'} \,. \tag{7.6}$$

Here the operators $\hat{c}_{\boldsymbol{k}}^\dagger$ and $\hat{d}_{\boldsymbol{k}}^\dagger$ create fermions and impurities respectively in the momentum mode $\boldsymbol{k}$. The index $\sigma \in \{1, R\}$ in turn characterizes the state of the impurity, $\sigma = 1$ corresponds to an impurity that interacts via contact interactions $V_1(\boldsymbol{r})$ with the bath atoms and $\sigma = R$ corresponds to an impurity in a Rydberg state which interactions with the surrounding atoms as described by the ULRRM potential $V_R(\boldsymbol{r}) = V_{\mathrm{ULRRM}}(\boldsymbol{r})$ given in Eq. (5.7). The Hamiltonian is not quadratic in creation and annihilation operators, as interactions between the impurity ($\hat{d}$-operators) and the Fermions ($\hat{c}$-operators) appear. For finite mass impurities this prohibits the application of a direct functional determinant approach [24] as a tool to compute the respective absorption spectra. However, in the immobile single impurity limit the Hamiltonian Eq. (7.6) does become quadratic

$$H_{\mathrm{inf}} = \sum_{\boldsymbol{k}} \epsilon_{\boldsymbol{k}}\, \hat{c}_{\boldsymbol{k}}^\dagger \hat{c}_{\boldsymbol{k}} + \int \mathrm{d}^3\boldsymbol{r}\, V_\sigma(\boldsymbol{r})\, \hat{c}_{\boldsymbol{r}}^\dagger \hat{c}_{\boldsymbol{r}} \,, \tag{7.7}$$

recognizing that the impurity position is a conserved quantity and thus may be assumed, e.g., to be placed at the origin of the coordinate system.

In [P4] we have shown how one can extract the local density of the polaron cloud around the impurity from the line strength of the ULRRM-dimer peak in the absorption spectrum using a functional determinant approach [24]. To this end, one calculates the Rydberg excitation spectrum when the impurity itself is excited in a Rydberg state.

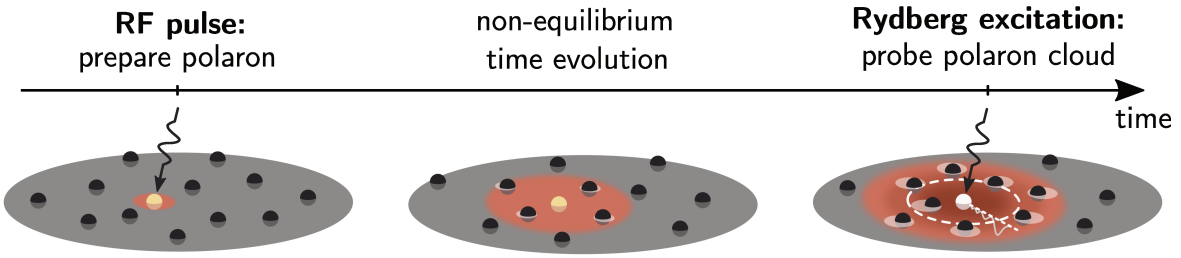

Figure 7.2.: Illustration of the excitation of an impurity into a Rydberg state that allows to probe the polaron cloud (the figures show a cross section of a three-dimensional cloud). First the impurity is brought into its interacting state. As a consequence the polaron is formed. Neighboring atoms are pulled towards the impurity (in case of the attractive polaron). In a second step (here after the polaron is fully formed) the impurity atom is excited into a Rydberg state. The ULRRM formation probes the polaron cloud.

The relevant functional determinant formula can be derived by considering the finite temperature absorption spectrum of a Rydberg impurity which is given by Fermi's golden rule

$$A(\omega) = \sum_{\mathrm{f,\,i}} \left| \langle \mathrm{f}| \hat{V}_{\mathrm{L}} |\mathrm{i}\rangle \right|^2 \frac{\mathrm{e}^{-\beta(E_\mathrm{i}-\mu N_\mathrm{i})}}{\mathrm{tr}\left(\mathrm{e}^{-\beta(\hat{H}_0-\mu\hat{N})}\right)} \delta\big(\omega - (E_\mathrm{f} - E_\mathrm{i})\big) \ . \tag{7.8}$$

By rewriting $\delta(\omega) = 1/2\pi \int_{-\infty}^{\infty} \mathrm{d}t \exp(-\mathrm{i}\omega t)$ we obtain

$$\begin{aligned} A(\omega) &= \frac{1}{2\pi} \int_{-\infty}^{\infty} \mathrm{d}t \sum_{\mathrm{f,\,i}} \langle \mathrm{i}| \hat{V}_{\mathrm{L}}^\dagger |\mathrm{f}\rangle \langle \mathrm{f}| \hat{V}_{\mathrm{L}} |\mathrm{i}\rangle \ \frac{\mathrm{e}^{-\beta(E_\mathrm{i}-\mu N_\mathrm{i})}}{\mathrm{tr}\left(\mathrm{e}^{-\beta(\hat{H}_0-\mu\hat{N})}\right)} \mathrm{e}^{-\mathrm{i}\omega t} \, \mathrm{e}^{\mathrm{i}E_\mathrm{f} t} \, \mathrm{e}^{-\mathrm{i}E_\mathrm{i} t} \\ &= \frac{1}{2\pi} \frac{1}{\mathrm{tr}\left(\mathrm{e}^{-\beta(\hat{H}_0-\mu\hat{N})}\right)} \int_{-\infty}^{\infty} \mathrm{d}t \sum_{\mathrm{i}} \langle \mathrm{i}| \, \mathrm{e}^{-\mathrm{i}\hat{H}_0 t} \, \hat{V}_{\mathrm{L}}^\dagger \, \mathrm{e}^{\mathrm{i}\hat{H} t} \hat{V}_{\mathrm{L}} \, \mathrm{e}^{-\beta(\hat{H}_0-\mu\hat{N})} \, |\mathrm{i}\rangle \ \mathrm{e}^{-\mathrm{i}\omega t} \\ &= \frac{1}{2\pi} \int_{-\infty}^{\infty} \mathrm{d}t \, S(t) \, \mathrm{e}^{-\mathrm{i}\omega t} \ , \end{aligned} \tag{7.9}$$

with

$$S(t) = \frac{\mathrm{tr}\left(\mathrm{e}^{-\mathrm{i}\hat{H}_0 t} \, \hat{V}_{\mathrm{L}}^\dagger \, \mathrm{e}^{\mathrm{i}\hat{H} t} \hat{V}_{\mathrm{L}} \, \mathrm{e}^{-\beta(\hat{H}_0-\mu\hat{N})}\right)}{\mathrm{tr}\left(\mathrm{e}^{-\beta(\hat{H}_0-\mu\hat{N})}\right)} \ . \tag{7.10}$$

In Appendix B we follow the derivation of the Levitov-Klich formula [118, 119] and sketch how the Loschmidt echo

$$S(t) = \det\left(1 - \hat{n} + \hat{n} \, \mathrm{e}^{-\mathrm{i}\hat{h}_0 t} \, \mathrm{e}^{\mathrm{i}\hat{h} t}\right) \tag{7.11}$$

can be treated effectively numerically. In

$$\hat{B} = \left(1 - \hat{n} + \hat{n}\mathrm{e}^{-\mathrm{i}\hat{h}_0 t}\mathrm{e}^{\mathrm{i}\hat{h}t}\right) \tag{7.12}$$

the operators are single particle operators as, e.g., $\hat{h}_0 = \hat{\boldsymbol{k}}^2/2m$ while

$$\hat{n} = \frac{1}{\mathrm{e}^{\beta(\hat{h}_0-\mu)}+1} \ . \tag{7.13}$$

The interacting single particle Hamiltonian is given by $\hat{h} = \hat{\boldsymbol{k}}^2/2m + V(\hat{\boldsymbol{r}})$. Using the eigenbasis of $\hat{h}_0$ the representation of $\hat{B}$ is block diagonal as each set of $2l+1$ states with fixed values of l and m forms an orthonormal basis in an invariant subspace of the Hilbert space. With the respective eigenstates of the single particle Hamiltonians

$$\begin{aligned} \hat{h}_0 \left|nlm\right\rangle &= \varepsilon_{nlm} \left|nlm\right\rangle \ , \\ \hat{h} \left|\nu lm\right\rangle &= \omega_{\nu lm} \left|\nu lm\right\rangle \ , \end{aligned} \tag{7.14}$$

one finds (see Appendix B)

$$\begin{aligned} \left\langle n'l'm'\right| \hat{B} \left|nlm\right\rangle &= \delta_{nn'}\delta_{ll'}\delta_{mm'} - \delta_{nn'}\delta_{ll'}\delta_{mm'} n(\varepsilon_{nlm}) + \underbrace{\left\langle n'l'm'\right| \hat{n}\mathrm{e}^{-\mathrm{i}\hat{h}_0 t}\mathrm{e}^{\mathrm{i}\hat{h}t} \left|nlm\right\rangle}_{(*)} \\ (*) &= n(\varepsilon_{n'lm})\, \mathrm{e}^{-\mathrm{i}\varepsilon_{n'lm}t}\delta_{ll'}\delta_{mm'} \sum_{\nu} \mathrm{e}^{\mathrm{i}\omega_{\nu lm}t} \left\langle n'lm|\nu\, lm\right\rangle \left\langle \nu lm|nlm\right\rangle \end{aligned} \tag{7.15}$$

and

$$\det(\hat{B}) = \prod_{lm} \det(\hat{B}_{lm}) = \prod_{l} \det(\hat{B}_l)^{2l+1} \ . \tag{7.16}$$

If one uses the eigenstates of the polaronic problem as states $|nlm\rangle$ and the ones of the Rydberg problem as interacting states $|\nu lm\rangle$ one is able to calculate the ULRRM-dimer absorption strength, when the impurity in the center of the polaron cloud is excited to a Rydberg state. Performing a detailed analysis of absoprtion spectra in [P4] we show that the ratio of line strength of the ULRRM-dimer peak in the polaron cloud and a background gas that is not interacting with the impurity (i.e., for turned off impurity-bath interactions, which can be achieved in an experimental setting using Feshbach resonances) precisely follows the density of the polaron cloud.

Indeed this finding can also directly be understood in terms of the method presented in Chapter 6. As we have seen in Eq. (6.30) the ULRRM-dimer absorption strength is directly proportional to the pair correlation function $g^{(2)}$. Applying this to the single immobile impurity limit one directly sees that this leads to a measure of the local density of the environment of the impurity

$$n_c(\boldsymbol{r}) \sim \left\langle \mathrm{i}\right| \hat{d}_{\boldsymbol{0}}^\dagger \hat{d}_{\boldsymbol{0}} \hat{c}_{\boldsymbol{r}}^\dagger \hat{c}_{\boldsymbol{r}} \left|\mathrm{i}\right\rangle \ , \tag{7.17}$$

where, in this case, $\hat{d}_{\boldsymbol{0}}^\dagger \hat{d}_{\boldsymbol{0}}$ probes the presence of an immobile impurity atom in the center of the polaron cloud.

7.3. Summary

In this chapter we have seen how Rydberg excitations can be used to probe correlated quantum states at the example of two systems that can be investigated in experiments. In the context of a gas of Feshbach molecules Rydberg spectroscopy allows to investigate the molecular wave functions which gives access to the scattering length of the ultracold atoms, while Rydberg excitations of impurity atoms in an ultracold quantum gases provide a direct probe of the polaron cloud. These applications show the versatility of Rydberg excitations as probe of ultracold quantum matter.

8. Detour: Semiclassical Description of Rydberg Excitations in a BEC

In this chapter we shift gears and turn to investigating a semiclassical description of Rydberg excitations in a BEC. This discussion is motivated by the observation that at large gas densities the absorption spectra of Rydberg impurities in BECs are well described by a classical Monte Carlo sampling of point-like particles in a ULRRM potential that is quenched into the BEC [101]. We first investigate the statistical distribution of Rydberg excitations within a BEC. Then we turn to the analysis of the dynamics of atoms around a Rydberg impurity in a BEC of ^{87}Rb atoms.

8.1. Rydberg Excitation Positions in a BEC

The following section is part of our publication [P2]. For the description of Rydberg excitations in a BEC the first crucial point is to understand where inside of a BEC Rydberg atoms are created by the absorption of photons of a specific energy. Here we present a semiclassical analysis of this problem. To obtain the spatial distribution of Rydberg excitations within a harmonically confined BEC we model the excitation process by drawing from different probability distributions that describe the excitation of a Rydberg atom from a harmonically trapped BEC by a Gaussian laser beam.

We start by generating clouds of point-like particles with a distribution function matching the Thomas-Fermi profile of the BEC density $\rho(\mathbf{r})$ in a cigar shaped harmonic trap, with long axis along y. In cylindrical coordinates

$$\rho(r, y, \phi) = \frac{1}{U_0}\left(\mu - \frac{m}{2}(\omega_r^2 r^2 + \omega_y^2 y^2)\right) \times \Theta\left(\mu - \frac{m}{2}(\omega_r^2 r^2 + \omega_y^2 y^2)\right) \ , \tag{8.1}$$

where Θ is the Heaviside step function, $r = \sqrt{x^2 + z^2}$, μ the chemical potential, the mass of the bosons m and the trapping frequencies ω_r in the radial direction and ω_y along the long axis of the BEC.

From the density distribution we derive the corresponding cumulative distribution functions (CDFs) for each coordinate that allow us to randomly draw particle positions matching the probability of finding atoms at a certain position inside the BEC. The extension of the BEC in the long direction is between

$$y_{\max} = -y_{\min} = \sqrt{2\mu/(m\omega_y^2)} \ , \tag{8.2}$$

and then for each y an upper bound for the radial coordinate is given by

$$r_{\max}(y) = 1/\omega_r \sqrt{2\mu/m - \omega_y^2 y^2} \ . \tag{8.3}$$

Consequently, the total particle number of the BEC is given by

$$N = \int_{y_{\min}}^{y_{\max}} \mathrm{d}y \underbrace{\int_0^{r_{\max}(y)} \mathrm{d}r \underbrace{\int_0^{2\pi} \mathrm{d}\phi \; r\, n(r,y,\phi)}_{=\bar{n}_\phi(r,y)}}_{=\bar{n}_{r,\phi}(y)} \ , \tag{8.4}$$

where $\bar{n}_{r,\phi}(y)\ \mathrm{d}y$ gives the contribution of a disc with thickness $\mathrm{d}y$ (i.e. a cross-section of the BEC) and $\bar{n}_\phi(r,y)\ \mathrm{d}y\ \mathrm{d}r$ characterizes the contribution to the total density of an infinitesimal cylinder of radius r for a given value of y. The CDF of the y-coordinate is given by

$$\mathrm{CDF}_{n_{r,\phi}}(y) = \frac{1}{N} \int_{y_{\min}}^{y} \mathrm{d}y' \, \bar{n}_{r,\phi}(y') \ , \tag{8.5}$$

which maps the possible y-coordinates onto the interval $[0,1]$. Hence we can use the inverse CDF to draw random numbers $\xi_y^* \in [0,1]$ and assign them to y-coordinates y^*, which are then correctly distributed according to the density of the Thomas-Fermi profile of the BEC. Analogously, we obtain the CDF of the radial coordinate

$$\mathrm{CDF}_{\bar{n}_\phi}(r,y)\big|_{y=y^*} = \frac{1}{N} \int_0^{r} \mathrm{d}r' \, \bar{n}_\phi(r',y)\big|_{y=y^*} \ . \tag{8.6}$$

The inverse of $\mathrm{CDF}_{\bar{n}_\phi}(r,y^*)$ assigns a random number $\xi_r^* \in [0,1]$ to an r-coordinate r^* under the condition that the atom is found at the y-coordinate y^*, which has been obtained in the previous step. Finally the ϕ-coordinate is drawn uniformly from the interval $[0,2\pi)$, as the density profile Eq. (8.1) of the BEC is invariant under rotation around the y-axis. By successively drawing random numbers $\xi \in [0,1]$ and converting them into coordinates as described above, we obtain three-dimensional atom positions forming a cloud that matches the density distribution of a BEC confined in a harmonic trap. For an illustration of a distribution drawn using this approach see Fig. 8.1(a).

In the following we describe how to select atoms from this cloud to be excited into a Rydberg state by a laser beam with a Gaussian profile and exploiting the density detuning of the energy of the Rydberg state. The overall excitation probability is proportional to the intensity profile of the Gaussian beam which we assume to propagate parallel to

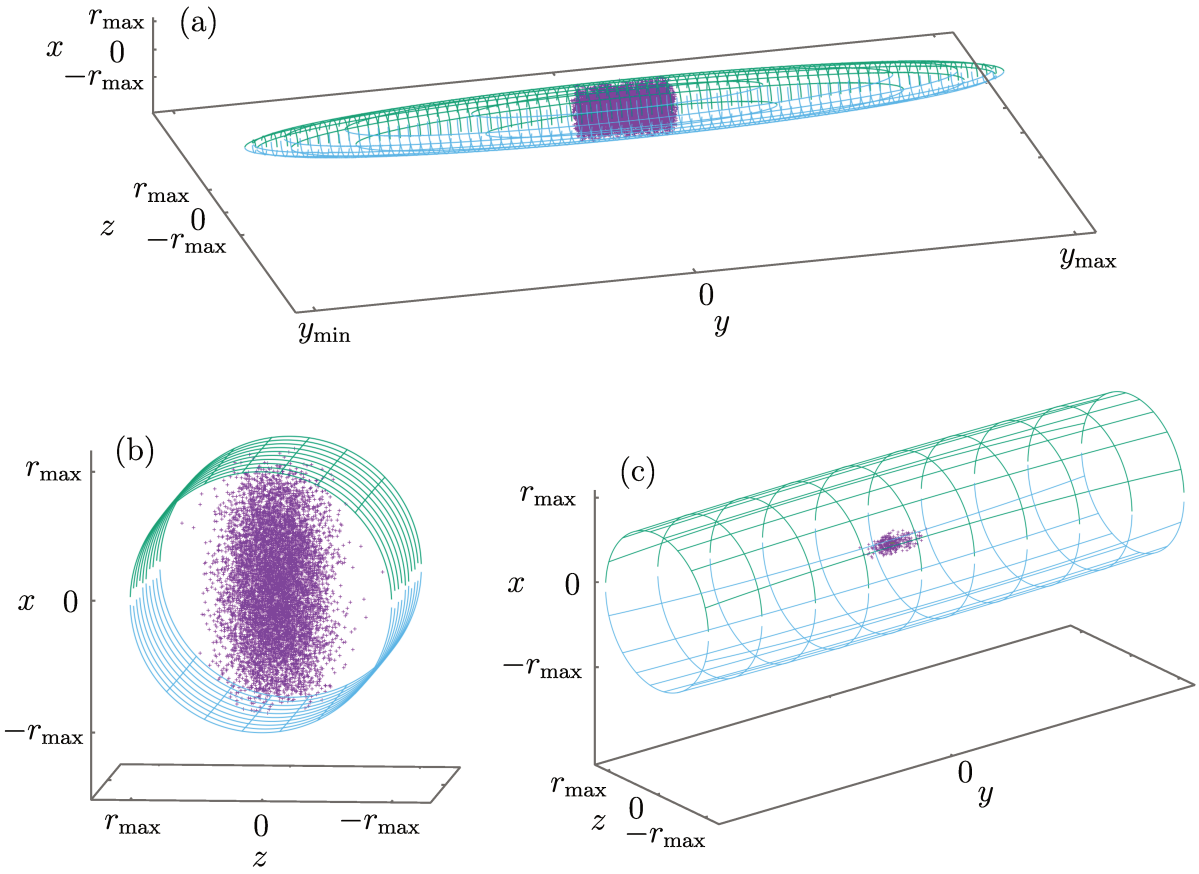

Figure 8.1.: Illustration of the spacial distribution of atoms and excitation process. Panel (a) shows the Thomas-Fermi profile and the section which is used for the semi-classical simulation in the next section where we model a BEC containing 10^6 atoms. The central region depicted here (relevant for the dynamics discussed in Section 8.2) contains approx. 225 000 atoms (purple). Panel (b) shows the atoms that are excited according to the intensity profile of a Gaussian beam. The final excitation positions that take into account the energy detuning and line width of the excitation laser are shown in (c).

the x-axis of our coordinate system. To implement this, we evaluate the laser intensity profile [120]

$$I(r_\perp, x) = I_0 \frac{\omega_0^2}{\omega(x)^2} \, e^{-\frac{2r_\perp^2}{\omega(x)^2}} \tag{8.7}$$

at the position of each atom within the cloud, where we defined

$$\begin{aligned} r_\perp &= \sqrt{y^2 + z^2} \, , \\ \omega(x) &= \omega_0 \sqrt{1 + (x/x_R)^2} \, . \end{aligned} \tag{8.8}$$

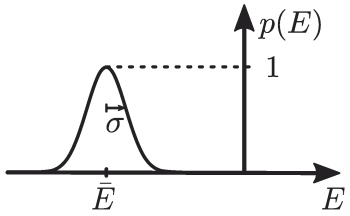

Figure 8.2.: Illustration of the energy dependence of the excitation probability $p(E)$ (given in Eq. (8.9)). The normalization factor $\mathcal{N}$ is chosen such that $p(\bar{E}) = 1$ allowing to assign a probability to each excitation with energy detuning E. This ensures that excitations which precisely match the energy detuning of $\bar{E}$ are guaranteed to happen and excitations that produce a different energy shift are represented accordingly in the overall number of excitation positions.

Here $x_R = \pi\,\omega_0^2/\lambda$ is the Rayleigh range. In accordance with a typical experimental setup [34], we choose a waist radius $\omega_0 = 1.8\,\mu m$ and wave length $\lambda = 1.011\,\mu m$. We keep I_0 dimensionless and define it such that the sum of all $I(r_\perp, x)$ evaluated at all atom positions is normalized to one. Assuming the excitation of exactly one Rydberg atom, the function $I(r_\perp, x)$ can then directly be taken as the excitation probability of an atom at location $(r_\perp, x)$. This allows to select atoms to be excited into a Rydberg state according to the Gaussian intensity profile of the excitation laser. Fig. 8.1(b) shows the distribution of atoms selected from the initial cloud corresponding to the probability distribution resulting from the laser intensity profile.

In addition to the dependence on the laser intensity and the density profile of the cloud, the excitation probability of an atom into a Rydberg state carries an additional density dependence caused by the energies of the neighboring atoms being shifted by the presence ULRRM potential. The spectral width of the laser only allows for excitations within a certain energy range ΔE, caused by a matching density in the vicinity of the Rydberg atom. We assume a Gaussian line shape of the excitation laser and hence an energy dependence of the excitation probability

$$p(E) = \mathcal{N}\, e^{-\frac{(E-\bar{E})^2}{\Delta E^2}}, \tag{8.9}$$

with width ΔE centered around a detuning $\bar{E}$ (see Fig. 8.2). This detuning is chosen matching to a recent experiment [34] by $\Delta E = 1$ MHz and $\bar{E} = -55$ MHz. If the normalization factor $\mathcal{N}$ is chosen such that $p(\bar{E}) = 1$, this assigns a probability to each excitation with energy detuning E. For each atom, the energy E is found by summing the potential energy shift due to the ULRRM potential Eq. (5.7) for all other atoms in the cloud

$$E = \sum_i V_{\mathrm{ryd}}(|\boldsymbol{R}_i - \boldsymbol{x}|). \tag{8.10}$$

Here $\boldsymbol{x}$ is the location of the atom for which the excitation probability is calculated and $\boldsymbol{R}_i \neq \boldsymbol{x}$ is the location of the ith atom inside the cloud.

Finally the total Rydberg excitation probability for each atom in the cloud is given by $I(r_\perp, x) \times p(E)$. The spatial distribution of Rydberg excitation positions following from this probability distribution is illustrated in Fig. 8.1(c). In the following we use these excitation positions as input for a semiclassical simulation of the dynamics of atoms in a BEC when one of the atoms of the BEC is excited into a Rydberg state.

8.2. Semiclassical Trajectory Dynamics

We now use the positions of Rydberg excitation as inputs for the simulation of the dynamics of atoms in the vicinity of a Rydberg atom which is excited from a BEC. To this end, we solve the classical Hamilton's equations of motion

$$\begin{aligned} \dot{\boldsymbol{q}}_i &= \frac{\partial \mathcal{H}}{\partial \boldsymbol{p}_i} \ , \\ \dot{\boldsymbol{p}}_i &= -\frac{\partial \mathcal{H}}{\partial \boldsymbol{q}_i} \ , \\ \mathcal{H} &= \sum_i \frac{\boldsymbol{p}_i^2}{2m} + V(\boldsymbol{q}_i, t) \ , \end{aligned} \tag{8.11}$$

for an ensemble of N classical non-interacting particles using a fourth-order Runge-Kutta method. Initially all atoms rest and are arranged according to the probability distribution resembling the Thomas-Fermi profile (see Eq. (8.1)) with $\omega_r = 2\pi \times 197\,\mathrm{Hz}$, $\omega_y = 2\pi \times 15\,\mathrm{Hz}$. We model clouds with 10^6 ^{87}Rb atoms to match the experimental setup of [34]. Following the procedure described above one atom is chosen to be excited into a Rydberg state. The other particles move accordingly to the ULRRM interaction potential Eq. (5.7)

$$V(\boldsymbol{q}, t) = \begin{cases} V_{\mathrm{ULRRM}} & , \quad t \in T_{\mathrm{Ryd}} \\ 0 & , \quad \text{otherwise} \end{cases} \ , \tag{8.12}$$

where T_{Ryd} is the set of time intervals with a Rydberg atom present in the cloud (see Fig. 8.3). We model a pulse sequence as studied in [34]. One pulse consists of 3.5 μs in which a Rydberg atom is present and the ground-state atoms move in the Rydberg potential. Afterwards the Rydberg atom is ionized and removed from the cloud. Subsequently, atoms move freely for 1.3 μs before the next atom is excited into a Rydberg state. After the pulse sequence the particles evolve freely for 250 μs (see Fig. 8.3).

Additionally we model the effects of three-body loss. In order to do that we calculate the local density around each atom and remove the three respective atoms from the cloud according to the probability distribution p_{3bl} resulting from the density change due to three-body loss [121]

$$\dot{n} = -L_3\, n^3 = -L_3 \frac{N^3}{V^3} \quad \Rightarrow \quad p_{\mathrm{3bl}} = \frac{\Delta N}{N} = -L_3\, \Delta t\, \frac{N^2}{V^2} \ , \tag{8.13}$$

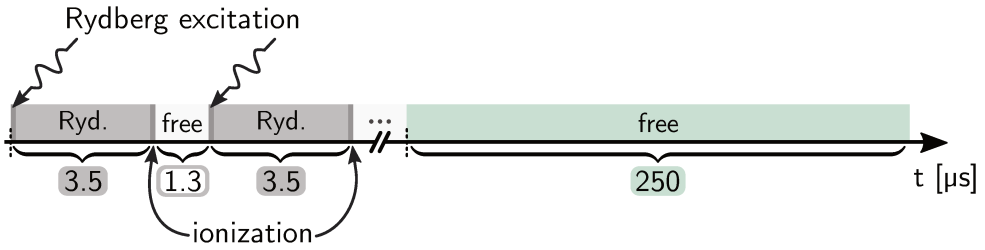

Figure 8.3.: Illustration of the pulse sequence. An evolution of 3.5 μs of the atoms of the BEC in which the Rydberg potential is present is followed by 1.3 μs of free evolution before the next atom is excited into a Rydberg state. Here we assume an instantaneous creation as well as ionization and subsequent extraction of the Rydberg atom from the BEC.

where $L_3 = 1.8 \times 10^{-29}\mathrm{cm}^6/\mathrm{s}$ [122] characterizes the rate of the three-body loss. In our simulation the time interval Δt is the Runge-Kutta step and V is a small volume around each individual atom containing a sufficient amount of atoms to reproduce the correct peak density of the respective Thomas-Fermi profile. For our simulations we consider the 25 nearest neighbors around each individual atom to calculate local densities as this presents itself to be a good trade-off between obtaining consistent densities and not underestimating local densities due to averaging over a too large volume. For each time step of the simulation we compute the probability $p_{3\mathrm{bl}}$ for each atom and remove the respective atoms accordingly.

While the Rydberg atom is present atoms are accelerated radially, moving either towards or away from the Rydberg atom (see Fig. 8.4). After the Rydberg atom is removed from the cloud all atoms move freely with the momentum they have gathered previously. In simulations with a single Rydberg excitation all trajectories of inward-moving atoms intersect at the position of the Rydberg excitation causing a temporal increase of the local density. This approximation is exact if the dynamics of the Rydberg atom itself is neglected, which is reasonable as the excitation is most likely to occur in the center of the BEC where the density profile around the Rydberg atom is approximately inversion symmetric resulting in a vanishing accelerating force on the Rydberg core itself.

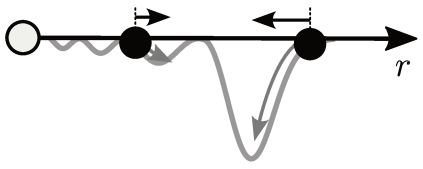

Figure 8.4.: Illustration of the radial acceleration of ultracold atoms (black dots) of a BEC in the vicinity of a Rydberg atom located ar $r = 0$. Depending on their distance from the Rydberg core, atoms are either accelerated towards or away from Rydberg core.

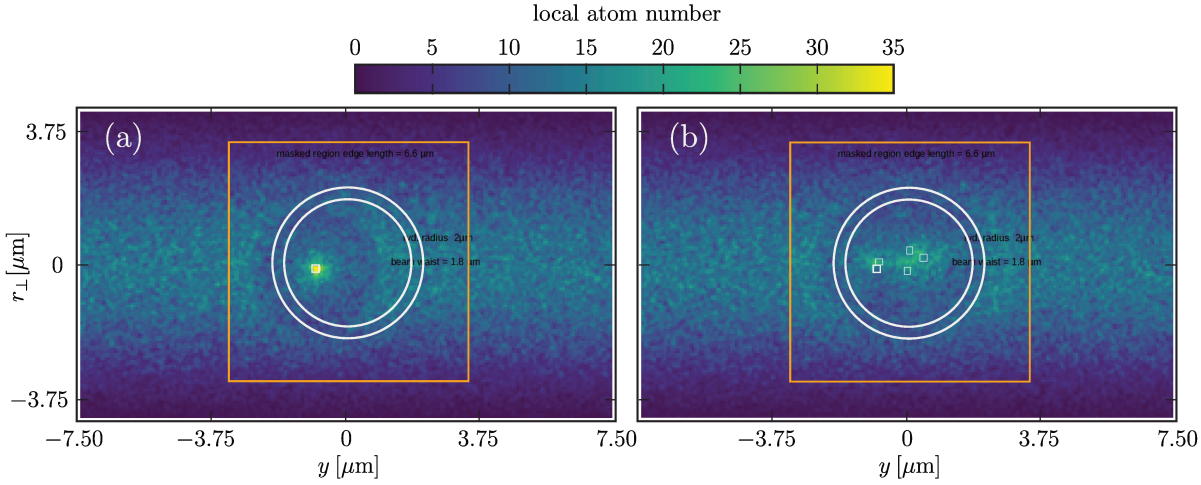

Figure 8.5.: Integrated atom number along the x-axis for a single Rydberg excitation (a) and 5 successive Rydberg excitations (b) after 250 μs of free evolution. The smaller circle gives the diameter of the Gaussian beam in the focal plane and the larger circle illustrates the size of the Rydberg orbit of a $l = 0$, $n = 133$ ^{87}Rb Rydberg state. The orange square is the region that is used to calculate the number of lost atoms by comparing the atoms within the region of the initial cloud of atoms to the number of atoms inside the region in each time step. The small squares mark the Rydberg excitation positions.

The effect of an increased local density at the location of the Rydberg excitation can be seen in Fig. 8.5(a) which shows the local atom number of the central region of the BEC after the simulated sequence for a single Rydberg excitation. Similar effects are also found in [P2]. The presentation of data in Fig. 8.5 is motivated by absorption images and phase-contrast images obtained from experiments [34], which correspond to integrated densities rather than local densities due to the projection along the imaging axis. From a comparison to a simulation that does not include three-body loss it is found that three-body loss plays a crucial role as it reduces the height of the central peak by a factor of approximately 1/4.

This focusing effect becomes less pronounced the longer the pulse sequence (the more Rydberg atoms are excited) as in this case, in contrast to the scenario of a single Rydberg excitation, the trajectories are not passing through the same point. This effect can be seen in Fig. 8.5(b) which shows the local atom number of the central region of the BEC after a pulse sequence of five individual Rydberg excitations. As a consequence the influence of three-body loss on the total number of lost atoms becomes smaller. The qualitative behavior of the BEC in the vicinity of the Rydberg excitation matches the findings of a simulation based on the solution of the radial Gross-Pitaevskii equation in [P2] and experiments [34].

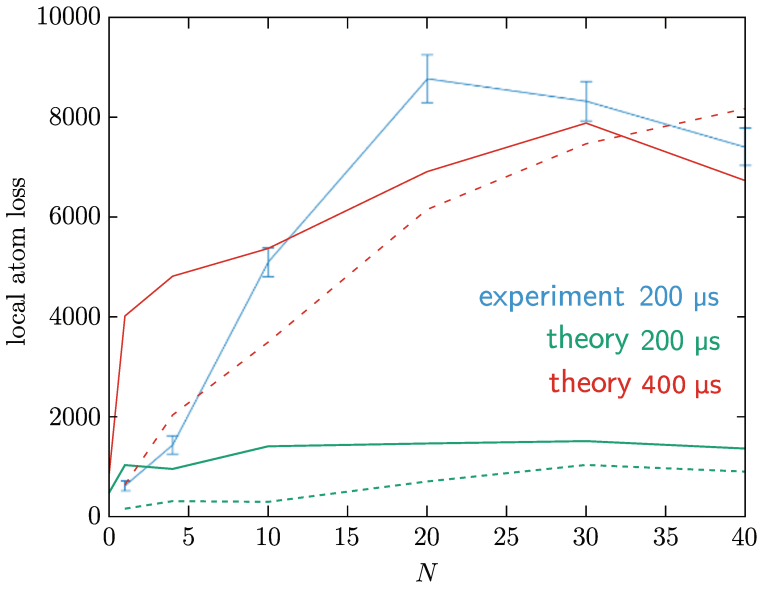

Figure 8.6.: Comparison of the atom loss after N consecutive Rydberg excitations in a BEC after 200 μs of free evolution. The blue line marks the experimental results taken from [34]. The green line shows the results of a semiclassical simulation (the dashed lines neglect the effect of three body loss). The red lines show the theoretical prediction for a free evolution time of 400 μs. Each theoretical data point is obtained from a single simulation. We expect smoother behavior if the results of many individual simulations are averaged.

However, the semiclassical simulation quantitatively underestimates the number of atoms lost from the cloud by one order of magnitude. Fig. 8.6 compares the atom loss observed in experiments [34] and the numerical results of the semiclassical simulation of the excitation sequence illustrated in Fig. 8.3 for a free evolution time of 200 μs. The theoretical results are obtained from a simulation of one initial configuration and N consecutive Rydberg excitations. We expect a smoother behavior after statistically averaging over many individual simulations. In the numerical simulation the atoms have not yet left the region that is used to detect the atom number after 200 μs, resulting in a smaller number of lost atoms and a plateau of the numerical results (see green line in Fig. 8.6). To bring the numerical results into approximately the same region as found in the experiment the free evolution time following the pulse sequence has to be doubled (see red line in Fig. 8.6).

8.3. Summary

In this chapter we have numerically modeled the loss of atoms from a BEC caused by the repeated excitation of Rydberg atoms using a semiclassical description. To this end, we first investigated the distribution of Rydberg excitation positions within a harmonically confined BEC. Then we solved the classical equations of motion of an ensemble of point-like particles resembling the density profile of a harmonically trapped BEC. While the overall qualitative behavior of the numerical simulation matches experimental results, our results predict longer time scales for the loss dynamics as those found in experiments. The study of the fundamental reason for the much faster dynamics observed in the experiment [34] is left for future work.

9. Conclusion

In this thesis we have investigated two fields of physics where the scattering of particles and the accompanying formation of bound states gives rise to interesting new possibilities to control and probe many-body quantum systems.

In the first part we have studied the scattering of charge carriers in two-dimensional semiconductors. We have seen how the concept of Feshbach resonances as known from ultracold atoms can be extended to exciton-electron scattering in two-dimensional materials. In Chapter 3 we provided a new theoretical framework that allows to understand two-dimensional exciton-electron Feshbach resonances from a microscopic few-particle point of view and does not rely on the assumption of preexisting excitonic states. We found two types of electronically tunable Feshbach resonances that can be used to control interactions between electrons and either short-lived intralayer excitons or long-lived interlayer excitons in TMD heterostructures. The first one promises to find applications in injection spectroscopy of intralayer excitons with large oscillator strength to probe correlations of electronic systems, whereas the latter can be used to bring tunable interactions to Bose-Fermi mixtures comprising electrons and long-lived interlayer excitons.

The two-dimensional nature of these systems results in a rather unintuitive behavior of scattering at the resonance, where interactions effectively vanish. In contrast, ultracold atoms in three-dimensions are strongly interacting at the resonance position. This indicates the necessity to discard the usual definition of the resonance width when describing two-dimensional Feshbach resonances. We have also introduced a toy-model description of the two-dimensional Fermi-polaron problem. Here this particular feature of two-dimensional Feshbach resonances that the phase shifts (i.e., the effective interactions) vanish at the resonance position results in the emergence of a repulsive polaron branch with zero spectral weight in the optical signatures of the respective two-dimensional Fermi polaron. Moreover we investigated a possible realization of a Bose-Hubbard type model for excitons in TMDs where excitons move in lattices formed by two-dimensional charge-ordered states and the previously introduced Feshbach resonances were used to tune the exciton-lattice interactions. We have found that the emerging excitonic bands can be tuned to a regime with negative curvature, suggesting a negative effective exciton mass, indicating a regime in which anomalous exciton diffusion could be observable.

In Chapter 4 we have developed an effective theory for exciton-electron scattering in TMDs that treats excitons as rigid point-like particles and captures the energetic properties of trions while being simple enough to be applicable in many-body calculations. We have found that two-dimensional exciton-electron scattering can be described by essentially the same type of models used to describe the scattering of ultracold atoms,

again underlining the analogy between two-dimensional materials and ultracold atoms.

In the second part of this thesis we have investigated how the creation of ultralong-range Rydberg molecules (ULRRMs) in an ultracold quantum gas allows to probe correlations on (sub-optical) length scales given by the Rydberg radius. In Chapter 6 we have developed an approximate description of ULRRM dimers in an ideal Fermi sea that can be used to calculate the dimer absorption signal using Fermi's golden rule. We found that the line strength of the ULRRM dimer in the Rydberg absorption spectrum is directly related to the pair correlation function of the Fermi sea. Moreover, we have shown that the particular shape of the s-wave ULRRM-dimer state, where a ground-state atom is located on a thin spherical shell (resembling the Rydberg orbit) around the Rydberg core, allows to use these molecules as probe for inter-particle spacings on sub-optical length scales.

In Chapter 7 we have applied this new sensing tool to a gas of Feshbach molecules and the Fermi-polaron problem and found that Rydberg excitations also provide a way to probe correlations in the context of interacting systems. The additional separation of timescales of the ULRRM formation and the typical dynamics in ultracold atoms suggests that ULRRMs can be used as an in-situ, time-resolved probe of the quantum gas in the vicinity of the Rydberg atom. The novel way of probing correlations using Rydberg excitations in interacting many-body systems is a promising new tool to experimentally study non-equilibirum quantum dynamics in strongly correlated systems.

In Chapter 8 we applied a semiclassical theory to describe the dynamics of atoms in a BEC when one of the atoms is excited into a Rydberg state. This investigation tried to explain the atom loss found in recent experiments [34]. While the overall qualitative behavior of the semiclassical model matched the experimental findings the theoretical timescales of the atom loss underestimated the ones found in the experiment hinting to a crucial role of quantum effects present in such experiments and opens the avenue for further theoretical and experimental investigations.

As we have outlined in the summary above, there are interesting future venues following from the results of this thesis. In particular, the tunability of exciton-charge interactions resulting from the Feshbach resonances discussed in Chapter 3 opens new possibilities to implement and study many-body models known from ultracold atoms in solid-state systems (such as, e.g., supersolidity in dipolar exciton condensates [92–94]), further substantiating the analogy between ultracold atoms and van der Waals materials. Moreover, studying the theory of exciton-charge Feshbach resonances beyond the TMD-bilayer scenario (i.e., in the case of three layers) could provide a microscopic understanding of the interactions that lead to exciton-induced superconductivity [89–91] in TMD heterostructures. Further, an extension of the framework developed in Chapter 6 to a description of Rydberg excitations in arbitrary states of ultracold atoms would provide a general theory of Rydberg excitation microscopy of correlations in ultracold quantum gases. This would allow to investigate, e.g., the BCS-BEC crossover [96], ferromagnetic domain walls in strongly interacting Fermi gases [111–114], or the domains within phase separated states of Bose-Fermi mixtures [115] or spin-imbalanced Fermi gases [116].

A. Details: From Lippmann-Schwinger Equation to Tunable Scattering Lengths

In the following we provide details on the two-channel model presented in Section 2.2.2. We start by showing that the state

$$\hat{G}\hat{V}\,|\boldsymbol{k},-\boldsymbol{k}\rangle = \frac{g}{\sqrt{V}}\,\mathcal{G}_0(E)\,\hat{b}_{\mathbf{0}}^{\dagger}\,|0\rangle \tag{A.1}$$

is an eigenstate of $(\hat{G}\hat{V}\hat{G}\hat{V})^n$, i.e.,

$$\begin{aligned}
\hat{G}\hat{V}\hat{G}\hat{V}\,\hat{b}_{\mathbf{0}}^{\dagger}\,|0\rangle &= \hat{G}\hat{V}\hat{G}\frac{g}{\sqrt{V}}\sum_{\boldsymbol{p}}|\boldsymbol{p},-\boldsymbol{p}\rangle \\
&= \frac{g}{\sqrt{V}}\,\hat{G}\hat{V}\sum_{\boldsymbol{p}}\frac{1}{E-\varepsilon_{\boldsymbol{p}}+\mathrm{i}\epsilon}\;|\boldsymbol{p},-\boldsymbol{p}\rangle \\
&= \frac{g}{\sqrt{V}}\,\hat{G}\sum_{\boldsymbol{p}}G_0(E,\boldsymbol{p})\,\frac{g}{\sqrt{V}}\hat{b}_{\mathbf{0}}^{\dagger}\,|0\rangle \\
&= \frac{g^2}{V}\sum_{\boldsymbol{p}}G_0(E,\boldsymbol{p})\,\hat{G}\,\hat{b}_{\mathbf{0}}^{\dagger}\,|0\rangle \\
&= \frac{g^2}{V}\sum_{\boldsymbol{p}}G_0(E,\boldsymbol{p})\,\frac{1}{E-\nu_B+\mathrm{i}\epsilon}\,\hat{b}_{\mathbf{0}}^{\dagger}\,|0\rangle \\
&= \frac{g^2}{V}\mathcal{G}_0(E)\sum_{\boldsymbol{p}}G_0(E,\boldsymbol{p})\,\hat{b}_{\mathbf{0}}^{\dagger}\,|0\rangle\;\;,
\end{aligned} \tag{A.2}$$

where we defined

$$\mathcal{G}_0(E) = \frac{1}{E-\nu_B+\mathrm{i}\epsilon} \tag{A.3}$$

and

$$G_0(E,p) = \frac{1}{E-\varepsilon_{\boldsymbol{p}}+\mathrm{i}\epsilon}\;. \tag{A.4}$$

This can be used to evaluate the transition matrix elements (see Eq. (2.6))

$$
\begin{aligned}
\langle \boldsymbol{k}', -\boldsymbol{k}' | \hat{T} | \boldsymbol{k}, -\boldsymbol{k} \rangle &= \langle \boldsymbol{k}', -\boldsymbol{k}' | \hat{V} \sum_{n=0}^{\infty} (\hat{G}\hat{V})^{2n} \hat{G}\hat{V} | \boldsymbol{k}, -\boldsymbol{k} \rangle \\
&= \frac{g}{\sqrt{V}} \mathcal{G}_0(E) \, \langle \boldsymbol{k}', -\boldsymbol{k}' | \hat{V} \, \hat{b}_{\boldsymbol{0}}^{\dagger} | 0 \rangle \sum_{n=0}^{\infty} \left(\frac{g^2}{V} \mathcal{G}_0(E) \sum_{\boldsymbol{p}} G_0(E, \boldsymbol{p}) \right)^n \\
&= \frac{g^2}{V} \mathcal{G}_0(E) \, \langle \boldsymbol{k}', -\boldsymbol{k}' | \sum_{\boldsymbol{p}'} | \boldsymbol{p}', -\boldsymbol{p}' \rangle \sum_{n=0}^{\infty} \left(\frac{g^2}{V} \mathcal{G}_0(E) \sum_{\boldsymbol{p}} G_0(E, \boldsymbol{p}) \right)^n \\
&= \frac{g^2}{V} \mathcal{G}_0(E) \sum_{n=0}^{\infty} \left(\mathcal{G}_0(E) \frac{g^2}{V} \sum_{\boldsymbol{p}} G_0(E, \boldsymbol{p}) \right)^n \\
&= \frac{g^2}{V} \mathcal{G}_0(E) \sum_{n=0}^{\infty} \left(\mathcal{G}_0(E) \, g^2 \int \frac{\mathrm{d}^3 \boldsymbol{p}}{(2\pi)^3} G_0(E, \boldsymbol{p}) \right)^n \\
&= \frac{g^2}{V} \mathcal{G}_0(E) \sum_{n=0}^{\infty} \left(\mathcal{G}_0(E) \, g^2 \underbrace{\int \frac{\mathrm{d}^3 \boldsymbol{p}}{(2\pi)^3} \frac{1}{E - \epsilon_{\boldsymbol{k}} + \mathrm{i}\epsilon}}_{:= \Sigma(E)} \right)^n \\
&= \frac{g^2}{V} \mathcal{G}_0(E) \sum_{n=0}^{\infty} \left(g^2 \, \mathcal{G}_0(E) \, \Sigma(E) \right)^n \\
&= \frac{g^2}{V} \mathcal{G}_0(E) \, \frac{1}{1 - g^2 \, \mathcal{G}_0(E) \, \Sigma(E)} \\
&= \frac{1}{V} \, \frac{1}{\mathcal{G}_0^{-1}(E)/g^2 - \Sigma(E)} \\
&\approx \frac{1}{V} \, \frac{1}{\frac{E - \nu_B + \mathrm{i}\epsilon}{g^2} - \frac{1}{V} \sum_{|\boldsymbol{p}| < \Lambda} \frac{1}{E - \epsilon_{\boldsymbol{p}} + \mathrm{i}\epsilon}} \, ,
\end{aligned}
\tag{A.5}
$$

where we used the geometric series to obtain the third last line, i.e., $\sum_{n=0}^{\infty} a x^n = \frac{a}{1-x}$, if: $|x| < 1$, and identified the self energy (with momentum cutoff Λ)

$$
\begin{aligned}
\Sigma(E) &= \int \frac{\mathrm{d}^3 \boldsymbol{p}}{(2\pi)^3} \frac{1}{E - \epsilon_{\boldsymbol{p}} + \mathrm{i}\epsilon} \\
&= \frac{1}{V} \sum_{\boldsymbol{p}} \frac{1}{E - \epsilon_{\boldsymbol{p}} + \mathrm{i}\epsilon} \\
&\approx \frac{1}{V} \sum_{|\boldsymbol{p}| < \Lambda} \frac{1}{E - \epsilon_{\boldsymbol{p}} + \mathrm{i}\epsilon} \, .
\end{aligned}
\tag{A.6}
$$

B. Functional Determinant Approach

In the following ($\hbar = 1$) we follow the derivation of the Levitov-Klich formula [118, 119] and sketch how the Lohschmidt Echo

$$S(t) = \det\left(1 - \hat{n} + \hat{n}\, \mathrm{e}^{-\mathrm{i}\hat{h}_0 t}\, \mathrm{e}^{\mathrm{i}\hat{h}t}\right) \tag{B.1}$$

can be treated effectively numerically.

The free Hamiltonian is given by

$$\begin{aligned} \hat{H}_0 &= \sum_{\boldsymbol{k}} \varepsilon_{\boldsymbol{k}} c^\dagger_{\boldsymbol{k}} c_{\boldsymbol{k}} = \sum_{\boldsymbol{k}} \langle \boldsymbol{k}| \, \frac{\hat{\boldsymbol{k}}^2}{2m} \, |\boldsymbol{k}\rangle \, c^\dagger_{\boldsymbol{k}} c_{\boldsymbol{k}} \ , \\ \hat{h}_0 &= \frac{\hat{\boldsymbol{k}}^2}{2m} = -\frac{\hbar^2 \boldsymbol{\nabla}^2}{2m} \ , \end{aligned} \tag{B.2}$$

with three-dimensional momenta $\boldsymbol{k}$, the mass m of the fermionic particles and energy $\varepsilon_{\boldsymbol{k}} = k^2/(2m)$. Analogously we find the full Hmiltonian (that includes the interaction potential)

$$\hat{h} = \frac{\hat{\boldsymbol{k}}^2}{2m} + V(\hat{\boldsymbol{r}}) \ , \tag{B.3}$$

with a spherical symmetric potential $V(\boldsymbol{r}) = V(r)$. We will denote the respective eigenstates and eigenvalues as follows

$$\begin{aligned} \hat{h}_0 \, |nlm\rangle &= \varepsilon_{nlm} \, |nlm\rangle \ , \\ \hat{h} \, |\nu lm\rangle &= \omega_{\nu lm} \, |\nu lm\rangle \ , \end{aligned} \tag{B.4}$$

and the respective wave functions are given by

$$\begin{aligned} \langle \boldsymbol{r}|nlm\rangle &= \phi_{nlm}(\boldsymbol{r}) = \frac{u_{nl}(r)}{r} Y_{lm}(\Omega_{\boldsymbol{r}}) \ , \\ \langle \boldsymbol{r}|\nu lm\rangle &= \psi_{\nu lm}(\boldsymbol{r}) = \frac{v_{\nu l}(r)}{r} Y_{lm}(\Omega_{\boldsymbol{r}}) \ . \end{aligned} \tag{B.5}$$

The indices n (resp. ν), l and m label the principal quantum number, angular momentum quantum number and angular momentum projection quantum number. We want to solve the problem in a spherical potential well (cf. Fig. B.1a). Thus the radial functions $u_{nl}(r)$ and $v_{\nu l}(r)$ have to fulfill the boundary conditions

$$u_{nl}(L) = v_{\nu l}(L) = u_{nl}(0) = v_{\nu l}(0) = 0 \ . \tag{B.6}$$

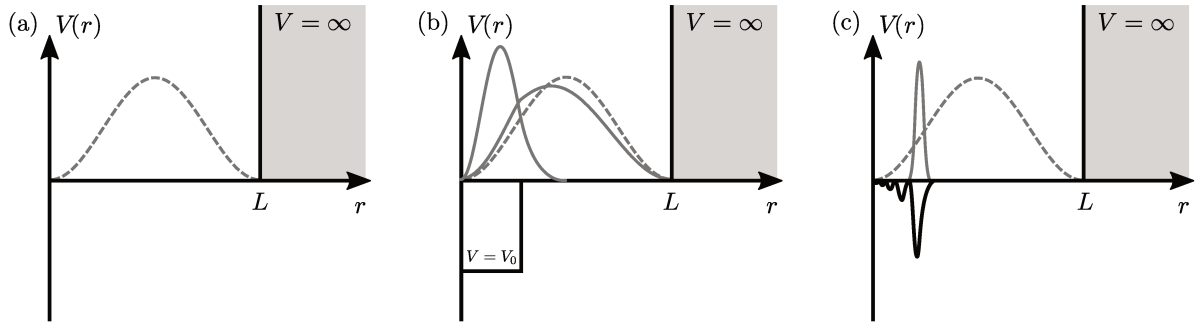

Figure B.1.: Sketches of different radial potential wells. The radial ground state wave function $u_{\nu l}(r)$ (free problem) is shown as a dashed line. The other panels additionally show the radial wave functions of the ground state in a three-dimensional square-well potential for two choices of V_0 in (b) and the ULRRM-dimer ground state (c.f. Fig. 5.2) in (c) and the respective interaction potentials.

The radial Schrödinger equations are given by

$$\begin{aligned}\left[-\frac{\partial_r^2}{2m}+\frac{l(l+1)}{2mr^2}\right]u_{nl}(r)&=\varepsilon_{nl}u_{nl}(r)\ ,\\ \left[-\frac{\partial_r^2}{2m}+\frac{l(l+1)}{2mr^2}+V(r)\right]v_{\nu l}(r)&=\omega_{\nu l}v_{\nu l}(r)\ .\end{aligned} \tag{B.7}$$

The free problem is solved by

$$u_{nl}(r)=\mathcal{N}_{nl}\,r\,j_l(k_{nl}r)\ , \tag{B.8}$$

with spherical Bessel functions $j_l(x)$. In the case $l=0$ we obtain

$$u_{n0}(r)=\mathcal{N}_{n0}\sin(k_{n0}r)\ . \tag{B.9}$$

from the boundary condition $u_{n0}(L)=0$ we obtain $k_{n0}=n\pi/L$ and the normalization ($\int \mathrm{d}r|u_{n0}|^2=1$) yields $\mathcal{N}_{n0}=(2/L)^{(1/2)}$.

In general we solve Eq. (B.7) numerically by discretizing the radial coordinate. To do so we define a uniform grid $r\in\{r=n\Delta r|n=0,1,...N\}$ (one could also use DVR, see Appendix C, or any other method of choice to numerically represent the Hamiltonian) on which we use finite difference coefficients allowing to represent the second derivative according to

$$\partial_r^2=\frac{1}{\Delta r^2}\begin{pmatrix}-2 & 1 & & & & 0\\ 1 & -2 & 1 & & & \\ & 1 & -2 & 1 & & \\ & & \ddots & \ddots & \ddots & \\ 0 & & & 1 & -2 & 1\end{pmatrix}\ . \tag{B.10}$$

From the numerical diagonalization of the respective Hamiltonians we obtain two sets of eigenenergies and eigenfunctions $\{(\varepsilon_{nl}, \boldsymbol{u}_{nl}), ...\}$ and $\{(\omega_{\nu l}, \boldsymbol{v}_{\nu l}), ...\}$ which are used to evaluate the determinant of

$$\hat{B} = \left(1 - \hat{n} + \hat{n}\mathrm{e}^{-\mathrm{i}\hat{h}_0 t}\mathrm{e}^{\mathrm{i}\hat{h}t}\right) , \tag{B.11}$$

with

$$\hat{n} = \frac{1}{\mathrm{e}^{\beta(\hat{h}_0 - \mu)} + 1} . \tag{B.12}$$

One then computes the representation of $\hat{B}$ in the eigenbasis of $\hat{h}_0$ and uses its block diagonal form as the $2l + 1$ states with fixed values of l and m form orthonormal bases in l invariant subspaces. This allows the determinant to be rewritten as

$$\det(\hat{B}) = \prod_{lm} \det(\hat{B}_{lm}) = \prod_{l} \det(\hat{B}_l)^{2l+1} = S(t) , \tag{B.13}$$

and one finds

$$\begin{aligned}
\langle n'l'm'|\, \hat{B}\, |nlm\rangle &= \delta_{nn'}\delta_{ll'}\delta_{mm'} - \delta_{nn'}\delta_{ll'}\delta_{mm'} n(\varepsilon_{nlm}) + \underbrace{\langle n'l'm'|\, \hat{n}\mathrm{e}^{-\mathrm{i}\hat{h}_0 t}\mathrm{e}^{\mathrm{i}\hat{h}t}\, |nlm\rangle}_{(*)} \\
(*) &= n(\varepsilon_{n'lm})\, \mathrm{e}^{-\mathrm{i}\varepsilon_{n'lm}t}\, \langle n'l'm'|\, \mathrm{e}^{\mathrm{i}\hat{h}t}\, |nlm\rangle \\
&= n(\varepsilon_{n'lm})\, \mathrm{e}^{-\mathrm{i}\varepsilon_{n'lm}t} \sum_{\nu\, l''m''} \langle n'l'm'|\, \mathrm{e}^{\mathrm{i}\hat{h}t}\, |\nu\, l''m''\rangle\, \langle \nu\, l''m''|nlm\rangle \\
&= n(\varepsilon_{n'lm})\, \mathrm{e}^{-\mathrm{i}\varepsilon_{n'lm}t} \sum_{\nu\, l''m''} \mathrm{e}^{\mathrm{i}\omega_{\nu lm}t}\, \langle n'l'm'|\nu lm\rangle\, \langle \nu lm|nlm\rangle\, \delta_{ll''}\delta_{mm''} \\
&= n(\varepsilon_{n'lm})\, \mathrm{e}^{-\mathrm{i}\varepsilon_{n'lm}t}\delta_{ll'}\delta_{mm'} \sum_{\nu} \mathrm{e}^{\mathrm{i}\omega_{\nu lm}t}\, \langle n'lm|\nu\, lm\rangle\, \underbrace{\langle \nu lm|nlm\rangle}_{=(**)} .
\end{aligned} \tag{B.14}$$

$(**)$ = overlaps of the free and full states (as the angular parts are equal this is given solely by the overlap of the respective radial wave functions)

This allows then to evaluate Eq. (B.13) and to obtain the absorption spectrum $A(\omega)$ by a Fourier transformation

$$A(\omega) = \frac{1}{2\pi} \int_{-\infty}^{\infty} \mathrm{d}t\, S(t)\, \mathrm{e}^{-\mathrm{i}\omega t} . \tag{B.15}$$

C. Discrete Variable Representation (DVR)

In order to numerically calculate eingenvalues and eigenstates of a given Hamiltonian typically a concrete choice of basis functions is needed for the matrix representation of the Hamiltonian. Here we present details on the choice of the basis functions used in Section 3.2 to represent the three-body Hamiltonian numerically allowing for its diagonalization. Thereby we summarize and follow the discussion given in [88] and [71].

First we consider an infinite set of square-integrable basis functions $\{\varphi_j(x)\}_{j=1}^{\infty}$. Each pair φ_j and φ_k allows to analytically evaluate the matrix elements

$$\begin{aligned} Q_{jk} &= \langle\varphi_j|\,\hat{x}\,|\varphi_k\rangle \ , \\ D^{(1)}_{jk} &= \langle\varphi_j|\,\frac{\mathrm{d}}{\mathrm{d}x}\,|\varphi_k\rangle \ , \\ D^{(2)}_{jk} &= \langle\varphi_j|\,\frac{\mathrm{d}^2}{\mathrm{d}x^2}\,|\varphi_k\rangle \ , \end{aligned} \tag{C.1}$$

that usually appear in a typically Hamiltonian. Here it is convenient to also assume square-integrability of $x\,\varphi_j(x)$ and $\mathrm{d}/\mathrm{d}x\,\varphi_j(x)$.

In the following we will investigate the truncated basis $\{\varphi_j(x)\}_{j=1}^{N}$ formed by the first N functions. The projector

$$\hat{P} = \sum_{j=1}^{N} |\varphi_j\rangle\,\langle\varphi_j| \tag{C.2}$$

projects any state on the subspace spanned by the truncated basis. Further we define the matrices[1] $\boldsymbol{Q}$, $\boldsymbol{D}^{(1)}$ and $\boldsymbol{D}^{(2)}$ acting on this subspace by allowing only $j,k \leq N$ in Eq. (C.1).

If the potential energy is the expectation value of an operator that itself is a function of the position operator $\hat{x}$, i.e.,

$$\hat{V} = V(\hat{x}) \ , \tag{C.3}$$

there are two different ways of approximately representing $\hat{V}$. The matrix can be defined in the truncated basis via the matrix elements

$$V^{\mathrm{VBR}}_{jk} = \langle\varphi_j|\,\hat{V}\,|\varphi_k\rangle \ , \tag{C.4}$$

[1] Note, in the following matrices will be labeled by bold capital latin letters.

with $j, k \leq N$ or as a function of the matrix representing the position operator in the truncated basis, i.e.,

$$\boldsymbol{V}^{\mathrm{FBR}} = V(\boldsymbol{Q}) \ . \tag{C.5}$$

Here VBR refers to 'variational basis-set representation' and FBR refers to 'finite basis-set representation'. Note that $\boldsymbol{V}^{\mathrm{FBR}}$ may have components that are outside of the subspace spanned by the truncated basis and that $\boldsymbol{V}^{\mathrm{VBR}} = \boldsymbol{V}^{\mathrm{FBR}}$ in general only holds in the limit $N \to \infty$, where both representations are exact.

The Hamiltonian

$$\hat{H} = \hat{T} + \hat{V} \tag{C.6}$$

can be approximated using either of the approximate representations and the resulting bound state energies represent upper bounds to the exact (infinite dimensional) problem.

In general the evaluation of the matrix elements V_{jk}^{VBR} is complicated, whereas the $\boldsymbol{V}^{\mathrm{FBR}}$ is easier to handle as $\boldsymbol{Q}$ is diagonalizable

$$\boldsymbol{Q} = \boldsymbol{U}\,\boldsymbol{X}\,\boldsymbol{U}^{\dagger} \ . \tag{C.7}$$

Here $\boldsymbol{X} = \mathrm{diag}(x_1, x_2, ...x_N)$ is the diagonalized matrix, where x_α are the eigenvalues of $\boldsymbol{Q}$ and $\boldsymbol{U}$ is the matrix containing the respective eigenvectors $|u_\alpha\rangle$. Consequently the matrix $\boldsymbol{V}^{\mathrm{FBR}}$ is obtained as

$$\boldsymbol{V}^{\mathrm{FBR}} = V(\boldsymbol{Q}) = \boldsymbol{U}\,V(\boldsymbol{X})\,\boldsymbol{U}^{\dagger} = \boldsymbol{U}\,\mathrm{diag}\big(V(x_1), V(x_2), ..., V(x_N)\big)\,\boldsymbol{U}^{\dagger} \ , \tag{C.8}$$

or element-wise

$$V_{jk}^{\mathrm{FBR}} = \sum_{\alpha=1}^{N} U_{j\alpha} V(x_\alpha) U_{k\alpha}^{*} \ . \tag{C.9}$$

The *discrete variable representation* (DVR) basis is now the basis in which the potential energy operator's matrix representation is diagonal, i.e.,

$$\begin{aligned} \boldsymbol{V}^{\mathrm{DVR}} =& \boldsymbol{U}^{\dagger}\,\boldsymbol{V}^{\mathrm{FBR}}\,\boldsymbol{U} = \boldsymbol{U}^{\dagger}\boldsymbol{U}\,V(\boldsymbol{X})\,\boldsymbol{U}^{\dagger}\boldsymbol{U} = V(\boldsymbol{X}) \\ =& \mathrm{diag}\big(V(x_1), V(x_2), ..., V(x_N)\big) \ . \end{aligned} \tag{C.10}$$

Here the eigenvalues x_α of the position operator $\boldsymbol{Q}$ appear as lattice sites on which the potential is evaluated. The corresponding basis is spanned by superpositions of the truncated basis functions, i.e., $\{\varphi_j(x)\}_{j=1}^{N}$, where the weights are given by the matrix elements of the unitary transformation $\boldsymbol{U}$

$$|\chi_\alpha(x)\rangle = \sum_{\alpha=1}^{N} \varphi_j(x) U_{j\alpha} \ . \tag{C.11}$$

To obtain the numerical results in Section 3.2 we use 11 Laguerre functions φ_j in each radial direction and seven in the angular direction.

D. Details: Real Space Interaction Term

Here we provide details of the conversion of the interaction term in Eq. (4.1) from real space to momentum space. The interactions in real space are given by

$$\hat{H}_{\text{int}} = g \iint \mathrm{d}^2\boldsymbol{r}_X \, \mathrm{d}^2\boldsymbol{r}_h \, \tilde{\chi}(\boldsymbol{r}_X - \boldsymbol{r}_h) \, \hat{t}^\dagger\!\left(\frac{m_X \boldsymbol{r}_X + m_h \boldsymbol{r}_h}{M}\right) \hat{X}(\boldsymbol{r}_X) \, \hat{h}(\boldsymbol{r}_h) + \text{h.c.} \,, \tag{D.1}$$

with the total mass $M = m_X + m_h$ and the field operators $\hat{t}(\boldsymbol{r})$, $\hat{X}(\boldsymbol{r})$ and $\hat{h}(\boldsymbol{r})$ of trions, excitons and holes. In contrast to the discussion in Chapter 4 we here suppress the layer index s of holes and trions to improve the clarity of the presentation. We use the conventions

$$\begin{aligned} \hat{\psi}(\boldsymbol{r}) &= \frac{1}{\sqrt{A}} \sum_{\boldsymbol{k}} \mathrm{e}^{\mathrm{i}\boldsymbol{k}\,\boldsymbol{r}} \, \hat{c}_{\boldsymbol{k}} \\ \hat{c}_{\boldsymbol{k}} &= \int \frac{\mathrm{d}^2\boldsymbol{r}}{\sqrt{A}} \, \mathrm{e}^{-\mathrm{i}\boldsymbol{k}\,\boldsymbol{r}} \, \hat{\psi}(\boldsymbol{r}) \,. \end{aligned} \tag{D.2}$$

This allows to express $\hat{H}_{\text{int}}$ in momentum space

$$\hat{H}_{\text{int}} = g \iint \mathrm{d}^2\boldsymbol{r}_X \, \mathrm{d}^2\boldsymbol{r}_h \, \tilde{\chi}(\boldsymbol{r}_X - \boldsymbol{r}_h) \, \frac{1}{\sqrt{A^3}} \sum_{\boldsymbol{p}\,\boldsymbol{k}\,\boldsymbol{q}} \mathrm{e}^{-\mathrm{i}\boldsymbol{p}\frac{m_X \boldsymbol{r}_X + m_h \boldsymbol{r}_h}{M}} \, \hat{t}^\dagger_{\boldsymbol{p}} \, \mathrm{e}^{\mathrm{i}\boldsymbol{k}\,\boldsymbol{r}_X} \hat{X}_{\boldsymbol{k}} \, \mathrm{e}^{\mathrm{i}\boldsymbol{q}\,\boldsymbol{r}_h} \hat{h}_{\boldsymbol{q}} + \text{h.c.} \,, \tag{D.3}$$

which can be transformed into relative and center of mass coordinates

$$\begin{aligned} \boldsymbol{R} &= \frac{m_X \boldsymbol{r}_X + m_h \boldsymbol{r}_h}{M} \,, \\ \boldsymbol{r} &= \boldsymbol{r}_X - \boldsymbol{r}_h \,, \end{aligned} \tag{D.4}$$

leading to

$$\begin{aligned} \hat{H}_{\text{int}} &= g \iint \mathrm{d}^2\boldsymbol{r} \, \mathrm{d}^2\boldsymbol{R} \, \tilde{\chi}(\boldsymbol{r}) \, \frac{1}{\sqrt{A^3}} \sum_{\boldsymbol{p}\,\boldsymbol{k}\,\boldsymbol{q}} \hat{t}^\dagger_{\boldsymbol{p}} \, \hat{X}_{\boldsymbol{k}} \, \hat{h}_{\boldsymbol{q}} \, \mathrm{e}^{-\mathrm{i}\boldsymbol{p}\boldsymbol{R}} \, \mathrm{e}^{\mathrm{i}\boldsymbol{k}\,(\boldsymbol{R} + m_h/M\,\boldsymbol{r})} \, \mathrm{e}^{\mathrm{i}\,\boldsymbol{q}\,(\boldsymbol{R} - m_x/M\,\boldsymbol{r})} + \text{h.c.} \\ &= g \iint \mathrm{d}^2\boldsymbol{r} \, \mathrm{d}^2\boldsymbol{R} \, \tilde{\chi}(\boldsymbol{r}) \, \frac{1}{\sqrt{A^3}} \sum_{\boldsymbol{p}\,\boldsymbol{k}\,\boldsymbol{q}} \hat{t}^\dagger_{\boldsymbol{p}} \, \hat{X}_{\boldsymbol{k}} \, \hat{h}_{\boldsymbol{q}} \, \mathrm{e}^{-\mathrm{i}\boldsymbol{R}\,(\boldsymbol{p} - \boldsymbol{k} - \boldsymbol{q})} \, \mathrm{e}^{\mathrm{i}\boldsymbol{r}\,(\boldsymbol{k}\,m_h/M - \boldsymbol{q}\,m_X/M)} + \text{h.c.} \\ &= g \int \mathrm{d}^2\boldsymbol{r} \, \tilde{\chi}(\boldsymbol{r}) \, \frac{1}{\sqrt{A}} \sum_{\boldsymbol{p}\,\boldsymbol{k}\,\boldsymbol{q}} \delta_{\boldsymbol{p},\boldsymbol{k}+\boldsymbol{q}} \, \hat{t}^\dagger_{\boldsymbol{p}} \, \hat{X}_{\boldsymbol{k}} \, \hat{h}_{\boldsymbol{q}} \, \mathrm{e}^{\mathrm{i}\boldsymbol{r}\,(\boldsymbol{k}\,m_h/M - \boldsymbol{q}\,m_X/M)} + \text{h.c.} \,, \end{aligned} \tag{D.5}$$

where we used

$$\delta_{\boldsymbol{p},\boldsymbol{q}} = \frac{1}{A}\int \mathrm{d}^2\boldsymbol{r}\, \mathrm{e}^{\pm \mathrm{i}\boldsymbol{r}(\boldsymbol{p}-\boldsymbol{q})} \ . \tag{D.6}$$

Making use of the definition of the Fourier transform

$$\chi(\boldsymbol{k}) = \frac{1}{\sqrt{A}}\int \mathrm{d}^2\boldsymbol{r}\, \mathrm{e}^{-\mathrm{i}\boldsymbol{r}\,\boldsymbol{k}}\, \tilde{\chi}(\boldsymbol{r}) \ , \tag{D.7}$$

we find the interaction term in momentum space

$$\hat{H}_{\mathrm{int}} = g\sum_{\boldsymbol{k}\,\boldsymbol{q}} \chi\Big(\frac{m_h}{M}\boldsymbol{q} - \frac{m_x}{M}\,\boldsymbol{k}\Big)\, \hat{t}^{\dagger}_{\boldsymbol{k}+\boldsymbol{q}}\, \hat{X}_{\boldsymbol{k}}\, \hat{h}_{\boldsymbol{q}} + \mathrm{h.c.} \ , \tag{D.8}$$

as used in Eq. (4.1).

E. Details: Calculation of the ULRRM-Dimer Absorption Strength

Here we provide additional information for the calculation presented in Chapter 6.

E.1. Normalization of the Approximate ULRRM Final States

Here we calculate the norm of a δ-peaked final state, i.e.,

$$\begin{aligned} |\mathrm{f}\rangle &= \frac{V}{\sqrt{2}} \int \mathrm{d}^3\boldsymbol{R} \int \mathrm{d}^3\boldsymbol{r}\; \delta^{(3)}\big(\boldsymbol{R}-\boldsymbol{R}_\mathrm{C}\big)\, \delta^{(3)}\big(\boldsymbol{r}-\boldsymbol{r}_\mathrm{D}\big)\, \hat{d}^\dagger_{\boldsymbol{R}-\frac{\boldsymbol{r}}{2}}\, \hat{c}^\dagger_{\boldsymbol{R}+\frac{\boldsymbol{r}}{2}}\, \hat{c}_{\boldsymbol{p}}\, \hat{c}_{\boldsymbol{p}'}\, |\mathrm{FS}_c\rangle \\ &= \frac{V}{\sqrt{2}}\, \hat{d}^\dagger_{\boldsymbol{R}_\mathrm{C}-\frac{\boldsymbol{r}_\mathrm{D}}{2}}\, \hat{c}^\dagger_{\boldsymbol{R}_\mathrm{C}+\frac{\boldsymbol{r}_\mathrm{D}}{2}}\, \hat{c}_{\boldsymbol{p}}\, \hat{c}_{\boldsymbol{p}'}\, |\mathrm{FS}_c\rangle \ . \end{aligned} \tag{E.1}$$

From this state we obtain

$$\begin{aligned} \langle\, \mathrm{f}\,|\,\mathrm{f}\,\rangle &= \frac{V^2}{2}\, \langle \mathrm{FS}_c|\, \hat{c}^\dagger_{\boldsymbol{p}'}\, \hat{c}^\dagger_{\boldsymbol{p}} \hat{c}_{\boldsymbol{R}_\mathrm{C}+\frac{\boldsymbol{r}_\mathrm{D}}{2}}\, \hat{d}_{\boldsymbol{R}_\mathrm{C}-\frac{\boldsymbol{r}_\mathrm{D}}{2}}\, \hat{d}^\dagger_{\boldsymbol{R}_\mathrm{C}-\frac{\boldsymbol{r}_\mathrm{D}}{2}}\, \hat{c}^\dagger_{\boldsymbol{R}_\mathrm{C}+\frac{\boldsymbol{r}_\mathrm{D}}{2}}\, \hat{c}_{\boldsymbol{p}}\, \hat{c}_{\boldsymbol{p}'}\, |\mathrm{FS}_c\rangle \\ &= \frac{V^2}{2}\, \langle \mathrm{FS}_c|\, \hat{c}^\dagger_{\boldsymbol{p}'}\, \hat{c}^\dagger_{\boldsymbol{p}} \hat{c}_{\boldsymbol{R}_\mathrm{C}+\frac{\boldsymbol{r}_\mathrm{D}}{2}}\, \hat{c}^\dagger_{\boldsymbol{R}_\mathrm{C}+\frac{\boldsymbol{r}_\mathrm{D}}{2}}\, \hat{c}_{\boldsymbol{p}}\, \hat{c}_{\boldsymbol{p}'}\, |\mathrm{FS}_c\rangle\, \langle 0_d|\, \hat{d}_{\boldsymbol{R}_\mathrm{C}-\frac{\boldsymbol{r}_\mathrm{D}}{2}}\, \hat{d}^\dagger_{\boldsymbol{R}_\mathrm{C}-\frac{\boldsymbol{r}_\mathrm{D}}{2}}\, |0_d\rangle \\ &= \frac{V^2}{2}\, \langle \mathrm{FS}_c|\, \hat{c}^\dagger_{\boldsymbol{p}'}\, \hat{c}^\dagger_{\boldsymbol{p}}\, \frac{1}{V} \sum_{kq}^{\infty} \mathrm{e}^{\mathrm{i}(\boldsymbol{R}_\mathrm{C}+\frac{\boldsymbol{r}_\mathrm{D}}{2})\boldsymbol{k}}\, \mathrm{e}^{-\mathrm{i}(\boldsymbol{R}_\mathrm{C}+\frac{\boldsymbol{r}_\mathrm{D}}{2})\boldsymbol{q}} \hat{c}_{\boldsymbol{k}}\, \hat{c}^\dagger_{\boldsymbol{q}}\, \hat{c}_{\boldsymbol{p}}\, \hat{c}_{\boldsymbol{p}'}\, |\mathrm{FS}_c\rangle \\ &\qquad\qquad \times \langle 0|_d\, \hat{d}_{\boldsymbol{R}_\mathrm{C}-\frac{\boldsymbol{r}_\mathrm{D}}{2}}\, \hat{d}^\dagger_{\boldsymbol{R}_\mathrm{C}-\frac{\boldsymbol{r}_\mathrm{D}}{2}}\, |0\rangle_d \\ &= \frac{V}{2} \sum_{kq} \mathrm{e}^{\mathrm{i}(\boldsymbol{R}_\mathrm{C}+\frac{\boldsymbol{r}_\mathrm{D}}{2})(\boldsymbol{k}-\boldsymbol{q})}\, \langle \mathrm{FS}_c|\, \hat{c}^\dagger_{\boldsymbol{p}'}\, \hat{c}^\dagger_{\boldsymbol{p}}\, \hat{c}_{\boldsymbol{k}}\, \hat{c}^\dagger_{\boldsymbol{q}}\, \hat{c}_{\boldsymbol{p}}\, \hat{c}_{\boldsymbol{p}'}\, |\mathrm{FS}_c\rangle \\ &\qquad\qquad \times \underbrace{\delta^{(3)}\Big(\boldsymbol{R}_\mathrm{C}-\frac{\boldsymbol{r}_\mathrm{D}}{2}-\Big(\boldsymbol{R}_\mathrm{C}-\frac{\boldsymbol{r}_\mathrm{D}}{2}\Big)\Big)}_{\delta^{(3)}(0)=1/V} \ . \end{aligned} \tag{E.2}$$

Now we consider the expression

$$\begin{aligned}
&\langle \mathrm{FS}_c |\, \hat{c}^\dagger_{\boldsymbol{p}'}\, \hat{c}^\dagger_{\boldsymbol{p}} \hat{c}_{\boldsymbol{k}}\, \hat{c}^\dagger_{\boldsymbol{q}}\, \hat{c}_{\boldsymbol{p}}\, \hat{c}_{\boldsymbol{p}'} \,| \mathrm{FS}_c \rangle \\
&\qquad = \langle \mathrm{FS}_c |\, \hat{c}^\dagger_{\boldsymbol{p}'}\, \hat{c}^\dagger_{\boldsymbol{p}} \hat{c}_{\boldsymbol{k}}\, (\delta_{\boldsymbol{qp}} - \hat{c}_{\boldsymbol{p}}\, \hat{c}^\dagger_{\boldsymbol{q}}) \hat{c}_{\boldsymbol{p}'} \,| \mathrm{FS}_c \rangle \\
&\qquad = \delta_{\boldsymbol{qp}} \langle \mathrm{FS}_c |\, \hat{c}^\dagger_{\boldsymbol{p}'}\, \hat{c}^\dagger_{\boldsymbol{p}} \hat{c}_{\boldsymbol{k}}\, \hat{c}_{\boldsymbol{p}'} \,| \mathrm{FS}_c \rangle - \langle \mathrm{FS}_c |\, \hat{c}^\dagger_{\boldsymbol{p}'}\, \hat{c}^\dagger_{\boldsymbol{p}} \hat{c}_{\boldsymbol{k}}\, \hat{c}_{\boldsymbol{p}}\, \hat{c}^\dagger_{\boldsymbol{q}} \hat{c}_{\boldsymbol{p}'} \,| \mathrm{FS}_c \rangle \\
&\qquad = \delta_{\boldsymbol{qp}} \Big(\delta_{\boldsymbol{p}'\boldsymbol{p}'} \delta_{\boldsymbol{pk}} - \delta_{\boldsymbol{pp}'} \delta_{\boldsymbol{p}'\boldsymbol{k}} \Big) - \langle \mathrm{FS}_c |\, \hat{c}^\dagger_{\boldsymbol{p}'}\, \hat{c}^\dagger_{\boldsymbol{p}} \hat{c}_{\boldsymbol{k}}\, \hat{c}_{\boldsymbol{p}}\, (\delta_{\boldsymbol{qp}'} - \hat{c}_{\boldsymbol{p}'}\, \hat{c}^\dagger_{\boldsymbol{q}}) \,| \mathrm{FS}_c \rangle \\
&\qquad = \delta_{\boldsymbol{qp}} \Big(\delta_{\boldsymbol{p}'\boldsymbol{p}'} \delta_{\boldsymbol{pk}} - \delta_{\boldsymbol{pp}'} \delta_{\boldsymbol{p}'\boldsymbol{k}} \Big) - \delta_{\boldsymbol{qp}'} \langle \mathrm{FS}_c |\, \hat{c}^\dagger_{\boldsymbol{p}'}\, \hat{c}^\dagger_{\boldsymbol{p}} \hat{c}_{\boldsymbol{k}}\, \hat{c}_{\boldsymbol{p}} \,| \mathrm{FS}_c \rangle \\
&\qquad = \delta_{\boldsymbol{qp}} \Big(\delta_{\boldsymbol{p}'\boldsymbol{p}'} \delta_{\boldsymbol{pk}} - \delta_{\boldsymbol{pp}'} \delta_{\boldsymbol{p}'\boldsymbol{k}} \Big) - \delta_{\boldsymbol{qp}'} \Big(\delta_{\boldsymbol{p}'\boldsymbol{p}} \delta_{\boldsymbol{pk}} - \delta_{\boldsymbol{pp}} \delta_{\boldsymbol{p}'\boldsymbol{k}} \Big) \\
&\qquad = \delta_{\boldsymbol{qp}} \Big(\delta_{\boldsymbol{pk}} - \delta_{\boldsymbol{pp}'} \delta_{\boldsymbol{p}'\boldsymbol{k}} \Big) - \delta_{\boldsymbol{qp}'} \Big(\delta_{\boldsymbol{p}'\boldsymbol{p}} \delta_{\boldsymbol{pk}} - \delta_{\boldsymbol{p}'\boldsymbol{k}} \Big) \\
&\qquad = \delta_{\boldsymbol{qp}} \delta_{\boldsymbol{pk}} + \delta_{\boldsymbol{qp}'} \delta_{\boldsymbol{p}'\boldsymbol{k}} \ ,
\end{aligned} \tag{E.3}$$

where we used that the case $\boldsymbol{p} = \boldsymbol{p}'$ can be neglected as it implies $|\mathrm{f}\rangle = 0$. Making use of this result in Eq. (E.2) we find

$$\begin{aligned}
\langle \mathrm{f} \,|\, \mathrm{f} \rangle &= \frac{V}{2} \sum_{kq} \mathrm{e}^{\mathrm{i}(\boldsymbol{R}_\mathrm{C} + \frac{\boldsymbol{r}_\mathrm{D}}{2})(\boldsymbol{k}-\boldsymbol{q})} \ \langle \mathrm{FS}_c |\, \hat{c}^\dagger_{\boldsymbol{p}'}\, \hat{c}^\dagger_{\boldsymbol{p}}\, \hat{c}_{\boldsymbol{k}}\, \hat{c}^\dagger_{\boldsymbol{q}}\, \hat{c}_{\boldsymbol{p}}\, \hat{c}_{\boldsymbol{p}'} \,| \mathrm{FS}_c \rangle \\
&\qquad\qquad \times \underbrace{\delta^{(3)}\Big(\boldsymbol{R}_\mathrm{C} - \frac{\boldsymbol{r}_\mathrm{D}}{2} - \Big(\boldsymbol{R}_\mathrm{C} - \frac{\boldsymbol{r}_\mathrm{D}}{2}\Big)\Big)}_{\delta^{(3)}(0) = 1/V} \\
&= \frac{1}{2} \sum_{kq} \mathrm{e}^{\mathrm{i}(\boldsymbol{R}_\mathrm{C} + \frac{\boldsymbol{r}_\mathrm{D}}{2})(\boldsymbol{k}-\boldsymbol{q})} \Big(\delta_{\boldsymbol{qp}} \delta_{\boldsymbol{pk}} + \delta_{\boldsymbol{qp}'} \delta_{\boldsymbol{p}'\boldsymbol{k}} \Big) \\
&= \frac{1}{2} \Big(\mathrm{e}^{\mathrm{i}(\boldsymbol{R}_\mathrm{C} + \frac{\boldsymbol{r}_\mathrm{D}}{2})(\boldsymbol{p}-\boldsymbol{p})} + \mathrm{e}^{\mathrm{i}(\boldsymbol{R}_\mathrm{C} + \frac{\boldsymbol{r}_\mathrm{D}}{2})(\boldsymbol{p}'-\boldsymbol{p}')} \Big) \\
&= 1 \ .
\end{aligned} \tag{E.4}$$

This also holds true for a final state

$$|\mathrm{f}\rangle = \int \mathrm{d}^3\boldsymbol{R} \int \mathrm{d}^3\boldsymbol{r}\, \Psi_{\boldsymbol{\lambda},\boldsymbol{\alpha}}(\boldsymbol{R}, \boldsymbol{r})\, \hat{d}^\dagger_{\boldsymbol{R}-\frac{\boldsymbol{r}}{2}}\, \hat{c}^\dagger_{\boldsymbol{R}+\frac{\boldsymbol{r}}{2}}\, \hat{c}_{\boldsymbol{p}}\, \hat{c}_{\boldsymbol{p}'} \,|\mathrm{i}\rangle \ , \tag{E.5}$$

which normalization condition reduces to

$$\iint \mathrm{d}^3\boldsymbol{R}\, \mathrm{d}^3\boldsymbol{r}\, |\Psi_{\boldsymbol{\lambda},\boldsymbol{\alpha}}(\boldsymbol{R}, \boldsymbol{r})|^2 = 1 \ . \tag{E.6}$$

E.2. Derivation of a Useful Relation

Here we derive Eq. (6.13). We again use the definition of the field operator

$$\hat{c}_{\boldsymbol{r}} = \frac{1}{\sqrt{V}} \sum_{\boldsymbol{k}} \mathrm{e}^{\mathrm{i}\boldsymbol{r}\boldsymbol{k}} \hat{c}_{\boldsymbol{k}} \ , \tag{E.7}$$

and investigate the expression B defined in Eq. (6.12)

$$\begin{aligned} B &= \sum_{\boldsymbol{p},\boldsymbol{p}'} \hat{c}_{\boldsymbol{p}}\, \hat{c}_{\boldsymbol{p}'} \left|\mathrm{FS}_c\right\rangle \left\langle \mathrm{FS}_c\right| \hat{c}^\dagger_{\boldsymbol{p}'}\, \hat{c}^\dagger_{\boldsymbol{p}} \hat{c}_{\boldsymbol{R}+\frac{\boldsymbol{r}}{2}}\, \hat{c}_{\boldsymbol{R}-\frac{\boldsymbol{r}}{2}} \left|\mathrm{FS}_c\right\rangle \\ &= \sum_{\boldsymbol{p},\boldsymbol{p}'} \hat{c}_{\boldsymbol{p}}\, \hat{c}_{\boldsymbol{p}'} \left|\mathrm{FS}_c\right\rangle \left\langle \mathrm{FS}_c\right| \hat{c}^\dagger_{\boldsymbol{p}'}\, \hat{c}^\dagger_{\boldsymbol{p}}\, \frac{1}{V} \sum_{\boldsymbol{k},\boldsymbol{q}} \mathrm{e}^{\mathrm{i}\boldsymbol{q}(\boldsymbol{R}+\frac{\boldsymbol{r}}{2})}\, \mathrm{e}^{\mathrm{i}\boldsymbol{k}(\boldsymbol{R}-\frac{\boldsymbol{r}}{2})} \hat{c}_{\boldsymbol{q}}\, \hat{c}_{\boldsymbol{k}} \left|\mathrm{FS}_c\right\rangle \\ &= \sum_{\boldsymbol{p},\boldsymbol{p}'} \frac{1}{V} \sum_{\boldsymbol{q},\boldsymbol{k}} \mathrm{e}^{\mathrm{i}\boldsymbol{q}(\boldsymbol{R}+\frac{\boldsymbol{r}}{2})}\, \mathrm{e}^{\mathrm{i}\boldsymbol{k}(\boldsymbol{R}-\frac{\boldsymbol{r}}{2})} \hat{c}_{\boldsymbol{p}}\, \hat{c}_{\boldsymbol{p}'} \left|\mathrm{FS}_c\right\rangle \left\langle \mathrm{FS}_c\right| \hat{c}^\dagger_{\boldsymbol{p}'}\, \hat{c}^\dagger_{\boldsymbol{p}}\, \hat{c}_{\boldsymbol{q}}\, \hat{c}_{\boldsymbol{k}} \left|\mathrm{FS}_c\right\rangle \ . \end{aligned} \tag{E.8}$$

Now we consider the expectation value of momentum creation and annihilation operators with respect to the Fermi sea and find

$$\begin{aligned} \left\langle \mathrm{FS}_c\right| \hat{c}^\dagger_{\boldsymbol{p}'}\, \hat{c}^\dagger_{\boldsymbol{p}}\, \hat{c}_{\boldsymbol{q}}\, \hat{c}_{\boldsymbol{k}} \left|\mathrm{FS}_c\right\rangle &= \left\langle \mathrm{FS}_c\right| \hat{c}^\dagger_{\boldsymbol{p}'}\, (\delta_{\boldsymbol{p}\boldsymbol{q}} - \hat{c}_{\boldsymbol{q}}\, \hat{c}^\dagger_{\boldsymbol{p}})\hat{c}_{\boldsymbol{k}} \left|\mathrm{FS}_c\right\rangle \\ &= \left\langle \mathrm{FS}_c\right| (\delta_{\boldsymbol{p}'\boldsymbol{k}} - \hat{c}_{\boldsymbol{k}}\, \hat{c}^\dagger_{\boldsymbol{p}'})\delta_{\boldsymbol{p}\boldsymbol{q}} - \hat{c}^\dagger_{\boldsymbol{p}'}\, \hat{c}_{\boldsymbol{q}}\, \hat{c}^\dagger_{\boldsymbol{p}}\, \hat{c}_{\boldsymbol{k}} \left|\mathrm{FS}_c\right\rangle \\ &= \left\langle \mathrm{FS}_c\right| \delta_{\boldsymbol{p}'\boldsymbol{k}}\delta_{\boldsymbol{p}\boldsymbol{q}} - (\delta_{\boldsymbol{p}'\boldsymbol{q}} - \hat{c}_{\boldsymbol{q}}\, \hat{c}^\dagger_{\boldsymbol{p}'})(\delta_{\boldsymbol{p}\boldsymbol{k}} - \hat{c}_{\boldsymbol{k}}\, \hat{c}^\dagger_{\boldsymbol{p}}) \left|\mathrm{FS}_c\right\rangle \\ &= \delta_{\boldsymbol{p}'\boldsymbol{k}}\delta_{\boldsymbol{p}\boldsymbol{q}} - \delta_{\boldsymbol{p}'\boldsymbol{q}}\delta_{\boldsymbol{p}\boldsymbol{k}} \ . \end{aligned} \tag{E.9}$$

Using this relation in Eq. (E.8) we obtain

$$\begin{aligned} B &= \sum_{\boldsymbol{p},\boldsymbol{p}'} \frac{1}{V} \sum_{\boldsymbol{q},\boldsymbol{k}} \mathrm{e}^{\mathrm{i}\boldsymbol{q}(\boldsymbol{R}+\frac{\boldsymbol{r}}{2})}\, \mathrm{e}^{\mathrm{i}\boldsymbol{k}(\boldsymbol{R}-\frac{\boldsymbol{r}}{2})} \hat{c}_{\boldsymbol{p}}\, \hat{c}_{\boldsymbol{p}'} \left|\mathrm{FS}_c\right\rangle \Big(\delta_{\boldsymbol{p}'\boldsymbol{k}}\delta_{\boldsymbol{p}\boldsymbol{q}} - \delta_{\boldsymbol{p}'\boldsymbol{q}}\delta_{\boldsymbol{p}\boldsymbol{k}}\Big) \\ &= \frac{1}{V} \sum_{\boldsymbol{p},\boldsymbol{p}'} \Big(\mathrm{e}^{\mathrm{i}\boldsymbol{p}(\boldsymbol{R}+\frac{\boldsymbol{r}}{2})}\, \mathrm{e}^{\mathrm{i}\boldsymbol{p}'(\boldsymbol{R}-\frac{\boldsymbol{r}}{2})} - \mathrm{e}^{\mathrm{i}\boldsymbol{p}(\boldsymbol{R}-\frac{\boldsymbol{r}}{2})}\, \mathrm{e}^{\mathrm{i}\boldsymbol{p}'(\boldsymbol{R}+\frac{\boldsymbol{r}}{2})}\Big) \hat{c}_{\boldsymbol{p}}\, \hat{c}_{\boldsymbol{p}'} \left|\mathrm{FS}_c\right\rangle \\ &= \Big(\hat{c}_{\boldsymbol{R}+\frac{\boldsymbol{r}}{2}}\, \hat{c}_{\boldsymbol{R}-\frac{\boldsymbol{r}}{2}} - \hat{c}_{\boldsymbol{R}-\frac{\boldsymbol{r}}{2}}\, \hat{c}_{\boldsymbol{R}+\frac{\boldsymbol{r}}{2}}\Big) \left|\mathrm{FS}_c\right\rangle \\ &= 2\, \hat{c}_{\boldsymbol{R}+\frac{\boldsymbol{r}}{2}}\, \hat{c}_{\boldsymbol{R}-\frac{\boldsymbol{r}}{2}} \left|\mathrm{FS}_c\right\rangle \ , \end{aligned} \tag{E.10}$$

which is the statement of Eq. (6.13). In the last step we made use the anti-commutation relations for $\hat{c}_{\boldsymbol{x}}\, \hat{c}_{\boldsymbol{x}'}$.

E.3. Extension to Single Fock States

Again we look at the expression B (c.f. Eq. (6.13)) now with Fock states

$$|\mathrm{F}\rangle = \prod_{i=1}^{\infty} \left(\hat{c}^\dagger_{\boldsymbol{k}_i}\right)^{n_i} |0\rangle = |n_1, n_2, \dots, n_i, \dots, n_\infty\rangle \ , \tag{E.11}$$

as initial states, i.e.,

$$\begin{aligned}
B &= \sum_{\boldsymbol{p},\boldsymbol{p}'} \hat{c}_{\boldsymbol{p}}\, \hat{c}_{\boldsymbol{p}'}\, |\mathrm{F}\rangle \langle \mathrm{F}|\, \hat{c}^\dagger_{\boldsymbol{p}'}\, \hat{c}^\dagger_{\boldsymbol{p}}\, \hat{c}_{\boldsymbol{R}+\frac{\boldsymbol{r}}{2}}\, \hat{c}_{\boldsymbol{R}-\frac{\boldsymbol{r}}{2}}\, |\mathrm{F}\rangle \\
&= 2 \sum_{\boldsymbol{p}<\boldsymbol{p}'} \hat{c}_{\boldsymbol{p}}\, \hat{c}_{\boldsymbol{p}'}\, |\mathrm{F}\rangle \langle \mathrm{F}|\, \hat{c}^\dagger_{\boldsymbol{p}'}\, \hat{c}^\dagger_{\boldsymbol{p}}\, \hat{c}_{\boldsymbol{R}+\frac{\boldsymbol{r}}{2}}\, \hat{c}_{\boldsymbol{R}-\frac{\boldsymbol{r}}{2}}\, |\mathrm{F}\rangle \\
&= \frac{2}{V^2} \sum_{\boldsymbol{p}<\boldsymbol{p}'} \sum_{\tilde{\boldsymbol{p}},\tilde{\boldsymbol{p}}'} \hat{c}_{\boldsymbol{p}}\, \hat{c}_{\boldsymbol{p}'}\, |\mathrm{i}\rangle \langle 0| \prod_{i=1}^{\infty} \left(\hat{c}_{\boldsymbol{k}_i}\right)^{n_i^{\mathrm{F}}} \hat{c}^\dagger_{\boldsymbol{p}'}\, \hat{c}^\dagger_{\boldsymbol{p}} \\
&\qquad\qquad \times \mathrm{e}^{\mathrm{i}\tilde{\boldsymbol{p}}\cdot\left(\boldsymbol{R}+\frac{\boldsymbol{r}}{2}\right)}\, \mathrm{e}^{\mathrm{i}\tilde{\boldsymbol{p}}'\cdot\left(\boldsymbol{R}-\frac{\boldsymbol{r}}{2}\right)}\, c_{\tilde{\boldsymbol{p}}} c_{\tilde{\boldsymbol{p}}'} \prod_{i=1}^{\infty} \left(\hat{c}^\dagger_{\boldsymbol{k}_i}\right)^{n_i^{\mathrm{F}}} |0\rangle \\
&= \frac{2}{V^2} \sum_{\boldsymbol{p}<\boldsymbol{p}'} \sum_{\tilde{\boldsymbol{p}},\tilde{\boldsymbol{p}}'} n^{\mathrm{F}}_{\boldsymbol{p}} n^{\mathrm{F}}_{\boldsymbol{p}'}\, (-1)^{\sum\limits_{\boldsymbol{q}\le\boldsymbol{p}} n^{\mathrm{F}}_{\boldsymbol{q}}}\, (-1)^{\sum\limits_{\boldsymbol{q}\le\boldsymbol{p}'} n^{\mathrm{F}}_{\boldsymbol{q}}}\, \mathrm{e}^{\mathrm{i}\tilde{\boldsymbol{p}}\cdot\left(\boldsymbol{R}+\frac{\boldsymbol{r}}{2}\right)}\, \mathrm{e}^{\mathrm{i}\tilde{\boldsymbol{p}}'\cdot\left(\boldsymbol{R}-\frac{\boldsymbol{r}}{2}\right)}\, n^{\mathrm{F}}_{\tilde{\boldsymbol{p}}} n^{\mathrm{F}}_{\tilde{\boldsymbol{p}}'} \\
&\qquad\qquad \times (-1)^{\sum\limits_{\boldsymbol{q}\le\tilde{\boldsymbol{p}}} n^{\mathrm{F}}_{\boldsymbol{q}}}\, (-1)^{\sum\limits_{\boldsymbol{q}\le\tilde{\boldsymbol{p}}'} n^{\mathrm{F}}_{\boldsymbol{q}}}\, \hat{c}_{\boldsymbol{p}}\, \hat{c}_{\boldsymbol{p}'}\, |\mathrm{F}\rangle \underbrace{\langle 0| \prod_{\substack{j=1 \\ \boldsymbol{p}\neq\boldsymbol{k}_j\neq\boldsymbol{p}'}}^{\infty} \left(\hat{c}_{\boldsymbol{k}_j}\right)^{n_j^{\mathrm{F}}} \prod_{\substack{i=1 \\ \tilde{\boldsymbol{p}}\neq\boldsymbol{k}_i\neq\tilde{\boldsymbol{p}}'}}^{\infty} \left(\hat{c}^\dagger_{\boldsymbol{k}_i}\right)^{n_i^{\mathrm{F}}} |0\rangle}_{=\delta_{\boldsymbol{p}\tilde{\boldsymbol{p}}}\delta_{\boldsymbol{p}'\tilde{\boldsymbol{p}}'} - \delta_{\boldsymbol{p}\tilde{\boldsymbol{p}}'}\delta_{\boldsymbol{p}'\tilde{\boldsymbol{p}}}} \\
&= \frac{2}{V^2} \sum_{\boldsymbol{p}<\boldsymbol{p}'} n^{\mathrm{F}}_{\boldsymbol{p}} n^{\mathrm{F}}_{\boldsymbol{p}'} \left(\mathrm{e}^{\mathrm{i}\boldsymbol{p}\cdot\left(\boldsymbol{R}+\frac{\boldsymbol{r}}{2}\right)}\, \mathrm{e}^{\mathrm{i}\boldsymbol{p}'\cdot\left(\boldsymbol{R}-\frac{\boldsymbol{r}}{2}\right)} - \mathrm{e}^{\mathrm{i}\boldsymbol{p}'\cdot\left(\boldsymbol{R}+\frac{\boldsymbol{r}}{2}\right)}\, \mathrm{e}^{\mathrm{i}\boldsymbol{p}\cdot\left(\boldsymbol{R}-\frac{\boldsymbol{r}}{2}\right)}\right) \hat{c}_{\boldsymbol{p}}\, \hat{c}_{\boldsymbol{p}'}\, |\mathrm{F}\rangle \\
&= \frac{1}{V^2} \sum_{\boldsymbol{p},\boldsymbol{p}'} \left(\mathrm{e}^{\mathrm{i}\boldsymbol{p}\cdot\left(\boldsymbol{R}+\frac{\boldsymbol{r}}{2}\right)}\, \mathrm{e}^{\mathrm{i}\boldsymbol{p}'\cdot\left(\boldsymbol{R}-\frac{\boldsymbol{r}}{2}\right)} - \mathrm{e}^{\mathrm{i}\boldsymbol{p}'\cdot\left(\boldsymbol{R}+\frac{\boldsymbol{r}}{2}\right)}\, \mathrm{e}^{\mathrm{i}\boldsymbol{p}\cdot\left(\boldsymbol{R}-\frac{\boldsymbol{r}}{2}\right)}\right) \hat{c}_{\boldsymbol{p}}\, \hat{c}_{\boldsymbol{p}'}\, |\mathrm{F}\rangle \\
&= \frac{1}{V^2} \sum_{\boldsymbol{p},\boldsymbol{p}'} \left(\mathrm{e}^{\mathrm{i}\boldsymbol{p}\cdot\left(\boldsymbol{R}+\frac{\boldsymbol{r}}{2}\right)}\, \mathrm{e}^{\mathrm{i}\boldsymbol{p}'\cdot\left(\boldsymbol{R}-\frac{\boldsymbol{r}}{2}\right)} - \mathrm{e}^{\mathrm{i}\boldsymbol{p}'\cdot\left(\boldsymbol{R}+\frac{\boldsymbol{r}}{2}\right)}\, \mathrm{e}^{\mathrm{i}\boldsymbol{p}\cdot\left(\boldsymbol{R}-\frac{\boldsymbol{r}}{2}\right)}\right) \hat{c}_{\boldsymbol{p}}\, \hat{c}_{\boldsymbol{p}'}\, |\mathrm{F}\rangle \\
&= 2\, \hat{c}_{\boldsymbol{R}+\frac{\boldsymbol{r}}{2}}\, \hat{c}_{\boldsymbol{R}-\frac{\boldsymbol{r}}{2}}\, |\mathrm{F}\rangle \ .
\end{aligned} \tag{E.12}$$

This is the same result as in the Fermi sea scenario (see E.10).

E.4. Further Details on the Calculation of the ULRRM-Dimer Absorption Strength

Here we derive a function used in the evaluation of the ULRRM-dimer absorption strength (c.f. Eq. (6.24)) and start by calculating the expression

$$\begin{aligned}
\langle \mathrm{FS}_c |\, \hat{c}^\dagger_{\boldsymbol{r}_1}\, \hat{c}^\dagger_{\boldsymbol{r}_2}\, \hat{c}_{\boldsymbol{r}_3}\, \hat{c}_{\boldsymbol{r}_4}\, | \mathrm{FS}_c \rangle &= \frac{1}{V^2} \sum_{\boldsymbol{p}_1,\ldots,\boldsymbol{p}_4} \mathrm{e}^{-\mathrm{i}\boldsymbol{r}_1\,\cdot\,\boldsymbol{p}_1}\, \mathrm{e}^{-\mathrm{i}\boldsymbol{r}_2\,\cdot\,\boldsymbol{p}_2}\, \mathrm{e}^{\mathrm{i}\boldsymbol{r}_3\,\cdot\,\boldsymbol{p}_3}\, \mathrm{e}^{\mathrm{i}\boldsymbol{r}_4\,\cdot\,\boldsymbol{p}_4} \\
&\qquad \times \langle \mathrm{FS}_c |\, \hat{c}^\dagger_{\boldsymbol{p}_1}\, \hat{c}^\dagger_{\boldsymbol{p}_2}\, \hat{c}_{\boldsymbol{p}_3}\, \hat{c}_{\boldsymbol{p}_4}\, | \mathrm{FS}_c \rangle \\
&= \frac{1}{V^2} \sum_{\boldsymbol{p}_1,\ldots,\boldsymbol{p}_4}^{\leq k_\mathrm{F}} \mathrm{e}^{-\mathrm{i}\boldsymbol{r}_1\,\cdot\,\boldsymbol{p}_1}\, \mathrm{e}^{-\mathrm{i}\boldsymbol{r}_2\,\cdot\,\boldsymbol{p}_2}\, \mathrm{e}^{\mathrm{i}\boldsymbol{r}_3\,\cdot\,\boldsymbol{p}_3}\, \mathrm{e}^{\mathrm{i}\boldsymbol{r}_4\,\cdot\,\boldsymbol{p}_4} \\
&\qquad \times \left(\delta_{\boldsymbol{p}_1\boldsymbol{p}_4}\delta_{\boldsymbol{p}_2\boldsymbol{p}_3} - \delta_{\boldsymbol{p}_2\boldsymbol{p}_4}\delta_{\boldsymbol{p}_1\boldsymbol{p}_3}\right) \\
&= \frac{1}{V^2} \sum_{\boldsymbol{p}_1,\,\boldsymbol{p}_2}^{\leq k_\mathrm{F}} \Big(\mathrm{e}^{-\mathrm{i}\boldsymbol{p}_1\,\cdot\,(\boldsymbol{r}_1-\boldsymbol{r}_4)}\, \mathrm{e}^{-\mathrm{i}\boldsymbol{p}_2\,\cdot\,(\boldsymbol{r}_2-\boldsymbol{r}_3)} \\
&\qquad - \mathrm{e}^{-\mathrm{i}\boldsymbol{p}_1\,\cdot\,(\boldsymbol{r}_1-\boldsymbol{r}_3)}\, \mathrm{e}^{-\mathrm{i}\boldsymbol{p}_2\,\cdot\,(\boldsymbol{r}_2-\boldsymbol{r}_4)} \Big) ,
\end{aligned} \tag{E.13}$$

which can be used to simplify Eq. (6.18)

$$\begin{aligned}
\bar{A}_{r_\mathrm{D}} &= 2 \sum_{\boldsymbol{\alpha}} \int \mathrm{d}^3\boldsymbol{R} \int \mathrm{d}^3\boldsymbol{r} \int \mathrm{d}^3\boldsymbol{r}'\, \phi^*_{\boldsymbol{\alpha}}(\boldsymbol{r})\, \phi_{\boldsymbol{\alpha}}(\boldsymbol{r}') \\
&\qquad \times \frac{1}{V^2} \sum_{\boldsymbol{p}_1,\,\boldsymbol{p}_2}^{\leq k_\mathrm{F}} \left(\mathrm{e}^{-\mathrm{i}\boldsymbol{p}_1\,\cdot\,\frac{\boldsymbol{r}'-\boldsymbol{r}}{2}}\, \mathrm{e}^{\mathrm{i}\boldsymbol{p}_2\,\cdot\,\frac{\boldsymbol{r}'-\boldsymbol{r}}{2}} - \mathrm{e}^{-\mathrm{i}\boldsymbol{p}_1\,\cdot\,\frac{\boldsymbol{r}'+\boldsymbol{r}}{2}}\, \mathrm{e}^{\mathrm{i}\boldsymbol{p}_2\,\cdot\,\frac{\boldsymbol{r}'+\boldsymbol{r}}{2}} \right) \\
&= 2 \sum_{\boldsymbol{\alpha}} \int \mathrm{d}^3\boldsymbol{R} \int \mathrm{d}^3\boldsymbol{r} \int \mathrm{d}^3\boldsymbol{r}'\, \phi^*_{\boldsymbol{\alpha}}(\boldsymbol{r})\, \phi_{\boldsymbol{\alpha}}(\boldsymbol{r}') \\
&\qquad \times \frac{1}{V^2} \sum_{\boldsymbol{p}_1,\,\boldsymbol{p}_2}^{\leq k_\mathrm{F}} \left(\mathrm{e}^{-\mathrm{i}\boldsymbol{p}_1\,\cdot\,\frac{\boldsymbol{r}'-\boldsymbol{r}}{2}}\, \mathrm{e}^{\mathrm{i}\boldsymbol{p}_2\,\cdot\,\frac{\boldsymbol{r}'-\boldsymbol{r}}{2}} - \mathrm{e}^{-\mathrm{i}\boldsymbol{p}_1\,\cdot\,\frac{\boldsymbol{r}'+\boldsymbol{r}}{2}}\, \mathrm{e}^{\mathrm{i}\boldsymbol{p}_2\,\cdot\,\frac{\boldsymbol{r}'+\boldsymbol{r}}{2}} \right) \\
&= 2 \sum_{\boldsymbol{\alpha}} \int \mathrm{d}^3\boldsymbol{R} \int \mathrm{d}^3\boldsymbol{r} \int \mathrm{d}^3\boldsymbol{r}'\, \phi^*_{\boldsymbol{\alpha}}(\boldsymbol{r})\, \phi_{\boldsymbol{\alpha}}(\boldsymbol{r}') \\
&\qquad \left(\left| \int_{k\leq k_\mathrm{F}} \frac{\mathrm{d}^3\boldsymbol{p}}{(2\pi)^3}\, \mathrm{e}^{-\mathrm{i}\boldsymbol{p}\,\cdot\,\frac{\boldsymbol{r}-\boldsymbol{r}'}{2}} \right|^2 - \left| \int_{k\leq k_\mathrm{F}} \frac{\mathrm{d}^3\boldsymbol{p}}{(2\pi)^3}\, \mathrm{e}^{-\mathrm{i}\boldsymbol{p}\,\cdot\,\frac{\boldsymbol{r}+\boldsymbol{r}'}{2}} \right|^2 \right) .
\end{aligned} \tag{E.14}$$

Further we find

$$\begin{aligned}\left|\int_{k\leq k_\mathrm{F}}\frac{\mathrm{d}^3\boldsymbol{p}}{(2\pi)^3}\,\mathrm{e}^{-\mathrm{i}\boldsymbol{p}\,\cdot\,\boldsymbol{y}}\right|^2 &= \left|\frac{1}{(2\pi)^3}\int_0^{k_\mathrm{F}}\mathrm{d}p\,p^2\int_0^{2\pi}\mathrm{d}\varphi\int_{-1}^{1}\mathrm{d}x\,\mathrm{e}^{-\mathrm{i}pyx}\right|^2\\ &= \left|\frac{2\pi}{(2\pi)^3}\int_0^{k_\mathrm{F}}\mathrm{d}p\,p^2\frac{-1}{\mathrm{i}py}\Big(\mathrm{e}^{-\mathrm{i}py}-\mathrm{e}^{\mathrm{i}py}\Big)\right|^2\\ &= \left|\frac{1}{(2\pi)^2}\int_0^{k_\mathrm{F}}\mathrm{d}p\,p\,\frac{2}{y}\,\sin\Big(py\Big)\right|^2 .\end{aligned} \tag{E.15}$$

We use

$$\int\mathrm{d}x\,x\sin(Cx)=\frac{1}{C^2}\Big(\sin(Cx)-Cx\cos(Cx)\Big)+\text{const.} \tag{E.16}$$

and obtain

$$\begin{aligned}\left|\int_{k\leq k_\mathrm{F}}\frac{\mathrm{d}^3\boldsymbol{p}}{(2\pi)^3}\,\mathrm{e}^{-\mathrm{i}\boldsymbol{p}\,\cdot\,\boldsymbol{y}}\right|^2 &= \left|\frac{k_\mathrm{F}^3}{2\pi^2}\,\frac{1}{(k_\mathrm{F}y)^3}\left(\sin\Big(k_\mathrm{F}y\Big)-k_\mathrm{F}y\cos\Big(k_\mathrm{F}y\Big)\right)\right|^2\\ &= \left(\frac{k_\mathrm{F}^3}{2\pi^2}\,h\Big(k_\mathrm{F}y\Big)\right)^2 ,\end{aligned} \tag{E.17}$$

were we defined

$$h(x)=\frac{\sin(x)-x\,\cos(x)}{x^3}\ . \tag{E.18}$$

The absorption rate is then given by (c.f. Eq. (6.24))

$$\begin{aligned}\bar{A}_{r_\mathrm{D}} = 2\sum_{\boldsymbol{\alpha}}\int\mathrm{d}^3\boldsymbol{R}\int\mathrm{d}^3\boldsymbol{r}\int\mathrm{d}^3\boldsymbol{r}'\,\phi^*_{\boldsymbol{\alpha}}(\boldsymbol{r})\,\phi_{\boldsymbol{\alpha}}(\boldsymbol{r}')\,\left(\frac{k_\mathrm{F}^3}{2\pi^2}\right)^2\\ \times\left[h\left(k_\mathrm{F}\frac{|\boldsymbol{r}-\boldsymbol{r}'|}{2}\right)^2-h\left(k_\mathrm{F}\frac{|\boldsymbol{r}+\boldsymbol{r}'|}{2}\right)^2\right]\ .\end{aligned} \tag{E.19}$$

In the case $\boldsymbol{r}\parallel\boldsymbol{r}'$ we define

$$\xi(r,r')=\left(\frac{k_\mathrm{F}^3}{2\pi^2}\right)^2\left[h\left(k_\mathrm{F}\frac{r-r'}{2}\right)^2-h\left(k_\mathrm{F}\frac{r+r'}{2}\right)^2\right]\ . \tag{E.20}$$

E.5. Pair Correlation Function of the Fermi Sea

In the following we present a derivation of the pair correlation function $g^{(2)}(r)$ for spin polarized Fermions. By again using the convention

$$\hat{c}_{\boldsymbol{r}} = \frac{1}{\sqrt{V}} \sum_{\boldsymbol{k}} \mathrm{e}^{\mathrm{i}\boldsymbol{r}\boldsymbol{k}} \hat{c}_{\boldsymbol{k}} \ , \tag{E.21}$$

we find

$$\begin{aligned} n^2 g^{(2)}(|\boldsymbol{r}-\boldsymbol{r}'|) &= \langle \mathrm{FS}| \, \hat{c}^\dagger_{\boldsymbol{r}} \, \hat{c}^\dagger_{\boldsymbol{r}'} \, \hat{c}_{\boldsymbol{r}'} \, \hat{c}_{\boldsymbol{r}} \, |\mathrm{FS}\rangle \\ &= \frac{1}{V^2} \sum_{\boldsymbol{p}_1,\ldots,\boldsymbol{p}_4} \mathrm{e}^{-\mathrm{i}\boldsymbol{r}\,\cdot\,(\boldsymbol{p}_1-\boldsymbol{p}_4)} \, \mathrm{e}^{-\mathrm{i}\boldsymbol{r}'\,\cdot\,(\boldsymbol{p}_2-\boldsymbol{p}_3)} \ \langle \mathrm{FS}_c| \, \hat{c}^\dagger_{\boldsymbol{p}_1} \, \hat{c}^\dagger_{\boldsymbol{p}_2} \, \hat{c}_{\boldsymbol{p}_3} \, \hat{c}_{\boldsymbol{p}_4} \, |\mathrm{FS}_c\rangle \\ &= \frac{1}{V^2} \sum_{\boldsymbol{p}_1,\ldots,\boldsymbol{p}_4}^{\leq k_\mathrm{F}} \mathrm{e}^{-\mathrm{i}\boldsymbol{r}\,\cdot\,(\boldsymbol{p}_1-\boldsymbol{p}_4)} \, \mathrm{e}^{-\mathrm{i}\boldsymbol{r}'\,\cdot\,(\boldsymbol{p}_2-\boldsymbol{p}_3)} \ (\delta_{\boldsymbol{p}_1\boldsymbol{p}_4}\delta_{\boldsymbol{p}_2\boldsymbol{p}_3} - \delta_{\boldsymbol{p}_2\boldsymbol{p}_4}\delta_{\boldsymbol{p}_1\boldsymbol{p}_3}) \ , \end{aligned} \tag{E.22}$$

where we used

$$\begin{aligned} \langle \mathrm{FS}_c| \, \hat{c}^\dagger_{\boldsymbol{p}_1} \, \hat{c}^\dagger_{\boldsymbol{p}_2} \, \hat{c}_{\boldsymbol{p}_3} \, \hat{c}_{\boldsymbol{p}_4} \, |\mathrm{FS}_c\rangle &= \langle \mathrm{FS}_c| \, \hat{c}^\dagger_{\boldsymbol{p}_1} \, (\delta_{\boldsymbol{p}_2\boldsymbol{q}_3} - \hat{c}_{\boldsymbol{p}_3} \, \hat{c}^\dagger_{\boldsymbol{p}_2} \,) \hat{c}_{\boldsymbol{p}_4} \, |\mathrm{FS}_c\rangle \\ &= \langle \mathrm{FS}_c| \, (\delta_{\boldsymbol{p}_1\boldsymbol{p}_4} - \hat{c}_{\boldsymbol{p}_4} \, \hat{c}^\dagger_{\boldsymbol{p}_1} \,) \delta_{\boldsymbol{p}_2\boldsymbol{p}_3} - \hat{c}^\dagger_{\boldsymbol{p}_1} \, \hat{c}_{\boldsymbol{p}_3} \, \hat{c}^\dagger_{\boldsymbol{p}_2} \, \hat{c}_{\boldsymbol{p}_4} \, |\mathrm{FS}_c\rangle \\ &= \langle \mathrm{FS}_c| \, \delta_{\boldsymbol{p}_1\boldsymbol{p}_4}\delta_{\boldsymbol{p}_2\boldsymbol{p}_3} - (\delta_{\boldsymbol{p}1\boldsymbol{p}_3} - \hat{c}_{\boldsymbol{p}_3} \, \hat{c}^\dagger_{\boldsymbol{p}_1} \,) \\ &\qquad\qquad \times (\delta_{\boldsymbol{p}_2\boldsymbol{p}_4} - \hat{c}_{\boldsymbol{p}_4} \, \hat{c}^\dagger_{\boldsymbol{p}_2} \,) \, |\mathrm{FS}_c\rangle \\ &= \delta_{\boldsymbol{p}_1\boldsymbol{p}_4}\delta_{\boldsymbol{p}_2\boldsymbol{p}_3} - \delta_{\boldsymbol{p}_1\boldsymbol{p}_3}\delta_{\boldsymbol{p}_2\boldsymbol{p}_4} \ . \end{aligned} \tag{E.23}$$

This allows to obtain

$$\begin{aligned} n^2 g^{(2)}(|\boldsymbol{r}-\boldsymbol{r}'|) &= \frac{1}{V^2} \sum_{\boldsymbol{p}_1,\,\boldsymbol{p}_2}^{\leq k_\mathrm{F}} \Big(1 - \mathrm{e}^{-\mathrm{i}\boldsymbol{r}\,\cdot\,(\boldsymbol{p}_1-\boldsymbol{p}_2)} \, \mathrm{e}^{-\mathrm{i}\boldsymbol{r}'\,\cdot\,(\boldsymbol{p}_2-\boldsymbol{p}_1)} \Big) \\ &= \int\limits_{k\leq k_\mathrm{F}} \frac{\mathrm{d}^3\boldsymbol{p}}{(2\pi)^3} \int\limits_{k\leq k_\mathrm{F}} \frac{\mathrm{d}^3\boldsymbol{p}'}{(2\pi)^3} \Big(1 - \mathrm{e}^{-\mathrm{i}\boldsymbol{p}_1\,\cdot\,(\boldsymbol{r}-\boldsymbol{r}')} \, \mathrm{e}^{\mathrm{i}\boldsymbol{p}_2\,\cdot\,(\boldsymbol{r}-\boldsymbol{r}')} \Big) \\ &= n^2 - \left| \int\limits_{k\leq k_\mathrm{F}} \frac{\mathrm{d}^3\boldsymbol{p}}{(2\pi)^3} \mathrm{e}^{-\mathrm{i}\boldsymbol{p}\,\cdot\,(\boldsymbol{r}-\boldsymbol{r}')} \right|^2 \ . \end{aligned} \tag{E.24}$$

Now we calculate the integral

$$\begin{aligned}
G(\boldsymbol{R}) &= \int \frac{\mathrm{d}^3\boldsymbol{p}}{(2\pi)^3}\, \mathrm{e}^{-\mathrm{i}\boldsymbol{p}\cdot\boldsymbol{R}}\, \Theta(k_\mathrm{F} - |\boldsymbol{p}|) \\
&= \frac{1}{(2\pi)^3} \int_0^{k_\mathrm{F}} \mathrm{d}p\, p^2 \int_0^{2\pi} \mathrm{d}\varphi \int_{-1}^{1} \mathrm{d}z \mathrm{e}^{-\mathrm{i}pRz} \\
&= \frac{1}{4\pi^2} \int_0^{k_\mathrm{F}} \mathrm{d}p\, p^2 \frac{1}{-\mathrm{i}pR} \left[\mathrm{e}^{-\mathrm{i}pR} - \mathrm{e}^{\mathrm{i}pR}\right] \\
&= \frac{1}{4\pi^2} \int_0^{k_\mathrm{F}} \mathrm{d}p\, p\, \frac{1}{R}\, 2\, \sin(pR) \\
&= \frac{1}{2\pi^2\, R} \left(\left[-\frac{p}{R}\, \cos(pR) \right]_0^{k_\mathrm{F}} - \int_0^{k_\mathrm{F}} \mathrm{d}p\, \frac{-\cos(pR)}{R} \right) \\
&= \frac{1}{2\pi^2\, R} \left(-\frac{k_\mathrm{F}\, \cos(pR)}{R} + \left[\frac{\sin(pR)}{R^2} \right]_0^{k_\mathrm{F}} \right) \\
&= \frac{1}{2\pi^2} \frac{\sin(k_\mathrm{F}R) - k_\mathrm{F}R\, \cos(k_\mathrm{F}R)}{R^3} \\
&= 3n \frac{\sin(k_\mathrm{F}R) - k_\mathrm{F}R\, \cos(k_\mathrm{F}R)}{(k_\mathrm{F}R)^3}\ ,
\end{aligned} \tag{E.25}$$

with $n = k_\mathrm{F}^3/6\pi^2$ for spin polarized fermions. The pair correlation function

$$g^{(2)}(|\boldsymbol{r} - \boldsymbol{r}'|) = 1 - \Big(3\, h(k_\mathrm{F}|\boldsymbol{r} - \boldsymbol{r}'|)\Big)^2 \tag{E.26}$$

follows from the combination of Eq. (E.24) and Eq. (E.25), after dividing by n^2 and defining

$$h(u) = \frac{\sin(u) - u\, \cos(u)}{u^3}\ . \tag{E.27}$$

E.6. Absorption Strength of an Unpolarized ULRRM Dimer

In analogy to the discussion in Chapter 6 we here repeat the calculation of the ULRRM-dimer absorption strength for quantum gases consisting of fermions with two different spins $(\uparrow,\downarrow)$ and ULRRM-dimer molecules consisting of atoms with **different** spins. In this case the final state is approximated by

$$\begin{aligned}|\mathrm{f}\rangle &= |\mathrm{f}(\boldsymbol{\lambda},\boldsymbol{\alpha},\boldsymbol{p},\boldsymbol{p}')\rangle \\ &= \int \mathrm{d}^3\boldsymbol{R}\int \mathrm{d}^3\boldsymbol{r}\,\Psi_{\boldsymbol{\lambda},\boldsymbol{\alpha}}(\boldsymbol{R},\boldsymbol{r})\,\hat{d}^\dagger_{\uparrow\,\boldsymbol{R}-\frac{\boldsymbol{r}}{2}}\,\hat{c}^\dagger_{\downarrow\,\boldsymbol{R}+\frac{\boldsymbol{r}}{2}}\,\hat{c}_{\uparrow\boldsymbol{p}}\,\hat{c}_{\downarrow\boldsymbol{p}'}\,|\mathrm{FS}_\uparrow\rangle\otimes|\mathrm{FS}_\downarrow\rangle \\ &= \int \mathrm{d}^3\boldsymbol{R}\,\Phi_{\boldsymbol{\lambda}}(\boldsymbol{R})\int \mathrm{d}^3\boldsymbol{r}\,\phi_{\boldsymbol{\alpha}}(\boldsymbol{r})\,\hat{d}^\dagger_{\uparrow\,\boldsymbol{R}-\frac{\boldsymbol{r}}{2}}\,\hat{c}^\dagger_{\downarrow\,\boldsymbol{R}+\frac{\boldsymbol{r}}{2}}\,\hat{c}_{\uparrow\boldsymbol{p}}\,\hat{c}_{\downarrow\boldsymbol{p}'}\,|\mathrm{FS}_\uparrow\rangle\otimes|\mathrm{FS}_\downarrow\rangle\ .\end{aligned} \tag{E.28}$$

Using the definition Eq. (6.4) for the laser operator which does not allow for spin flips and the initial state

$$|\mathrm{i}\rangle = |\mathrm{FS}_\uparrow\rangle\otimes|\mathrm{FS}_\downarrow\rangle\otimes|0\rangle_d \tag{E.29}$$

we find (where we suppress '$\otimes|0\rangle_d$' in the notation)

$$\begin{aligned}\bar{A} &= \sum_{\mathrm{f}}\big|\,\langle\mathrm{f}|\,\hat{V}_\mathrm{L}\,|\mathrm{i}\rangle\,\big|^2 \\ &= \sum_{\boldsymbol{\lambda},\boldsymbol{\alpha}}\sum_{\boldsymbol{p},\boldsymbol{p}'}\big|\,\langle\mathrm{FS}_\uparrow|\otimes\langle\mathrm{FS}_\downarrow|\int \mathrm{d}^3\boldsymbol{R}\int \mathrm{d}^3\boldsymbol{r}\,\Psi^*_{\boldsymbol{\lambda},\boldsymbol{\alpha}}(\boldsymbol{R},\boldsymbol{r})\,\hat{c}^\dagger_{\downarrow\boldsymbol{p}'}\,\hat{c}^\dagger_{\uparrow\boldsymbol{p}}\,\hat{c}_{\downarrow\,\boldsymbol{R}+\frac{\boldsymbol{r}}{2}}\,\hat{d}_{\uparrow\,\boldsymbol{R}-\frac{\boldsymbol{r}}{2}} \\ &\qquad\qquad\times\int \mathrm{d}^3\boldsymbol{r}_\mathrm{L}\,\hat{d}^\dagger_{\uparrow\,\boldsymbol{r}_\mathrm{L}}\,\hat{c}_{\uparrow\,\boldsymbol{r}_\mathrm{L}}\,|\mathrm{FS}_\uparrow\rangle\otimes|\mathrm{FS}_\downarrow\rangle\,\big|^2 \\ &= \sum_{\boldsymbol{\lambda},\boldsymbol{\alpha}}\sum_{\boldsymbol{p},\boldsymbol{p}'}\big|\,\langle\mathrm{FS}_\uparrow|\otimes\langle\mathrm{FS}_\downarrow|\int \mathrm{d}^3\boldsymbol{R}\int \mathrm{d}^3\boldsymbol{r}\,\Psi^*_{\boldsymbol{\lambda},\boldsymbol{\alpha}}(\boldsymbol{R},\boldsymbol{r})\,\hat{c}^\dagger_{\downarrow\boldsymbol{p}'}\,\hat{c}^\dagger_{\uparrow\boldsymbol{p}}\,\hat{c}_{\downarrow\,\boldsymbol{R}+\frac{\boldsymbol{r}}{2}}\,\hat{c}_{\uparrow\,\boldsymbol{r}_\mathrm{L}} \\ &\qquad\qquad\times\int \mathrm{d}^3\boldsymbol{r}_\mathrm{L}\,\delta^{(3)}\Big(\boldsymbol{r}_\mathrm{L}-\Big(\boldsymbol{R}-\frac{\boldsymbol{r}}{2}\Big)\Big)\,|\mathrm{FS}_\uparrow\rangle\otimes|\mathrm{FS}_\downarrow\rangle\,\big|^2 \\ &= \sum_{\boldsymbol{\lambda},\boldsymbol{\alpha}}\sum_{\boldsymbol{p},\boldsymbol{p}'}\big|\int \mathrm{d}^3\boldsymbol{R}\int \mathrm{d}^3\boldsymbol{r}\,\Psi^*_{\boldsymbol{\lambda},\boldsymbol{\alpha}}(\boldsymbol{R},\boldsymbol{r}) \\ &\qquad\qquad\times\langle\mathrm{FS}_\uparrow|\otimes\langle\mathrm{FS}_\downarrow|\,\hat{c}^\dagger_{\downarrow\boldsymbol{p}'}\,\hat{c}^\dagger_{\uparrow\boldsymbol{p}}\,\hat{c}_{\downarrow\,\boldsymbol{R}+\frac{\boldsymbol{r}}{2}}\,\hat{c}_{\uparrow\,\boldsymbol{R}-\frac{\boldsymbol{r}}{2}}\,|\mathrm{FS}_\uparrow\rangle\otimes|\mathrm{FS}_\downarrow\rangle\,\big|^2\end{aligned} \tag{E.30}$$

$$\begin{aligned}&= \sum_{\boldsymbol{\lambda},\boldsymbol{\alpha}}\sum_{\boldsymbol{p},\boldsymbol{p}'}\int \mathrm{d}^3\boldsymbol{R}\int \mathrm{d}^3\boldsymbol{R}'\int \mathrm{d}^3\boldsymbol{r}\int \mathrm{d}^3\boldsymbol{r}'\,\Psi^*_{\boldsymbol{\lambda},\boldsymbol{\alpha}}(\boldsymbol{R},\boldsymbol{r})\Psi_{\boldsymbol{\lambda},\boldsymbol{\alpha}}(\boldsymbol{R}',\boldsymbol{r}') \\ &\qquad\times\langle\mathrm{FS}_\uparrow|\,\hat{c}^\dagger_{\uparrow\,\boldsymbol{R}'-\frac{\boldsymbol{r}'}{2}}\,\hat{c}_{\uparrow\boldsymbol{p}}\,|\mathrm{FS}_\uparrow\rangle\,\langle\mathrm{FS}_\uparrow|\,\hat{c}^\dagger_{\uparrow\boldsymbol{p}}\,\hat{c}_{\uparrow\,\boldsymbol{R}-\frac{\boldsymbol{r}}{2}}\,|\mathrm{FS}_\uparrow\rangle \\ &\qquad\times\langle\mathrm{FS}_\downarrow|\,\hat{c}^\dagger_{\downarrow\,\boldsymbol{R}'+\frac{\boldsymbol{r}'}{2}}\,\hat{c}_{\downarrow\boldsymbol{p}'}\,|\mathrm{FS}_\downarrow\rangle\,\langle\mathrm{FS}_\downarrow|\,\hat{c}^\dagger_{\downarrow\boldsymbol{p}'}\,\hat{c}_{\downarrow\,\boldsymbol{R}+\frac{\boldsymbol{r}}{2}}\,|\mathrm{FS}_\downarrow\rangle\ .\end{aligned}$$

Now we evaluate

$$\begin{aligned}\langle \mathrm{FS}|\, \hat{c}^\dagger_{\boldsymbol{r}_1}\, \hat{c}_{\boldsymbol{p}'}\, |\mathrm{FS}\rangle\, \langle \mathrm{FS}|\, \hat{c}^\dagger_{\boldsymbol{p}'}\, \hat{c}_{\boldsymbol{r}_2}\, |\mathrm{FS}\rangle &= \frac{1}{V}\sum_{\boldsymbol{kq}} \mathrm{e}^{-\mathrm{i}\boldsymbol{k}\,\cdot\,\boldsymbol{r}_1}\mathrm{e}^{\mathrm{i}\boldsymbol{q}\,\cdot\,\boldsymbol{r}_2}\, \langle \mathrm{FS}|\, \hat{c}^\dagger_{\boldsymbol{k}}\, \hat{c}_{\boldsymbol{p}'}\, |\mathrm{FS}\rangle \\ &\qquad \times \langle \mathrm{FS}|\, \hat{c}^\dagger_{\boldsymbol{p}'}\, \hat{c}_{\boldsymbol{q}}\, |\mathrm{FS}\rangle \\ &= \frac{1}{V}\sum_{\boldsymbol{kq}} \mathrm{e}^{-\mathrm{i}\boldsymbol{k}\,\cdot\,\boldsymbol{r}_1}\mathrm{e}^{\mathrm{i}\boldsymbol{q}\,\cdot\,\boldsymbol{r}_2}\, \delta_{\boldsymbol{kp}'}\delta_{\boldsymbol{qp}'} \\ &= \frac{1}{V}\,\mathrm{e}^{-\mathrm{i}\boldsymbol{p}'\,\cdot\,(\boldsymbol{r}_1-\boldsymbol{r}_2)}\ ,\end{aligned} \tag{E.31}$$

which can be used to simplify Eq. (E.30). We arrive at the expression for the absorption rate of spin-zero Rydberg molecules

$$\begin{aligned}\bar{A} = \sum_{\boldsymbol{\lambda},\boldsymbol{\alpha}} \int \mathrm{d}^3\boldsymbol{R} \int \mathrm{d}^3\boldsymbol{R}' \int \mathrm{d}^3\boldsymbol{r} \int \mathrm{d}^3\boldsymbol{r}'\, \Psi^*_{\boldsymbol{\lambda},\boldsymbol{\alpha}}(\boldsymbol{R},\boldsymbol{r})\Psi_{\boldsymbol{\lambda},\boldsymbol{\alpha}}(\boldsymbol{R}',\boldsymbol{r}') \\ \times \sum_{\boldsymbol{p},\boldsymbol{p}'}^{\leq \boldsymbol{k}_\mathrm{F}} \frac{1}{V^2}\,\mathrm{e}^{-\mathrm{i}\boldsymbol{p}\,\cdot\,(\boldsymbol{R}'-\frac{\boldsymbol{r}'}{2}-(\boldsymbol{R}-\frac{\boldsymbol{r}}{2}))}\mathrm{e}^{-\mathrm{i}\boldsymbol{p}'\,\cdot\,(\boldsymbol{R}'+\frac{\boldsymbol{r}'}{2}-(\boldsymbol{R}+\frac{\boldsymbol{r}}{2}))}\ .\end{aligned} \tag{E.32}$$

Ansatz: plane wave center of mass wave function

We again investigate wave functions of the type

$$\begin{aligned}\Psi_{\boldsymbol{\lambda},\boldsymbol{\alpha}}(\boldsymbol{R},\boldsymbol{r}) &= \Phi_{\boldsymbol{\lambda}}(\boldsymbol{R})\,\phi_{\boldsymbol{\alpha}}(\boldsymbol{r})\ , \\ \phi_{\boldsymbol{\alpha}}(\boldsymbol{r}) &= \frac{u_{\nu r_\mathrm{D}}(r)}{r}\,Y_{lm}(\Omega_{\boldsymbol{r}})\ , \\ \Phi_{\boldsymbol{\lambda}}(\boldsymbol{R}) &= \frac{\mathrm{e}^{-\mathrm{i}\,\boldsymbol{K}\boldsymbol{R}}}{\sqrt{V}}\ ,\end{aligned} \tag{E.33}$$

where the radial component χ does not depend on l. We again keep the relative dimer wave function unspecified and find

$$\begin{aligned}
\bar{A} &= \sum_{\boldsymbol{K},\boldsymbol{\alpha}} \sum_{\boldsymbol{p},\boldsymbol{p}'} \int \mathrm{d}^3\boldsymbol{R} \int \mathrm{d}^3\boldsymbol{R}' \int \mathrm{d}^3\boldsymbol{r} \int \mathrm{d}^3\boldsymbol{r}'\, \phi^*_{\boldsymbol{\alpha}}(\boldsymbol{r})\phi_{\boldsymbol{\alpha}}(\boldsymbol{r}')\, \frac{1}{V} \mathrm{e}^{-\mathrm{i}\boldsymbol{K}\cdot(\boldsymbol{R}'-\boldsymbol{R})} \\
&\qquad \times \sum_{\boldsymbol{p},\boldsymbol{p}'}^{\leq \boldsymbol{k}_\mathrm{F}} \frac{1}{V^2}\, \mathrm{e}^{-\mathrm{i}\boldsymbol{p}\cdot(\boldsymbol{R}'-\frac{\boldsymbol{r}'}{2}-(\boldsymbol{R}-\frac{\boldsymbol{r}}{2}))} \mathrm{e}^{-\mathrm{i}\boldsymbol{p}'\cdot(\boldsymbol{R}'+\frac{\boldsymbol{r}'}{2}-(\boldsymbol{R}+\frac{\boldsymbol{r}}{2}))} \\
&= \sum_{\boldsymbol{\alpha}} \int \mathrm{d}^3\boldsymbol{R} \int \mathrm{d}^3\boldsymbol{R}' \int \mathrm{d}^3\boldsymbol{r} \int \mathrm{d}^3\boldsymbol{r}'\, \phi^*_{\boldsymbol{\alpha}}(\boldsymbol{r})\phi_{\boldsymbol{\alpha}}(\boldsymbol{r}')\, \delta^{(3)}(\boldsymbol{R}'-\boldsymbol{R}) \\
&\qquad \times \frac{1}{V^2} \sum_{\boldsymbol{p},\boldsymbol{p}'}^{\leq \boldsymbol{k}_\mathrm{F}} \mathrm{e}^{-\mathrm{i}\boldsymbol{p}\cdot(\boldsymbol{R}'-\frac{\boldsymbol{r}'}{2}-(\boldsymbol{R}-\frac{\boldsymbol{r}}{2}))} \mathrm{e}^{-\mathrm{i}\boldsymbol{p}'\cdot(\boldsymbol{R}'+\frac{\boldsymbol{r}'}{2}-(\boldsymbol{R}+\frac{\boldsymbol{r}}{2}))} \\
&= \sum_{\boldsymbol{\alpha}} \int \mathrm{d}^3\boldsymbol{R} \int \mathrm{d}^3\boldsymbol{r} \int \mathrm{d}^3\boldsymbol{r}'\, \phi^*_{\boldsymbol{\alpha}}(\boldsymbol{r})\phi_{\boldsymbol{\alpha}}(\boldsymbol{r}')\, \frac{1}{V^2} \sum_{\boldsymbol{p},\boldsymbol{p}'}^{\leq \boldsymbol{k}_\mathrm{F}} \mathrm{e}^{-\mathrm{i}\boldsymbol{p}\cdot\frac{\boldsymbol{r}-\boldsymbol{r}'}{2}} \mathrm{e}^{\mathrm{i}\boldsymbol{p}'\cdot\frac{\boldsymbol{r}'-\boldsymbol{r}}{2}} \\
&= \sum_{\boldsymbol{\alpha}} \int \mathrm{d}^3\boldsymbol{R} \int \mathrm{d}^3\boldsymbol{r} \int \mathrm{d}^3\boldsymbol{r}'\, \phi^*_{\boldsymbol{\alpha}}(\boldsymbol{r})\phi_{\boldsymbol{\alpha}}(\boldsymbol{r}') \left| \int\limits_{k\leq k_\mathrm{F}} \frac{\mathrm{d}^3\boldsymbol{p}}{(2\pi)^3}\, \mathrm{e}^{-\mathrm{i}\boldsymbol{p}\cdot\frac{\boldsymbol{r}-\boldsymbol{r}'}{2}} \right|^2 \\
&= \sum_{\boldsymbol{\alpha}} \int \mathrm{d}^3\boldsymbol{R} \int \mathrm{d}^3\boldsymbol{r} \int \mathrm{d}^3\boldsymbol{r}'\, \phi^*_{\boldsymbol{\alpha}}(\boldsymbol{r})\phi_{\boldsymbol{\alpha}}(\boldsymbol{r}') \left(\frac{k_\mathrm{F}^3}{2\pi^2}\, h\Big(k_\mathrm{F}\frac{|\boldsymbol{r}-\boldsymbol{r}'|}{2}\Big) \right)^2 ,
\end{aligned} \tag{E.34}$$

were we have again used the relation derived in App. E.4 and the define

$$h(u) = \frac{\sin(u) - u\,\cos(u)}{u^3} \ . \tag{E.35}$$

Here it is important to note that the fermion density is given by $n_{\uparrow\downarrow}/2 = k_\mathrm{F}^3/6\pi^2$.

Relative Dimer Wave Functions

We investigate functions of the type

$$\phi_{\boldsymbol{\alpha}}(\boldsymbol{r}) = \frac{u_{\nu r_\mathrm{D}}(r)}{r}\, Y_{lm}(\Omega_{\boldsymbol{r}}) \ , \tag{E.36}$$

where the radial component $\phi_{\boldsymbol{\alpha}}$ does not depend on l, and the indices ν, l and m again label the principal quantum number, angular momentum quantum number and angular

momentum projection quantum number. From Eq. (E.34) we obtain

$$\begin{aligned}
\bar{A}_{r_\mathrm{D}} &= \sum_{lm} \int \mathrm{d}\Omega_{\boldsymbol{r}_\mathrm{D}} \int \mathrm{d}^3\boldsymbol{R} \int \mathrm{d}^3\boldsymbol{r} \int \mathrm{d}^3\boldsymbol{r}' \, \frac{u^*_{\nu r_\mathrm{D}}(r)}{r} \, Y^*_{lm}(\Omega_{\boldsymbol{r}}) \, \frac{u_{\nu r_\mathrm{D}}(r')}{r'} \, Y_{lm}(\Omega_{\boldsymbol{r}'}) \\
&\qquad \times \left(\frac{k_\mathrm{F}^3}{2\pi^2} h\Big(k_\mathrm{F} \, \frac{|\boldsymbol{r} - \boldsymbol{r}'|}{2} \Big) \right)^2 \\
&= \int \mathrm{d}\Omega_{\boldsymbol{r}_\mathrm{D}} \int \mathrm{d}^3\boldsymbol{R} \int_0^\infty \mathrm{d}r \int_0^\infty \mathrm{d}r' \, rr' \, u^*_{\nu r_\mathrm{D}}(r) \, u_{\nu r_\mathrm{D}}(r') \int \mathrm{d}\Omega_{\boldsymbol{r}} \int \mathrm{d}\Omega_{\boldsymbol{r}'} \\
&\qquad \times \sum_{lm} Y^*_{lm}(\Omega_{\boldsymbol{r}}) \, Y_{lm}(\Omega_{\boldsymbol{r}'}) \left(\frac{k_\mathrm{F}^3}{2\pi^2} \, h\Big(k_\mathrm{F} \, \frac{|\boldsymbol{r} - \boldsymbol{r}'|}{2} \Big) \right)^2 \qquad \text{(E.37)} \\
&= \int \mathrm{d}\Omega_{\boldsymbol{r}_\mathrm{D}} \int \mathrm{d}\Omega_{\boldsymbol{r}} \int \mathrm{d}^3\boldsymbol{R} \int_0^\infty \mathrm{d}r \int_0^\infty \mathrm{d}r' \, rr' \, u^*_{\nu r_\mathrm{D}}(r) \, u_{\nu r_\mathrm{D}}(r') \\
&\qquad \times \left(\frac{k_\mathrm{F}^3}{2\pi^2} \, h\Big(k_\mathrm{F} \, \frac{r - r'}{2} \Big) \right)^2 \\
&= \frac{4}{\pi^2} \, V \int_0^\infty \mathrm{d}r \int_0^\infty \mathrm{d}r' \, rr' \, u^*_{\nu r_\mathrm{D}}(r) \, u_{\nu r_\mathrm{D}}(r') \, k_\mathrm{F}^6 \, h\Big(k_\mathrm{F} \, \frac{r - r'}{2} \Big)^2 \, ,
\end{aligned}$$

which is the statement of Eq. (6.33). In the second last step we again made use of the completeness relation

$$\sum_{l=0}^{\infty} \sum_{m=-l}^{l} Y^*_{lm}(\Omega_{\boldsymbol{r}}) \, Y_{lm}(\Omega_{\boldsymbol{r}'}) = \delta(\varphi - \varphi') \, \delta(\cos\theta - \cos\theta') \, . \qquad \text{(E.38)}$$

F. Towards a Theoretical Description of Rydberg Excitation Microscopy in Arbitrarily Correlated States

Here we want to present open questions arising from the ansatz presented in Chapter 6 when used to analytically predict the ULRRM-dimer response of Rydberg atoms excited from an arbitrarily correlated state of ultracold atoms. To this end, we assume that the initial state can be expressed as a superposition of Fock states, i.e.,

$$|\mathrm{i}\rangle = \sum_{\mathrm{F}} \alpha_{\mathrm{F}} \, |\mathrm{F}\rangle \otimes |0\rangle_d \ , \tag{F.1}$$

with one unique set of coefficients $\{\alpha_{\mathrm{F}}\}$

$$\sum_{\mathrm{F}} |\alpha_{\mathrm{F}}|^2 = 1 \tag{F.2}$$

and fermionic Fock states

$$|\mathrm{F}\rangle = \prod_{i=1}^{\infty} \left(\hat{c}^{\dagger}_{\boldsymbol{k}_i}\right)^{n_i^{\mathrm{F}}} |0\rangle = |n_1^{\mathrm{F}}, n_2^{\mathrm{F}}, \ldots, n_i^{\mathrm{F}}, \ldots, n_{\infty}^{\mathrm{F}}\rangle \ , \tag{F.3}$$

with

$$\sum_{i=1}^{\infty} n_i^{\mathrm{F}} = N \quad , \ \forall \ \mathrm{F}. \tag{F.4}$$

Again we choose the ansatz similar to the one presented in Eq. (6.8) to describe the final states

$$\begin{aligned} |\mathrm{f}\rangle &= |\mathrm{f}(\boldsymbol{\lambda}, \boldsymbol{\alpha}, \boldsymbol{p}, \boldsymbol{p}')\rangle \\ &= \int \mathrm{d}^3\boldsymbol{R} \int \mathrm{d}^3\boldsymbol{r} \, \Psi_{\boldsymbol{\lambda},\boldsymbol{\alpha}}(\boldsymbol{R}, \boldsymbol{r}) \, \hat{d}^{\dagger}_{\boldsymbol{R}-\frac{\boldsymbol{r}}{2}} \, \hat{c}^{\dagger}_{\boldsymbol{R}+\frac{\boldsymbol{r}}{2}} \, \hat{c}_{\boldsymbol{p}} \, \hat{c}_{\boldsymbol{p}'} \, |\mathrm{i}\rangle \ , \end{aligned} \tag{F.5}$$

and investigate the ULRRM-dimer response

$$\bar{A} = \sum_{\mathrm{f}} \left| \, \langle \mathrm{f}| \, \hat{V}_{\mathrm{L}} \, |\mathrm{i}\rangle \, \right|^2 \ , \tag{F.6}$$

with the laser operator

$$\hat{V}_{\mathrm{L}} = \int \mathrm{d}^3\boldsymbol{r}\; \hat{d}^\dagger_{\boldsymbol{r}} \hat{c}_{\boldsymbol{r}} + \mathrm{h.c.}\;. \tag{F.7}$$

The dimer signal is then given by

$$\begin{aligned}
\bar{A} &= \sum_{\mathrm{f}} \left| \langle \mathrm{f}| \hat{V}_{\mathrm{L}} |\mathrm{i}\rangle \right|^2 \\
&= \sum_{\boldsymbol{\lambda},\boldsymbol{\alpha}} \sum_{\boldsymbol{p},\boldsymbol{p}'} \Big| \langle \mathrm{i}| \int \mathrm{d}^3\boldsymbol{R} \int \mathrm{d}^3\boldsymbol{r}\; \Psi^*_{\boldsymbol{\lambda},\boldsymbol{\alpha}}(\boldsymbol{R},\boldsymbol{r})\, \hat{c}^\dagger_{\boldsymbol{p}'}\, \hat{c}^\dagger_{\boldsymbol{p}}\, \hat{c}_{\boldsymbol{R}+\frac{\boldsymbol{r}}{2}}\, \hat{d}_{\boldsymbol{R}-\frac{\boldsymbol{r}}{2}} \\
&\qquad\qquad \times \left(\int \mathrm{d}^3\boldsymbol{r}_{\mathrm{L}}\, \hat{d}^\dagger_{\boldsymbol{r}_{\mathrm{L}}}\, \hat{c}_{\boldsymbol{r}_{\mathrm{L}}} + \mathrm{h.c.} \right) |\mathrm{i}\rangle \Big|^2 \\
&= \sum_{\boldsymbol{\lambda},\boldsymbol{\alpha}} \sum_{\boldsymbol{p},\boldsymbol{p}'} \Big| \langle \mathrm{i}| \int \mathrm{d}^3\boldsymbol{R} \int \mathrm{d}^3\boldsymbol{r}\; \Psi^*_{\boldsymbol{\lambda},\boldsymbol{\alpha}}(\boldsymbol{R},\boldsymbol{r})\, \hat{c}^\dagger_{\boldsymbol{p}'}\, \hat{c}^\dagger_{\boldsymbol{p}}\, \hat{c}_{\boldsymbol{R}+\frac{\boldsymbol{r}}{2}}\, \hat{c}_{\boldsymbol{r}_{\mathrm{L}}} \\
&\qquad\qquad \times \int \mathrm{d}^3\boldsymbol{r}_{\mathrm{L}}\, \delta^{(3)}\Big(\boldsymbol{r}_{\mathrm{L}} - \Big(\boldsymbol{R} - \frac{\boldsymbol{r}}{2} \Big) \Big) |\mathrm{i}\rangle \Big|^2 \\
&= \sum_{\boldsymbol{\lambda},\boldsymbol{\alpha}} \int \mathrm{d}^3\boldsymbol{R} \int \mathrm{d}^3\boldsymbol{R}' \int \mathrm{d}^3\boldsymbol{r} \int \mathrm{d}^3\boldsymbol{r}'\; \Psi^*_{\boldsymbol{\lambda},\boldsymbol{\alpha}}(\boldsymbol{R},\boldsymbol{r}) \Psi_{\boldsymbol{\lambda},\boldsymbol{\alpha}}(\boldsymbol{R}',\boldsymbol{r}') \\
&\qquad \times \langle \mathrm{i}|\, \hat{c}^\dagger_{\boldsymbol{R}'-\frac{\boldsymbol{r}'}{2}}\, \hat{c}^\dagger_{\boldsymbol{R}'+\frac{\boldsymbol{r}'}{2}} \underbrace{\sum_{\boldsymbol{p},\boldsymbol{p}'} \hat{c}_{\boldsymbol{p}}\, \hat{c}_{\boldsymbol{p}'}\, |\mathrm{i}\rangle \, \langle \mathrm{i}|\, \hat{c}^\dagger_{\boldsymbol{p}'}\, \hat{c}^\dagger_{\boldsymbol{p}}\, \hat{c}_{\boldsymbol{R}+\frac{\boldsymbol{r}}{2}}\, \hat{c}_{\boldsymbol{R}-\frac{\boldsymbol{r}}{2}}}_{=B} |\mathrm{i}\rangle \;.
\end{aligned} \tag{F.8}$$

Again we look at the expression B where $|\mathrm{i}\rangle$ is now the general state characterized by Eq. (F.1)

$$\begin{aligned}
B &= \sum_{\boldsymbol{p},\boldsymbol{p}'} \hat{c}_{\boldsymbol{p}}\, \hat{c}_{\boldsymbol{p}'}\, |\mathrm{i}\rangle \, \langle \mathrm{i}|\, \hat{c}^\dagger_{\boldsymbol{p}'}\, \hat{c}^\dagger_{\boldsymbol{p}}\, \hat{c}_{\boldsymbol{R}+\frac{\boldsymbol{r}}{2}}\, \hat{c}_{\boldsymbol{R}-\frac{\boldsymbol{r}}{2}}\, |\mathrm{i}\rangle \\
&= 2 \sum_{\boldsymbol{p}<\boldsymbol{p}'} \hat{c}_{\boldsymbol{p}}\, \hat{c}_{\boldsymbol{p}'}\, |\mathrm{i}\rangle \, \langle \mathrm{i}|\, \hat{c}^\dagger_{\boldsymbol{p}'}\, \hat{c}^\dagger_{\boldsymbol{p}}\, \hat{c}_{\boldsymbol{R}+\frac{\boldsymbol{r}}{2}}\, \hat{c}_{\boldsymbol{R}-\frac{\boldsymbol{r}}{2}}\, |\mathrm{i}\rangle \\
&= 2 \sum_{\boldsymbol{p}<\boldsymbol{p}'} \hat{c}_{\boldsymbol{p}}\, \hat{c}_{\boldsymbol{p}'} \sum_{\mathrm{F},\mathrm{F}',\mathrm{F}''} \alpha_{\mathrm{F}}\, \alpha^*_{\mathrm{F}'}\, \alpha_{\mathrm{F}''}\, |\mathrm{F}\rangle \, \langle \mathrm{F}'|\, \hat{c}^\dagger_{\boldsymbol{p}'}\, \hat{c}^\dagger_{\boldsymbol{p}}\, \hat{c}_{\boldsymbol{R}+\frac{\boldsymbol{r}}{2}}\, \hat{c}_{\boldsymbol{R}-\frac{\boldsymbol{r}}{2}}\, |\mathrm{F}''\rangle \;.
\end{aligned} \tag{F.9}$$

The sum over F, F′ and F″ can be split into two contributions one where the occurring Fock states are identical, i.e., F=F′=F″ and one containing all other terms

$$\begin{aligned}
B &= 2 \sum_{\mathrm{F}} |\alpha_{\mathrm{F}}|^2 \alpha_{\mathrm{F}} \sum_{\boldsymbol{p}<\boldsymbol{p}'} \hat{c}_{\boldsymbol{p}}\, \hat{c}_{\boldsymbol{p}'}\, |\mathrm{F}\rangle \, \langle \mathrm{F}|\, \hat{c}^\dagger_{\boldsymbol{p}'}\, \hat{c}^\dagger_{\boldsymbol{p}}\, \hat{c}_{\boldsymbol{R}+\frac{\boldsymbol{r}}{2}}\, \hat{c}_{\boldsymbol{R}-\frac{\boldsymbol{r}}{2}}\, |\mathrm{F}\rangle \\
&\quad + 2 \sum_{\boldsymbol{p}<\boldsymbol{p}'} \hat{c}_{\boldsymbol{p}}\, \hat{c}_{\boldsymbol{p}'} \sum_{\substack{\mathrm{F},\mathrm{F}',\mathrm{F}'' \\ \text{w.o. } \mathrm{F}=\mathrm{F}'=\mathrm{F}''}} \alpha_{\mathrm{F}}\, \alpha^*_{\mathrm{F}'}\, \alpha_{\mathrm{F}''}\, |\mathrm{F}\rangle \, \langle \mathrm{F}'|\, \hat{c}^\dagger_{\boldsymbol{p}'}\, \hat{c}^\dagger_{\boldsymbol{p}}\, \hat{c}_{\boldsymbol{R}+\frac{\boldsymbol{r}}{2}}\, \hat{c}_{\boldsymbol{R}-\frac{\boldsymbol{r}}{2}}\, |\mathrm{F}''\rangle \;,
\end{aligned} \tag{F.10}$$

where 'w.o.' stands for 'without'. Using the relation derived in Appendix E.3 each term in the first line is found to be proportional to $\hat{c}_{\boldsymbol{R}+\frac{\boldsymbol{r}}{2}}\,\hat{c}_{\boldsymbol{R}-\frac{\boldsymbol{r}}{2}}\,|\mathrm{F}\rangle$

$$\begin{aligned} B = {} & 2\sum_{\mathrm{F}} |\alpha_{\mathrm{F}}|^2 \alpha_{\mathrm{F}}\,\hat{c}_{\boldsymbol{R}+\frac{\boldsymbol{r}}{2}}\,\hat{c}_{\boldsymbol{R}-\frac{\boldsymbol{r}}{2}}\,|\mathrm{F}\rangle \\ & + 2\sum_{\boldsymbol{p}<\boldsymbol{p}'} \hat{c}_{\boldsymbol{p}}\,\hat{c}_{\boldsymbol{p}'} \sum_{\substack{\mathrm{F},\mathrm{F}',\mathrm{F}'' \\ \text{w.o. } \mathrm{F}=\mathrm{F}'=\mathrm{F}''}} \alpha_{\mathrm{F}}\,\alpha^*_{\mathrm{F}'}\,\alpha_{\mathrm{F}''}\,|\mathrm{F}\rangle\,\langle\mathrm{F}'|\,\hat{c}^\dagger_{\boldsymbol{p}'}\,\hat{c}^\dagger_{\boldsymbol{p}}\,\hat{c}_{\boldsymbol{R}+\frac{\boldsymbol{r}}{2}}\,\hat{c}_{\boldsymbol{R}-\frac{\boldsymbol{r}}{2}}\,|\mathrm{F}''\rangle \ . \end{aligned} \tag{F.11}$$

The expression in the first line reveals the first problem of the ansatz in Eq. (F.1) as it only results in terms proportional to

$$\langle\mathrm{i}|\,\hat{c}^\dagger_{\boldsymbol{R}'-\frac{\boldsymbol{r}'}{2}}\,\hat{c}^\dagger_{\boldsymbol{R}'+\frac{\boldsymbol{r}'}{2}}\,\hat{c}_{\boldsymbol{R}+\frac{\boldsymbol{r}}{2}}\,\hat{c}_{\boldsymbol{R}-\frac{\boldsymbol{r}}{2}}\,|\mathrm{i}\rangle$$

in cases where the coefficients α_{F} only take two values 0 or a constant (i.e., for superpositions of Fock states with equal weights) as only in this case

$$\sum_{\mathrm{F}} |\alpha_{\mathrm{F}}|^2 \alpha_{\mathrm{F}}\,\hat{c}_{\boldsymbol{R}+\frac{\boldsymbol{r}}{2}}\,\hat{c}_{\boldsymbol{R}-\frac{\boldsymbol{r}}{2}}\,|\mathrm{F}\rangle \sim \hat{c}_{\boldsymbol{R}+\frac{\boldsymbol{r}}{2}}\,\hat{c}_{\boldsymbol{R}-\frac{\boldsymbol{r}}{2}}\,|\mathrm{i}\rangle \ . \tag{F.12}$$

The other terms in the second line of Eq. (F.11) give rise to off diagonal elements that couple all individual Fock states $|\mathrm{F}\rangle$ that appear in the general state $|\mathrm{i}\rangle$ and the general relation between the ULRRM-dimer absorption peak in an arbitrarily correlated quantum gas remains an open question.

G. Pair Correlation Function of a Dimer Molecule

Here we show how the pair correlation function of a molecule consisting of two fermions is connected to their wave function. The molecular state is defined by

$$|\Psi\rangle = \iint \mathrm{d}^3\boldsymbol{r}\,\mathrm{d}^3\boldsymbol{r}'\,\Psi(\boldsymbol{r},\boldsymbol{r}')\,\hat{c}^\dagger_{\boldsymbol{r}}\hat{c}^\dagger_{\boldsymbol{r}'}\,|0\rangle \ , \tag{G.1}$$

with a fermionic two-body wave function $\Psi(\boldsymbol{r},\boldsymbol{r}') = -\Psi(\boldsymbol{r}',\boldsymbol{r})$ and fermionic creation operators $\hat{c}^\dagger_{\boldsymbol{r}}$. The pair correlation function is then given by

$$\begin{aligned}
n^2\,g^{(2)}(|\boldsymbol{x}-\boldsymbol{x}'|) &= \langle\Psi|\,\hat{c}^\dagger_{\boldsymbol{x}}\hat{c}^\dagger_{\boldsymbol{x}'}\hat{c}_{\boldsymbol{x}'}\hat{c}_{\boldsymbol{x}}\,|\Psi\rangle \\
&= \langle\Psi|\,\hat{c}^\dagger_{\boldsymbol{x}}\hat{c}^\dagger_{\boldsymbol{x}'}\hat{c}_{\boldsymbol{x}'}\hat{c}_{\boldsymbol{x}} \iint \mathrm{d}^3\boldsymbol{r}\,\mathrm{d}^3\boldsymbol{r}'\,\Psi(\boldsymbol{r},\boldsymbol{r}')\,\hat{c}^\dagger_{\boldsymbol{r}}\hat{c}^\dagger_{\boldsymbol{r}'}\,|0\rangle \\
&= \langle\Psi|\,\hat{c}^\dagger_{\boldsymbol{x}}\hat{c}^\dagger_{\boldsymbol{x}'}\hat{c}_{\boldsymbol{x}'} \iint \mathrm{d}^3\boldsymbol{r}\,\mathrm{d}^3\boldsymbol{r}'\,\Psi(\boldsymbol{r},\boldsymbol{r}') \\
&\qquad\qquad \times\Big(\hat{c}^\dagger_{\boldsymbol{r}'}\delta^{(3)}(\boldsymbol{r}-\boldsymbol{x}) - \hat{c}^\dagger_{\boldsymbol{r}}\delta^{(3)}(\boldsymbol{r}'-\boldsymbol{x})\Big)\,|0\rangle \\
&= \underbrace{\langle\Psi|\,\hat{c}^\dagger_{\boldsymbol{x}}\hat{c}^\dagger_{\boldsymbol{x}'}}_{\text{'h.c. of the following'}} \iint \mathrm{d}^3\boldsymbol{r}\,\mathrm{d}^3\boldsymbol{r}'\,\Psi(\boldsymbol{r},\boldsymbol{r}') \\
&\qquad\qquad \times\big(\delta^{(3)}(\boldsymbol{r}-\boldsymbol{x})\delta^{(3)}(\boldsymbol{r}'-\boldsymbol{x}') - \delta^{(3)}(\boldsymbol{r}'-\boldsymbol{x}\delta^{(3)}(\boldsymbol{r}-\boldsymbol{x}')\big)\,|0\rangle \\
&= |\Psi(\boldsymbol{x},\boldsymbol{x}') - \Psi(\boldsymbol{x}',\boldsymbol{x})|^2 \\
&= 4\,|\Psi(\boldsymbol{x},\boldsymbol{x}')|^2 \ .
\end{aligned} \tag{G.2}$$

List of Publications

This work is based on the following articles. The publications [P1] and [P3] are no direct subject of this dissertation.

[P1] J. Whalen, S. Kanungo, R. Ding, **M. Wagner**, R. Schmidt, H. R. Sadeghpour, S. Yoshida, J. Burgdörfer, F. B. Dunning and T. C. Killian, Probing nonlocal spatial correlations in quantum gases with ultra-long-range rydberg molecules. *Phys. Rev. A* 100, 011402(R) (2019)

[P2] S. Tiwari, F. Engel, **M. Wagner**, R. Schmidt, F. Meinert and S. Wüster, Dynamics of atoms within atoms. *New J. Phys.* 24 073005 (2022)

[P3] C. Kuhlenkamp, M. Knap, **M. Wagner**, R. Schmidt, A. İmamoğlu, Tunable Feshbach resonances and their spectral signatures in bilayer semiconductors. *Phys. Rev. Lett.* 129, 037401 (2022)

[P4] M. Gievers, **M. Wagner**, R. Schmidt, Probing polaron clouds by Rydberg atom spectroscopy. *Phys. Rev. Lett.* 132, 053401 (2024)

[P5] **M. Wagner**, R. Ołdziejewski, F. Rose, V. Köder, C. Kuhlenkamp, A. İmamoğlu, R. Schmidt, Feshbach resonances of composite charge carrier states in atomically thin semiconductor heterostructures. Submitted to *Phys. Rev. Lett.* (2024) arXiv:2310.08729

Bibliography

[1] P. Kapitza. Viscosity of liquid helium below the λ-point. *Nature* **141**(3558):74–74, 1938. DOI:10.1038/141074a0.

[2] L. Landau. Theory of the superfluidity of helium II. *Phys Rev* **60**:356–358, 1941. DOI:10.1103/PhysRev.60.356.

[3] A. J. Leggett. Superfluidity. *Rev Mod Phys* **71**:S318–S323, 1999. DOI:10.1103/RevModPhys.71.S318.

[4] M. Boninsegni, N. V. Prokof'ev. Colloquium: supersolids: what and where are they? *Rev Mod Phys* **84**:759–776, 2012. DOI:10.1103/RevModPhys.84.759.

[5] A. Chiocchetta, D. Kiese, C. P. Zelle, et al. Cavity-induced quantum spin liquids. *Nature Communications* **12**(1):5901, 2021. DOI:10.1038/s41467-021-26076-3.

[6] S. Ohler, M. Kiefer-Emmanouilidis, M. Fleischhauer. Quantum spin liquids of Rydberg excitations in a honeycomb lattice induced by density-dependent Peierls phases. *Phys Rev Res* **5**:013157, 2023. DOI:10.1103/PhysRevResearch.5.013157.

[7] L. Ciorciaro, T. Smoleński, I. Morera, et al. Kinetic magnetism in triangular moiré materials. *Nature* **623**(7987):509–513, 2023. DOI:10.1038/s41586-023-06633-0.

[8] I. Morera, M. Kanász-Nagy, T. Smolenski, et al. High-temperature kinetic magnetism in triangular lattices. *Phys Rev Res* **5**:L022048, 2023. DOI:10.1103/PhysRevResearch.5.L022048.

[9] F. Böttcher, J.-N. Schmidt, J. Hertkorn, et al. New states of matter with fine-tuned interactions: quantum droplets and dipolar supersolids. *Reports on Progress in Physics* **84**(1):012403, 2020. DOI:10.1088/1361-6633/abc9ab.

[10] S. Ebadi, T. T. Wang, H. Levine, et al. Quantum phases of matter on a 256-atom programmable quantum simulator. *Nature* **595**(7866):227–232, 2021. DOI:10.1038/s41586-021-03582-4.

[11] A. Messiah. *Quantenmechanik 2*. De Gruyter, 1990. ISBN: 9783110126693.

[12] A. Altland, B. D. Simons. *Condensed matter field theory*. Cambridge university press, 2010. ISBN: 9780511789984.

[13] W. M. C. Foulkes, L. Mitas, R. J. Needs, G. Rajagopal. Quantum Monte Carlo simulations of solids. *Rev Mod Phys* **73**:33–83, 2001. DOI:10.1103/RevModPhys.73.33.

[14] K. G. Wilson. The renormalization group and critical phenomena. *Rev Mod Phys* **55**:583–600, 1983. DOI:10.1103/RevModPhys.55.583.

[15] W. Metzner, M. Salmhofer, C. Honerkamp, et al. Functional renormalization group approach to correlated fermion systems. *Rev Mod Phys* **84**:299–352, 2012. DOI:10.1103/RevModPhys.84.299.

[16] U. Schollwöck. The density-matrix renormalization group. *Rev Mod Phys* **77**:259–315, 2005. DOI:10.1103/RevModPhys.77.259.

[17] J. I. Cirac, D. Pérez-García, N. Schuch, F. Verstraete. Matrix product states and projected entangled pair states: concepts, symmetries, theorems. *Rev Mod Phys* **93**:045003, 2021. DOI:10.1103/RevModPhys.93.045003.

[18] D. J. Griffiths, D. F. Schroeter. *Introduction to quantum mechanics*. Cambridge university press, 2018. ISBN: 9781107189638.

[19] J. Bardeen, L. N. Cooper, J. R. Schrieffer. Theory of superconductivity. *Phys Rev* **108**:1175–1204, 1957. DOI:10.1103/PhysRev.108.1175.

[20] L. D. Landau, E. M. Lifshitz. *Statistical physics: course of theoretical physics, volume 5*. Elsevier, 2013. ISBN: 0080570461.

[21] L. D. Landau, E. M. Lifshitz. *Fluid mechanics: course of theoretical physics, volume 6*. Elsevier, 2013. ISBN: 1483128628.

[22] U. Weiss. *Quantum dissipative systems*. World Scientific, 2012. ISBN: 9789811243134.

[23] A. Rosch. Quantum-coherent transport of a heavy particle in a fermionic bath. *Advances in Physics* **48**(3):295–394, 1999. DOI:10.1080/000187399243446.

[24] R. Schmidt, M. Knap, D. A. Ivanov, et al. Universal many-body response of heavy impurities coupled to a Fermi sea: a review of recent progress. *Reports on Progress in Physics* **81**(2):024401, 2018. DOI:10.1088/1361-6633/aa9593.

[25] L. D. Landau. Electron motion in crystal lattices. *Phys Z Sowjet* **3**:664, 1933. DOI:10.1016/b978-0-08-010586-4.50015-8.

[26] M. Sidler, P. Back, O. Cotlet, et al. Fermi polaron-polaritons in charge-tunable atomically thin semiconductors. *Nature Physics* **13**(3):255–261, 2017. DOI:10.1038/nphys3949.

[27] A. Schirotzek, C.-H. Wu, A. Sommer, M. W. Zwierlein. Observation of Fermi polarons in a tunable Fermi liquid of ultracold atoms. *Phys Rev Lett* **102**:230402, 2009. DOI:10.1103/PhysRevLett.102.230402.

[28] Y. E. Shchadilova, R. Schmidt, F. Grusdt, E. Demler. Quantum dynamics of ultracold Bose polarons. *Phys Rev Lett* **117**:113002, 2016. DOI:10.1103/PhysRevLett.117.113002.

[29] W. E. Lamb, R. C. Retherford. Fine structure of the hydrogen atom. Part I. *Phys Rev* **79**:549–572, 1950. DOI:10.1103/PhysRev.79.549.

[30] J. J. Sakurai, J. Napolitano. *Modern quantum mechanics*. Cambridge University Press, 2020. ISBN: 9781108587280.

[31] J. I. Cirac, P. Zoller. Goals and opportunities in quantum simulation. *Nature Physics* **8**(4):264–266, 2012. DOI:10.1038/nphys2275.

[32] I. Bloch, J. Dalibard, S. Nascimbene. Quantum simulations with ultracold quantum gases. *Nature Physics* **8**(4):267–276, 2012. DOI:10.1038/nphys2259.

[33] I. Schwartz, Y. Shimazaki, C. Kuhlenkamp, et al. Electrically tunable Feshbach resonances in twisted bilayer semiconductors. *Science* **374**(6565):336–340, 2021. DOI:10.1126/science.abj3831.

[34] F. Engel. *From positive to negative ions, studies based on Rydberg spectroscopy*. Ph.D. thesis, 2020. ISBN: 9783843946049.

[35] M. Endres, T. Fukuhara, D. Pekker, et al. The 'Higgs' amplitude mode at the two-dimensional superfluid/Mott insulator transition. *Nature* **487**(7408):454–458, 2012. DOI:10.1038/nature11255.

[36] I. Bloch, J. Dalibard, W. Zwerger. Many-body physics with ultracold gases. *Rev Mod Phys* **80**:885–964, 2008. DOI:10.1103/RevModPhys.80.885.

[37] H. Feshbach. Unified theory of nuclear reactions. *Annals of Physics* **5**(4):357–390, 1958. DOI:10.1016/0003-4916(58)90007-1.

[38] H. Feshbach. A unified theory of nuclear reactions. II. *Annals of Physics* **19**(2):287–313, 1962. DOI:10.1016/0003-4916(62)90221-X.

[39] M. Duda, X.-Y. Chen, A. Schindewolf, et al. Transition from a polaronic condensate to a degenerate Fermi gas of heteronuclear molecules. *Nature Physics* **19**(5):720–725, 2023. DOI:10.1038/s41567-023-01948-1.

[40] E. C. Regan, D. Wang, C. Jin, et al. Mott and generalized Wigner crystal states in WSe_2/WS_2 moiré superlattices. *Nature* **579**(7799):359–363, 2020. DOI:10.1038/s41586-020-2092-4.

[41] Y. Shimazaki, C. Kuhlenkamp, I. Schwartz, et al. Optical signatures of periodic charge distribution in a Mott-like correlated insulator state. *Phys Rev X* **11**:021027, 2021. DOI:10.1103/PhysRevX.11.021027.

[42] Y. Xu, S. Liu, D. A. Rhodes, et al. Correlated insulating states at fractional fillings of moiré superlattices. *Nature* **587**(7833):214–218, 2020. DOI:10.1038/s41586-020-2868-6.

[43] C. Jin, Z. Tao, T. Li, et al. Stripe phases in WSe_2/WS_2 moiré superlattices. *Nature Materials* **20**(7):940–944, 2021. DOI:10.1038/s41563-021-00959-8.

[44] X. Huang, T. Wang, S. Miao, et al. Correlated insulating states at fractional fillings of the WS_2/WSe_2 moiré lattice. *Nature Physics* **17**(6):715–719, 2021. DOI:10.1038/s41567-021-01171-w.

[45] I. Amelio, N. D. Drummond, E. Demler, et al. Polaron spectroscopy of a bilayer excitonic insulator. *Phys Rev B* **107**:155303, 2023. DOI:10.1103/PhysRevB.107.155303.

[46] T. Smoleński, P. E. Dolgirev, C. Kuhlenkamp, et al. Signatures of Wigner crystal of electrons in a monolayer semiconductor. *Nature* **595**(7865):53–57, 2021. DOI:10.1038/s41586-021-03590-4.

[47] Y. Zhou, J. Sung, E. Brutschea, et al. Bilayer Wigner crystals in a transition metal dichalcogenide heterostructure. *Nature* **595**(7865):48–52, 2021. DOI:10.1038/s41586-021-03560-w.

[48] Y.-M. Xie, C.-P. Zhang, J.-X. Hu, et al. Valley-polarized quantum anomalous hall state in moiré $MoTe_2/WSe_2$ heterobilayers. *Phys Rev Lett* **128**:026402, 2022. DOI:10.1103/PhysRevLett.128.026402.

[49] J. Cai, E. Anderson, C. Wang, et al. Signatures of fractional quantum anomalous Hall states in twisted $MoTe_2$. *Nature* 2023. DOI:10.1038/s41586-023-06289-w.

[50] K. F. Mak, C. Lee, J. Hone, et al. Atomically thin MoS_2: a new direct-gap semiconductor. *Phys Rev Lett* **105**:136805, 2010. DOI:10.1103/PhysRevLett.105.136805.

[51] G. Wang, A. Chernikov, M. M. Glazov, et al. Colloquium: excitons in atomically thin transition metal dichalcogenides. *Rev Mod Phys* **90**:021001, 2018. DOI:10.1103/RevModPhys.90.021001.

[52] Y. Zhan, Z. Liu, S. Najmaei, et al. Large-area vapor-phase growth and characterization of MoS_2 atomic layers on a SiO_2 substrate. *Small* **10**(8(7)):966–71, 2012. DOI:10.1002/smll.201102654.

[53] K. S. Novoselov, A. K. Geim, S. V. Morozov, et al. Electric field effect in atomically thin carbon films. *Science* **306**(5696):666–669, 2004. DOI:10.1126/science.1102896.

[54] A. K. Geim, I. V. Grigorieva. Van der Waals heterostructures. *Nature* **499**(7459):419–425, 2013. DOI:10.1038/nature12385.

[55] D. A. Ruiz-Tijerina, M. Danovich, C. Yelgel, et al. Hybrid $\mathrm{k}\cdot\mathrm{p}$ tight-binding model for subbands and infrared intersubband optics in few-layer films of transition-metal dichalcogenides: MoS_2, $MoSe_2$, WS_2, and WSe_2. *Phys Rev B* **98**:035411, 2018. DOI:10.1103/PhysRevB.98.035411.

[56] A. Kormányos, G. Burkard, M. Gmitra, et al. $\mathrm{k}\cdot\mathrm{p}$ theory for two-dimensional transition metal dichalcogenide semiconductors. *2D Materials* **2**(2):022001, 2015. DOI:10.1088/2053-1583/2/2/022001.

[57] I. Kylänpää, H.-P. Komsa. Binding energies of exciton complexes in transition metal dichalcogenide monolayers and effect of dielectric environment. *Phys Rev B* **92**:205418, 2015. DOI:10.1103/PhysRevB.92.205418.

[58] F. Wilczek. Majorana returns. *Nature Physics* **5**(9):614–618, 2009. DOI:10.1038/nphys1380.

[59] T. Cao, G. Wang, W. Han, et al. Valley-selective circular dichroism of monolayer molybdenum disulphide. *Nature Communications* **3**(1):887, 2012. DOI:10.1038/ncomms1882.

[60] K. F. Mak, K. He, J. Shan, T. F. Heinz. Control of valley polarization in monolayer MoS_2 by optical helicity. *Nature Nanotechnology* **7**(8):494–498, 2012. DOI:10.1038/nnano.2012.96.

[61] G. Sallen, L. Bouet, X. Marie, et al. Robust optical emission polarization in MoS_2 monolayers through selective valley excitation. *Phys Rev B* **86**:081301, 2012. DOI:10.1103/PhysRevB.86.081301.

[62] J. Kim, X. Hong, C. Jin, et al. Ultrafast generation of pseudo-magnetic field for valley excitons in WS_2 monolayers. *Science* **346**(6214):1205–1208, 2014. DOI:10.1126/science.1258122.

[63] N. S. Rytova. Screened potential of a point charge in a thin film. *Proc MSU, Phys Astron* **3**, 1967. DOI:10.48550/arXiv.1806.00976.

[64] L. Keldysh. Coulomb interaction in thin semiconductor and semimetal films. *Soviet Journal of Experimental and Theoretical Physics Letters* **29**:658, 1979. DOI:10.1142/9789811279461_0024.

[65] P. Cudazzo, I. V. Tokatly, A. Rubio. Dielectric screening in two-dimensional insulators: implications for excitonic and impurity states in graphane. *Phys Rev B* **84**:085406, 2011. DOI:10.1103/PhysRevB.84.085406.

[66] Y. Li, J. Ludwig, T. Low, et al. Valley splitting and polarization by the Zeeman effect in monolayer $MoSe_2$. *Phys Rev Lett* **113**:266804, 2014. DOI:10.1103/PhysRevLett.113.266804.

[67] C. Zhang, Y. Chen, A. Johnson, et al. Probing critical point energies of transition metal dichalcogenides: surprising indirect gap of single layer WSe_2. *Nano Letters* **15**(10):6494–6500, 2015. DOI:10.1021/acs.nanolett.5b01968.

[68] A. Molina-Sánchez, L. Wirtz. Phonons in single-layer and few-layer MoS_2 and WS_2. *Phys Rev B* **84**:155413, 2011. DOI:10.1103/PhysRevB.84.155413.

[69] A. Chernikov, T. C. Berkelbach, H. M. Hill, et al. Exciton binding energy and nonhydrogenic Rydberg series in monolayer WS_2. *Phys Rev Lett* **113**:076802, 2014. DOI:10.1103/PhysRevLett.113.076802.

[70] M. D. Sturge. Optical absorption of gallium arsenide between 0.6 and 2.75 eV. *Phys Rev* **127**:768–773, 1962. DOI:10.1103/PhysRev.127.768.

[71] C. Fey, P. Schmelcher, A. Imamoglu, R. Schmidt. Theory of exciton-electron scattering in atomically thin semiconductors. *Phys Rev B* **101**:195417, 2020. DOI:10.1103/PhysRevB.101.195417.

[72] M. M. Glazov, T. Amand, X. Marie, et al. Exciton fine structure and spin decoherence in monolayers of transition metal dichalcogenides. *Phys Rev B* **89**:201302, 2014. DOI:10.1103/PhysRevB.89.201302.

[73] C. Chin, R. Grimm, P. Julienne, E. Tiesinga. Feshbach resonances in ultracold gases. *Rev Mod Phys* **82**:1225–1286, 2010. DOI:10.1103/RevModPhys.82.1225.

[74] H. Friedrich. *Scattering theory*. Springer, 2013. ISBN: 9783642382826.

[75] U. Fano. Sullo spettro di assorbimento dei gas nobili presso il limite dello spettro d'arco. *Il Nuovo Cimento (1924-1942)* **12**(3):154–161, 1935. DOI:10.1007/bf02958288.

[76] U. Fano, G. Pupillo, A. Zannoni, C. W. Clark. On the absorption spectrum of noble gases at the arc spectrum limit. *Journal of research of the National Institute of Standards and Technology* **110**(6):583, 2005. DOI:10.6028/jres.110.083.

[77] A. J. Moerdijk, B. J. Verhaar, A. Axelsson. Resonances in ultracold collisions of ^{6}Li, ^{7}Li, and ^{23}Na. *Phys Rev A* **51**:4852–4861, 1995. DOI:10.1103/PhysRevA.51.4852.

[78] C. Langmack, R. Schmidt, W. Zwerger. Efimov states near a Feshbach resonance and the limits of van der Waals universality at finite background scattering length. *Phys Rev A* **97**:033623, 2018. DOI:10.1103/PhysRevA.97.033623.

[79] R. Schmidt, S. P. Rath, W. Zwerger. Efimov physics beyond universality. *The European Physical Journal B* **85**:1–6, 2012. DOI:10.1140/epjb/e2012-30841-3.

[80] R. Schmidt. *From few-to many-body physics with ultracold atoms*. Ph.D. thesis, Technische Universität München, 2013. TUM: 1145048.

[81] C. A. Kocher. Criteria for bound-state solutions in quantum mechanics. *American Journal of Physics* **45**(1):71–74, 1977. DOI:https://doi.org/10.1119/1.10913.

[82] S. K. Adhikari. Quantum scattering in two dimensions. *American Journal of Physics* **54**(4):362–367, 1986. DOI:https://doi.org/10.1119/1.14623.

[83] K. Kanjilal, D. Blume. Coupled-channel pseudopotential description of the Feshbach resonance in two dimensions. *Phys Rev A* **73**:060701, 2006. DOI:10.1103/PhysRevA.73.060701.

[84] R. Schmidt, T. Enss, V. Pietilä, E. Demler. Fermi polarons in two dimensions. *Phys Rev A* **85**:021602, 2012. DOI:10.1103/PhysRevA.85.021602.

[85] C. Fey, J. Yang, S. T. Rittenhouse, et al. Effective three-body interactions in Cs(6s)-Cs(nd) Rydberg trimers. *Phys Rev Lett* **122**:103001, 2019. DOI:10.1103/PhysRevLett.122.103001.

[86] K. Zhang, Y. Feng, F. Wang, et al. Two dimensional hexagonal boron nitride (2D-hBN): synthesis, properties and applications. *Journal of Materials Chemistry C* **5**(46):11992–12022, 2017. DOI:10.1039/C7TC04300G.

[87] B. Borodin, M. Dunaevskiy, F. Benimetskiy, et al. Kelvin probe microscopy of MoSe2 monolayers on graphene. In *Journal of Physics: Conference Series*, vol. 1124, p. 081031. IOP Publishing, 2018. DOI:10.1088/1742-6596/1124/8/081031.

[88] M. H. Beck, A. Jäckle, G. A. Worth, H.-D. Meyer. The multiconfiguration time-dependent Hartree (MCTDH) method: a highly efficient algorithm for propagating wavepackets. *Physics Reports* **324**(1):1–105, 2000. DOI:10.1016/S0370-1573(99)00047-2.

[89] F. P. Laussy, A. V. Kavokin, I. A. Shelykh. Exciton-polariton mediated superconductivity. *Phys Rev Lett* **104**:106402, 2010. DOI:10.1103/PhysRevLett.104.106402.

[90] F. P. Laussy. Superconductivity with excitons and polaritons: review and extension. *Journal of Nanophotonics* **6**(1):064502, 2012. DOI:10.1117/1.jnp.6.064502.

[91] J. von Milczewski, X. Chen, A. Imamoglu, R. Schmidt. Superconductivity induced by strong electron-exciton coupling in doped atomically thin semiconductor heterostructures. *arXiv preprint arXiv:231010726* 2023. DOI:10.48550/arXiv.2310.10726.

[92] I. A. Shelykh, T. Taylor, A. V. Kavokin. Rotons in a hybrid Bose-Fermi system. *Phys Rev Lett* **105**:140402, 2010. DOI:10.1103/PhysRevLett.105.140402.

[93] E. Cherotchenko, T. Espinosa-Ortega, A. Nalitov, et al. Superconductivity in semiconductor structures: the excitonic mechanism. *Superlattices Microstruct* **90**:170–175, 2016. DOI:10.1016/j.spmi.2015.12.003.

[94] O. Cotleţ, S. Zeytinoğlu, M. Sigrist, et al. Superconductivity and other collective phenomena in a hybrid Bose-Fermi mixture formed by a polariton condensate and an electron system in two dimensions. *Phys Rev B* **93**:054510, 2016. DOI:10.1103/PhysRevB.93.054510.

[95] K. S. Krane. *Introductory nuclear physics*. John Wiley & Sons, 1991. ISBN: 9780471805533.

[96] W. Zwerger. *The BCS-BEC crossover and the unitary Fermi gas*. Springer Science & Business Media, 2011. ISBN: 9783642219788.

[97] R. Schmidt, H. R. Sadeghpour, E. Demler. Mesoscopic Rydberg impurity in an atomic quantum gas. *Phys Rev Lett* **116**:105302, 2016. DOI:10.1103/PhysRevLett.116.105302.

[98] C. H. Greene, A. S. Dickinson, H. R. Sadeghpour. Creation of polar and nonpolar ultra-long-range Rydberg molecules. *Phys Rev Lett* **85**:2458–2461, 2000. DOI:10.1103/PhysRevLett.85.2458.

[99] V. Bendkowsky, B. Butscher, J. Nipper, et al. Observation of ultralong-range Rydberg molecules. *Nature* **458**(7241):1005–1008, 2009. DOI:10.1038/nature07945.

[100] F. Camargo, R. Schmidt, J. D. Whalen, et al. Creation of Rydberg polarons in a Bose gas. *Phys Rev Lett* **120**:083401, 2018. DOI:10.1103/PhysRevLett.120.083401.

[101] R. Schmidt, J. D. Whalen, R. Ding, et al. Theory of excitation of Rydberg polarons in an atomic quantum gas. *Phys Rev A* **97**:022707, 2018. DOI:10.1103/PhysRevA.97.022707.

[102] M. T. Eiles. Trilobites, butterflies, and other exotic specimens of long-range Rydberg molecules. *Journal of Physics B: Atomic, Molecular and Optical Physics* **52**(11):113001, 2019. DOI:10.1088/1361-6455/ab19ca.

[103] C. Fey, F. Hummel, P. Schmelcher. Ultralong-range Rydberg molecules. *Molecular Physics* **118**(2):e1679401, 2020. DOI:10.1080/00268976.2019.1679401.

[104] E. Amaldi, E. Segrè. Effect of pressure on high terms of alkaline spectra. *Nature* **133**(3352):141–141, 1934. DOI:10.1038/133141a0.

[105] E. Fermi. Sopra lo spostamento per pressione delle righe elevate delle serie spettrali. *Il Nuovo Cimento (1924-1942)* **11**:157–166, 1934. DOI:10.1007/bf02959829.

[106] T. C. Liebisch, M. Schlagmüller, F. Engel, et al. Controlling Rydberg atom excitations in dense background gases. *Journal of Physics B: Atomic, Molecular and Optical Physics* **49**(18):182001, 2016. DOI:10.1088/0953-4075/49/18/182001.

[107] A. Gaj, A. T. Krupp, J. B. Balewski, et al. From molecular spectra to a density shift in dense Rydberg gases. *Nature Communications* **5**(1):4546, 2014. DOI:10.1038/ncomms5546.

[108] D. Barredo, S. De Léséleuc, V. Lienhard, et al. An atom-by-atom assembler of defect-free arbitrary two-dimensional atomic arrays. *Science* **354**(6315):1021–1023, 2016. DOI:10.1126/science.aah3778.

[109] M. Endres, H. Bernien, A. Keesling, et al. Atom-by-atom assembly of defect-free one-dimensional cold atom arrays. *Science* **354**(6315):1024–1027, 2016. DOI:10.1126/science.aah3752.

[110] H. Bernien, S. Schwartz, A. Keesling, et al. Probing many-body dynamics on a 51-atom quantum simulator. *Nature* **551**(7682):579–584, 2017. DOI:10.1038/nature24622.

[111] G.-B. Jo, Y.-R. Lee, J.-H. Choi, et al. Itinerant ferromagnetism in a Fermi gas of ultracold atoms. *Science* **325**(5947):1521–1524, 2009. DOI:10.1126/science.1177112.

[112] C. Sanner, E. J. Su, W. Huang, et al. Correlations and pair formation in a repulsively interacting Fermi gas. *Phys Rev Lett* **108**:240404, 2012. DOI:10.1103/PhysRevLett.108.240404.

[113] G. Valtolina, F. Scazza, A. Amico, et al. Exploring the ferromagnetic behaviour of a repulsive Fermi gas through spin dynamics. *Nature Physics* **13**(7):704–709, 2017. DOI:10.1038/nphys4108.

[114] A. Amico, F. Scazza, G. Valtolina, et al. Time-resolved observation of competing attractive and repulsive short-range correlations in strongly interacting Fermi gases. *Phys Rev Lett* **121**:253602, 2018. DOI:10.1103/PhysRevLett.121.253602.

[115] R. S. Lous, I. Fritsche, M. Jag, et al. Probing the interface of a phase-separated state in a repulsive Bose-Fermi mixture. *Phys Rev Lett* **120**:243403, 2018. DOI:10.1103/PhysRevLett.120.243403.

[116] K. B. Gubbels, H. T. Stoof. Imbalanced Fermi gases at unitarity. *Physics Reports* **525**(4):255–313, 2013. DOI:10.1016/j.physrep.2012.11.004.

[117] F. Ferlaino, S. Knoop, R. Grimm. *Ultracold Feshbach molecules*. CRC Press, 2009. ISBN: 9780429149504.

[118] L. S. Levitov, H. Lee, G. B. Lesovik. Electron counting statistics and coherent states of electric current. *Journal of Mathematical Physics* **37**(10):4845–4866, 1996. DOI:10.1063/1.531672.

[119] I. Klich. Full counting statistics: an elementary derivation of Levitov's formula. *arXiv preprint cond-mat/0209642* 2002. DOI:10.48550/arXiv.cond-mat/0209642.

[120] A. E. Siegman. *Lasers*. University Science Books, 1986. ISBN: 0935702113.

[121] C. J. Pethick, H. Smith. *Bose-Einstein condensation in dilute gases*. Cambridge University Press, 2008. ISBN: 9780511802850.

[122] J. Söding, D. Guéry-Odelin, P. Desbiolles, et al. Three-body decay of a rubidium Bose–Einstein condensate. *Applied physics B* **69**:257–261, 1999. DOI:10.1007/s003400050805.

Acknowledgments

Scientific work and the development of new ideas in general profits and in most cases relies on the direct interaction of people. The progress in science would be rather slow without the exchange of ideas during discussions, conferences, lunch breaks, etc., the collaboration within the scientific community, the inspiration found while attending meetings and talks, or the exchange with colleagues while tackling problems with joint forces. This being said there are many people without whom I would not have been able to write this thesis.

First I would like to thank my PhD supervisor Richard Schmidt for all the inspiration and insights, whose excitement and joy about physics always spreads during conversations and discussions. He supported me through out the whole time of my PhD and helped to find solutions to all problems.

I thank Hans Peter Büchler for co-examining this thesis, allowing me to conclude this PhD project in the planned time frame; this also holds true for the other members of the examination committee Jana Zaumseil and Selim Jochim. I also want to thank Wilhelm Zwerger for the supervision of my PhD project during my time in Munich, Hossein Sadeghpour and Ataç İmamoğlu for insightful discussions.

Further I would like to thank Clemens Kuhlenkamp for fruitful discussions and help with numerical questions. I thank my colleagues Christian Fey, Rafał Ołdziejewski, Félix Rose, Jonas von Milczewski, Xin Chen, Marcel Gievers, Oriana Dießel and Arthur Christianen for helpful discussions and support in coding questions; we spend great times together with the rest of our colleagues Enderalp Yakaboylu, Zhongda Zeng, Aileen Durst, Zied Jaber and Ruipeng Li inside and outside of our office at MPQ. Also I thank my colleges and flatmates Eruthuparna Ramachandran and Renhao Tao for good conversations, the evenings spent together cooking and eating, and lots of fun. I thank my colleagues in Heidelberg Anton Andersen, Verena Köder, Eugen Dizer, Florian Hirsch, Ekaterina Vlasiuk and again Xin Chen for the nice atmosphere in the office.

Also I would not have been able to do this without the support from all my friends from Stuttgart; thank you.

Finally, I want to thank my Family for their continuous support at all levels. This would not have been possible without you.